Nanoscale Mechanics of Helical and Angular Structures: Exploring and Expanding the Capabilities of Objective Molecular Dynamics

A THESIS
SUBMITTED TO THE FACULTY OF THE GRADUATE SCHOOL
OF THE UNIVERSITY OF MINNESOTA
BY

Ilia Andreyevich Nikiforov

IN PARTIAL FULFILLMENT OF THE REQUIREMENTS
FOR THE DEGREE OF
DOCTOR OF PHILOSOPHY

Traian Dumitrică

June, 2014

Acknowledgements

- I would like to thank Prof. Dumitrică and all of my co-authors for their patience and valuable insights, instruction, and help.
- I would like to thank Prof. Dmitri Golberg and the National Institute for Materials Science, Tsukuba, and Prof. Thomas Frauenheim and the Bremen Center for Computational Materials Science at the University of Bremen. Their hospitality made me feel at home and made my international research experiences fulfilling and enlightening.
- All images of atomistic representations were created using VMD [1].
- All computations in this dissertation were carried out at the Minnesota Supercomputing Institute.
- I would like to acknowledge support from the Doctoral Dissertation Fellowship for the 2013-14 academic year.
- The research in Chapter 3 was supported by NSF CAREER grant no. CMMI-0747684, NSF grant no. 1006706, and AFOSR grant no. FA9550-09-1-0339.
- The research in Chapter 4 was supported by NSF CAREER Grant CMMI-0747684.
- The molecular orbital analysis and POAV2 numerical calculations in Sec. 4.2 were performed by Dr. Evgeniya Dontsova, Department of Materials Engineering, University of British Columbia.
- Appendix A was adapted from Prof. Richard James, Department of Aerospace Engineering and Mechanics, University of Minnesota.

- The research in Chapter 5 was supported by National Science Foundation (NSF) CAREER Grant No. CMMI-0747684, NSF Grant No. DMR-1006706, and NSF Grant No. CMMI-1332228.

- The helical Ewald formulas in Sec. 5.2 were developed in collaboration with Prof. Traian Dumitrică. Also acknowledged are useful discussions with M. Elstner and A. Enyashin.

- The objective SCC-DFTB simulations carried out in Sec. 5.3 were made possible by the incorporation of the helical Ewald module (written by myself, Appendix D) into the DFTB+ simulation package, carried out by Dr. Benjamin Hourahine, Department of Physics, SUPA, University of Stratchclyde, and Dr. Balint Aradi, BCCMS, University of Bremen.

- The research in Chapter 6 was supported by NSF Grant No. DMR-1006706, the Center for Materials Nanoarchitectonics of the National Institute for Materials Science, Tsukuba, Japan, and the Russian Ministry for Science and Education (Agreement No. 11.G34.31.0061). The international collaboration was made possible by NSF EAPSI and JSPS Summer Institute programs.

- The experiments in Chapter 6 were carried out by Dr. Dai-Ming Tang and Dr. Xianlong Wei, National Institute for Materials Science, Tsukuba.

- The LAMMPS calculation in Chapter 7 was carried out by Jihong Ma, Department of Mechanical Engineering, University of Minnesota.

Dedication

I would like to dedicate this dissertation to my grandfather, Mikhail Nikiforov, who sadly passed away in December 2013. You will always live on in my heart and are a great inspiration in my goal to become the third generation of "Dr. Nikiforov".

Abstract

Objective molecular dynamics (OMD) is a recently developed generalization of the traditionally employed periodic boundary conditions (PBC) used in atomistic simulations. OMD allows for helical and/or rotational symmetries to be exploited in addition to translational symmetry. These symmetries are especially prevalent in nanostructures, and OMD enables or facilitates many simulations that were previously difficult or impossible to carry out. This includes simulations of pristine structures that inherently possess helical and/or angular symmetries (such as nanotubes), structures that contain defects (such as screw disclocations) or stuctures that are subjected to deformations (such as bending or torsion).

OMD is already a powerful method, having been coupled with the quantum-mechanical density functional-based tight-binding (DFTB) method, as well as with classical potentials. In this work, these capabilities are used to investigate electromechanical properties of silicon nanowires, treating the mechanical simulation results in the context of continuum mechanics. The bending of graphene is studied, and the underlying molecular orbital mechanisms are investigated. The implications of the results on other simulation methods used to study bending of graphene are discussed. OMD is used in an experimental-theoretical collaboration studying the kinking of graphene and boron nitride nanoribbons. The simulations elucidate and quantify the underlying mechanism behind the kinking seen in experiments.

Although theoretically, as a generalization, OMD can match or exceed the capabilities of PBC in all cases, OMD is a new method. Thus, practical implementation must be tackled to expand the capabilities of OMD to new simulation methods and simulation types. In this work, OMD is expanded to allow coupling with self-consistent charge (SCC) DFTB, by developing and implementing the required summation formulas for electrostatic and dispersion interactions. SCC-DFTB is an improved form of the standard DFTB method which includes explicit consideration of charge transfer between atoms. This allows for improved description of heteronuclear materials. To demonstrate this capability, proof-of-concept calculations are carried out on a boron nitride nanotube, a screw-dislocated zinc oxide nanowire, and a single-helix DNA molecule.

Finally, preliminary development of heat current calculations under OMD is presented. Heat current calculations are used for calculating thermal conductivity of materials from equilibrium molecular dynamics. So far, heat current calculations have been implemented for the pairwise Lennard-Jones potential. The next development (not yet implemented) is the extension of the heat current calculation under OMD to the Tersoff interatomic potential. The challenges and considerations involved are discussed.

Contents

List of Tables

List of Figures

Chapter 1

Introduction

- Chapter 2 introduces the concept of atomistic modeling in general, followed by a description of objective molecular dynamics (OMD). A description of the generalization of tight-binding to helical and rotational symmetry is included. Tight-binding is a powerful method for modeling interatomic interactions that maintains high computational speed while explicitly describing electronic structure. It is used for the majority of the simulations found herein.
- Chapter 3 presents an application of OMD coupled with density functional-based tight binding (DFTB) – electromechanical properties of screw-dislocated silicon nanowires. This chapter has been published as Ref. [111].
- Chapter 4 presents another application of OMD coupled with DFTB – bending mechanics of monolayer graphene. The contents of this chapter were published as Ref. [3]. Appendices A, B, and C are associated with this chapter.
- Chapter 5 concerns the expansion of the current capabilities of objective molecular dynamics to include a self-consistent charge correction (SCC-DFTB) in the DFTB implementation, allowing for charge transfer between atoms in a unit cell. This required the generalization of the venerable Ewald summation method to helical symmetry. Example calculations of a boron-nitride nanotube, a screw-dislocated zinc oxide nanowire and a single helix of DNA are included. The contents of this chapter were published as Ref. [53]. Appendix D contains the Fortran modules developed as part of this work.

- While DFTB is a highly accurate and powerful method as demonstrated in the previous chapters, classical interatomic interaction potentials still have their place, for systems with simple interactions and/or large numbers of atoms. Chapter 6 contains an application of OMD coupled with the classical Tersoff potential – an experimental-theoretical collaboration studying the bending of multi-layer boron-nitride and graphene nanoribbons. This work has been published as Ref. [2]. A description of the classical potentials used in this chapter can be found in Appendix E.

- In Chapter 7, early work on the implementation of heat current calculations – useful for calculating thermal conductivity of structures – is presented. So far, heat current can be computed for van der Waals objective structures.

- Chapter 8 summarizes the work performed and proposes possible future research.

- Appendix F lists the symbols used to describe objective boundary conditions throughout the work. An effort has been made to keep the description of this unifying theme consistent.

Chapter 2

Theoretical Background

2.1 Atomistic Modeling

The computations performed in this dissertation fall under the umbrella of atomistic modeling. In atomistic modeling, physical properties of a system are calculated by considering the positions $\mathbf{X}_i$ of the individual atoms comprising the system. In abstract, the central concept is that the potential energy of the system is a function of the coordinates of all n of the constituent atoms,

$$E = E(\mathbf{X}_1, \mathbf{X}_2, ..., \mathbf{X}_n). \tag{2.1}$$

By differentiating the energy with respect to each atomic position, the force on each atom is obtained. Then, each atom i can be treated as a Newtonian point mass m_i and the position of each atom may be evolved in time by numerically integrating the equation of motion

$$m_i \frac{\partial^2 \mathbf{X}_i}{\partial t^2} = -\frac{\partial E}{\partial \mathbf{X}_i}, \quad i = 1, ..., n. \tag{2.2}$$

This is called *molecular dynamics*, and represents the behavior of the system at a finite temperature. Typically, Eq. 2.2 is integrated using a *symplectic* algorithm, such as Velocity Verlet. These algorithms conserve the total (kinetic and potential) energy of the system from step to step. Depending on the type of molecular dynamics simulation being run, the energy-conserving time evolution may proceed untouched, or the velocities and/or positions of the atoms may be adjusted at each step. This allows for different

thermodynamic properties of the system (such as temperature, total energy, enhalpy, pressure, volume, etc.) to be held constant, while others are allowed to vary.

Alternatively, one may seek to minimize the energy with respect to the atomic positions, using a nonlinear optimization method such as the nonlinear conjugate gradient method, or the steepest descent method. Starting from some initial set of atomic coordinates, the gradient of the forces is used to find the nearest local minimum to said initial coordinates. This *structural relaxation* results in a static configuration which essentially repesents the state of the system in the low-temperature limit.

Of course, in any situation where finite temperature is a significant consideration, it is necessary to perform molecular dynamics simulations. Obviously, any simulation where thermal properties are of interest (heat capacity, thermal conductivity, melting point, etc.) must be studied with molecular dynamics. Also, thermal effects play a role in other properties of physical systems as well. One cannot, for example, study the compressibility of helium gas at room temperature by considering a helium crystal at 0 K, or the tensile stiffness of a protein at room temperature by considering only the zero-temperature structure – entropic effects are too important. However, the evaluation of properties using molecular dynamics requires a large amount of time integration steps, in order to equilibrate the system and/or obtain a large enough statistical sample.

In this dissertation, structural relaxation is the primary approach used. Chapters 3 and 4 are concerned with mechanical properties and band structure of covalent nanocrystals under deformation. Because the melting temperature of covalent crystals is much higher than room temperature, their zero-temperature ground-state properties are good approximations for room-temperature behavior. Conjugate gradient structural relaxations at different degrees of deformation (twist and bending) are carried out in order to determine the deformation dependence of the band structure or strain energy.

Chapter 6 is also concerned with nanomechanical properties of crystalline materials. In that chapter, molecular dynamics is used, but only as a method of perturbing the system. Recall that structural relaxation finds the local minimum nearest to the initial configuration, which may not be the minimum of interest. For example, Chapter 6 studies the experimentally-observed localized kinking under bending of multi-layer graphene and hexagonal boron nitride nanoribbons. Of interest is the bending angle at which smooth bending becomes localized kinking. However, even at bending angles

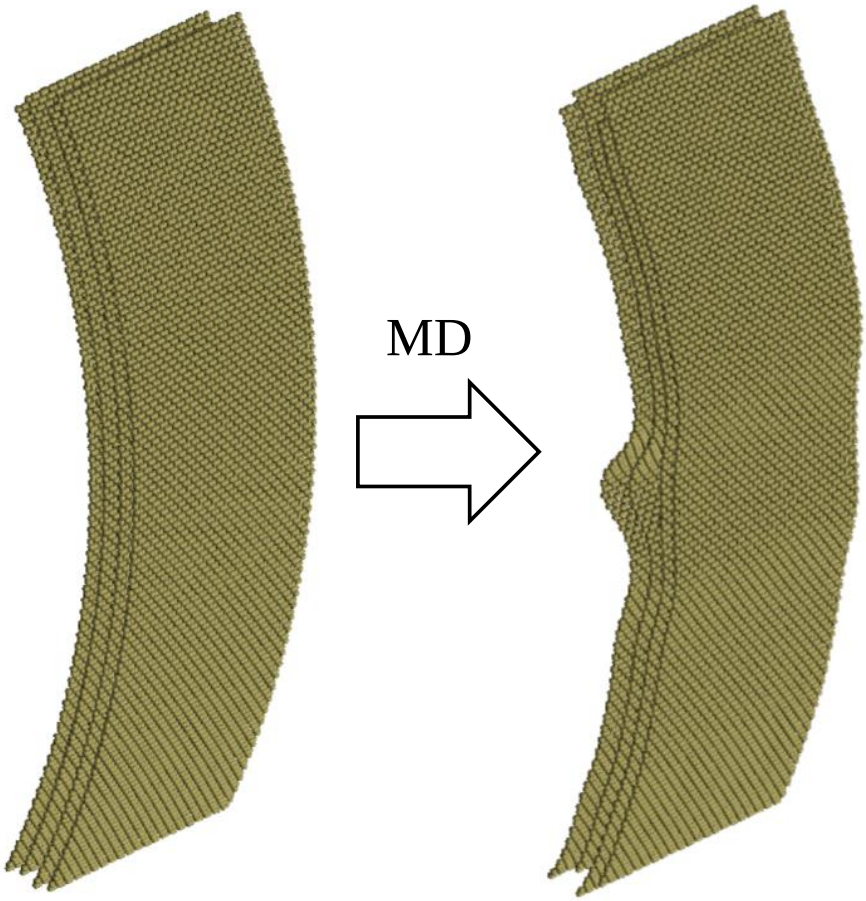

Figure 2.1: Metastable states of four-layer graphene. Molecular dynamics perturbs the systems and allows it to cross the energy barrier between the higher-energy smooth metastable state on the left to the lower-energy kinked state on the right.

higher than this threshold, the smooth bending configuration is a *metastable state* – a local minimum of higher energy than the kinked state. Molecular dynamics performed for short times at approximately room temperature creates thermal vibrations large enough to overcome the energy barrier between the two states and drive the system to the lower-energy kinked state (Fig. 2.1). In the experiments this occurs spontaneously, as they are performed at room temperature and the atoms are always subject to thermal vibrations. Thus, molecular dynamics is useful even if thermodynamic properties are not of interest. The goal is not to seek the absolute minimum energy of a given set of atoms, however – for example, it is not desirable for the graphene nanoribbon to transform into diamond. Room temperature is far too low for this to occur.

Chapter 5 is concerned with the development of a new simulation methodology, and thus the simulations carried out therein are primarily intended as a proof-of concept. Thus, all of the simulations are structural relaxations, as they are quicker to execute than molecular dynamics. After all, if it is possible to carry out structural relaxation, it means that the energy and the forces (gradients of the energy) are known. All that is needed, then, to perform molecular dynamics is the mass of each atom. Regarding the simulations themselves, they are calculations of torsional mechanics of a boron-nitride nanotube, zinc oxide nanowire, and a DNA strand. Of these, the results of the nanotube and nanowire calculations are likely to be meaningful at room temperature, as these are covalent solids. Admittedly, temperature-dependent entropic effects play an important role in the mechanical behavior of organic polymers such as DNA, thus zero-temperature structural relaxations may not be directly useful for applications.

Chapter 7, however, is concerned with evaluation of thermal properties – specifically, heat current for the purpose of evaluating thermal conductivity. Thus, in that Chapter, molecular dynamics is fully utilized.

The potential energy function can range greatly in complexity and computational speed. The simpler forms are closed-form analytical expressions based on arguments about the nature of interatomic interactions, and fitted to reproduce properties calculated by higher level simulation methods, or experimentally measured. The most simplistic are sums of terms containing only pairwise interactions between atoms. One such potential is the Lennard-Jones potential (Appendix E.2). It is suitable for simulating noble gases, and is used for this purpose in Chapter 7. It is also useful for treating

inter-layer interactions in layered solids such as multi-layer graphene and hexagonal boron nitride. It is used for this purpose in Chapter 6. More complicated analytical potentials include sums of many-body terms. An example is the Tersoff potential, suitable for a description of covalent binding in semiconductors. It is described in more detail in Appendix E.1 and used in Chapter 6 in order to describe the intra-layer interactions in the layered solids.

More advanced potentials are explicitly quantum-mechanical in nature. The Born-Oppenheimer approximation is invoked, which states that the electronic and ionic wavefunctions are separable due to the large difference in mass between the ions and the electrons. Furthermore, the ions are treated as classical point particles, and static as far as the electrons are concerned. Finally, the electronic structure problem is solved in the static potential created by the ions. As solution of the multi-particle Schrödinger equation is non-tractable in all but the simplest cases, so various simplifications and approximations are made in different methods. In Chapters 3 and 4, the density functional-based tight binding (DFTB) method is used, described in detail in Sec. 2.4. Tight-binding is the simplest expicitly quantum-mechanical simulation method. Essentially, the one-electron wavefunctions are approximated as linear superpositions of pre-computed atom-centered atomic-like orbitals, and electron-electron interactions are not explicitly considered. In DFTB specifically, the precomputed orbitals, as well as the pairwise repulsion between ion cores, are fitted from the highly accurate first-principles density-functional theory (DFT). One may think of this fitting as implicitly, empirically describing effects that are not explicitly included in tight-binding. Chapter 5 concerns the generalization of self-consistent charge (SCC) DFTB to objective symmetry. The SCC correction allows for charge transfer between atoms, representing a computationally efficient way of approximately treating the electron-electron interactions.

2.2 Periodic Boundary Conditions

Unfortunately, most interesting physical systems that aren't an isolated molecule contain too many atoms to simulate with reasonable computational time. Even the nanostructures considered herein contain large amounts of atoms, for while they are on the scale

of several nanometers in one or two dimensions, they extend for hundreds of nanometers or more in the other dimensions. For example, the graphene nanoribbon seen in experiments in Chapter 6 is only 3 nm thick, but 82 nm wide and 300 nm long, containing nearly a million carbon atoms. In macroscopic bulk materials, of course, this problem is even worse, and, because computational time generally scales as the square of the number of atoms, it is highly desirable to reduce the number of atoms considered. For many decades, *periodic boundary conditions* (PBC) have been used for this purpose [4]. In PBC, only a subset of the atoms in the structure – the *simulation cell* – is treated independently. The rest of the structure is represented by *images* of the simulation cell – replicas which have the same coordinates as the atoms in the simulation cell, but translated by integer multiples of one or more translational vectors $\mathbf{T}_k$. The most general case is for three-dimensional bulk materials, in which case there are three vectors $\mathbf{T}_1, \mathbf{T}_2$, and $\mathbf{T}_3$. The full set of coordinates in the structure is then

$$\mathbf{X}_{i,\zeta_1,\zeta_2,\zeta_3} = \zeta_1\mathbf{T}_1 + \zeta_2\mathbf{T}_2 + \zeta_3\mathbf{T}_3 + \mathbf{X}_{i,0,0,0}, \quad i = 1, ..., n_T, \tag{2.3}$$

where $\mathbf{X}_{i,0,0,0}$ are the coordinates of the atom i contained in the simulation cell, n_T is the number of atoms in the simulation cell, ζ_1, ζ_2, and ζ_3 are the integers designating the images, and $\mathbf{X}_{i,\zeta_1,\zeta_2,\zeta_3}$ are the coordinates of the copy of atom i in the corresponding image. If the simulation is dynamic, the velocity of the atom i in the images is identical to the velocity of atom i in the simulation cell:

$$\mathbf{v}_{i,\zeta_1,\zeta_2,\zeta_3} = \mathbf{v}_{i,0,0,0}, \quad i = 1, ..., n_T. \tag{2.4}$$

ζ_k run from some $-N_k$ to N_k. In the general abstract view, typically $N_k \to \infty$, as the system being simulated is infinite bulk. In practice, some finite number of images is considered. The entire premise of PBC is that the simulation cell and the images are identical, as well as existing in identical environments. Thus, the potential energy only needs to be evauated for the simulation cell to obtain a value of energy per cell. The potential energy function, or *interatomic potential* is expressed as a set of atom-centered contributions,

$$E = \sum_{i=1}^{n_T} E_i, \tag{2.5}$$

where the E_i depend on the local environment of atom i. Thus, in computations, N_k only needs to be large enough that all of the images that would fall within the cutoff range of the interatomic potential around each atom in the simulation cell are present.

If the system being simulated is a crystalline solid, then the T_k vector(s) make explicit recourse to the translational symmetry of the crystal lattice, including an integer number of crystal unit cells within the simulation cell. All of the simulations in this dissertation consider crystalline solids, although amorphous solids, liquids and gases may be simulated using PBC as well.

Fig. 2.2 is an illustration of a PBC simulation of a crystal with a two-dimensional square lattice that is periodic in one dimension:

$$\mathbf{X}_{i,\zeta} = \zeta\mathbf{T} + \mathbf{X}_{i,0}, \quad i = 1, ..., n_T \tag{2.6}$$

$$\mathbf{v}_{i,\zeta} = \mathbf{v}_{i,0}, \quad i = 1, ..., n_T. \tag{2.7}$$

One-dimensional PBC can represent, for example, a nanotube or a nanowire. While the restriction that the images follow the motion of the simulation cell may seem unnatural, it can be shown that as long as the initial conditions of the system follow this symmetry, the solution to equation 2.2 will follow the symmetry for any future point in time [41]. The exact choice of the size of simulation cell will depend on the phenomenon being studied. For formation energies and elastic properties of ideal crystals, the simulation cell can be as small as the crystal unit cell. For example, for these purposes, $\mathbf{T}$ in Fig. 2.2 can be reduced to the distance between two circles, and the simulation cell can be reduced to three circles in a horizontal line. For other phenomena, the simulation cell needs to be larger than the relevant length scale. Consider, for example, studying a vacancy in the crystal depicted in Fig. 2.2. It is desirable to study the vacancy in an otherwise perfect crystal, but when a vacancy is created in the simulation cell, PBC will repeat it in the images. Thus, in order to approximate the behavior of an isolated vacancy, the simulation cell must be large enough that the vacancy in the simulation cell does not interact with the vacancies in the images. This is illustrated in Fig. 2.3. Precisely speaking, the vacancies will interact no matter how large the simulation cell is, as they will cause asymptotically decaying deformations in the crystal lattice. It is up to the investigator to decide at what distance the interaction can be considered

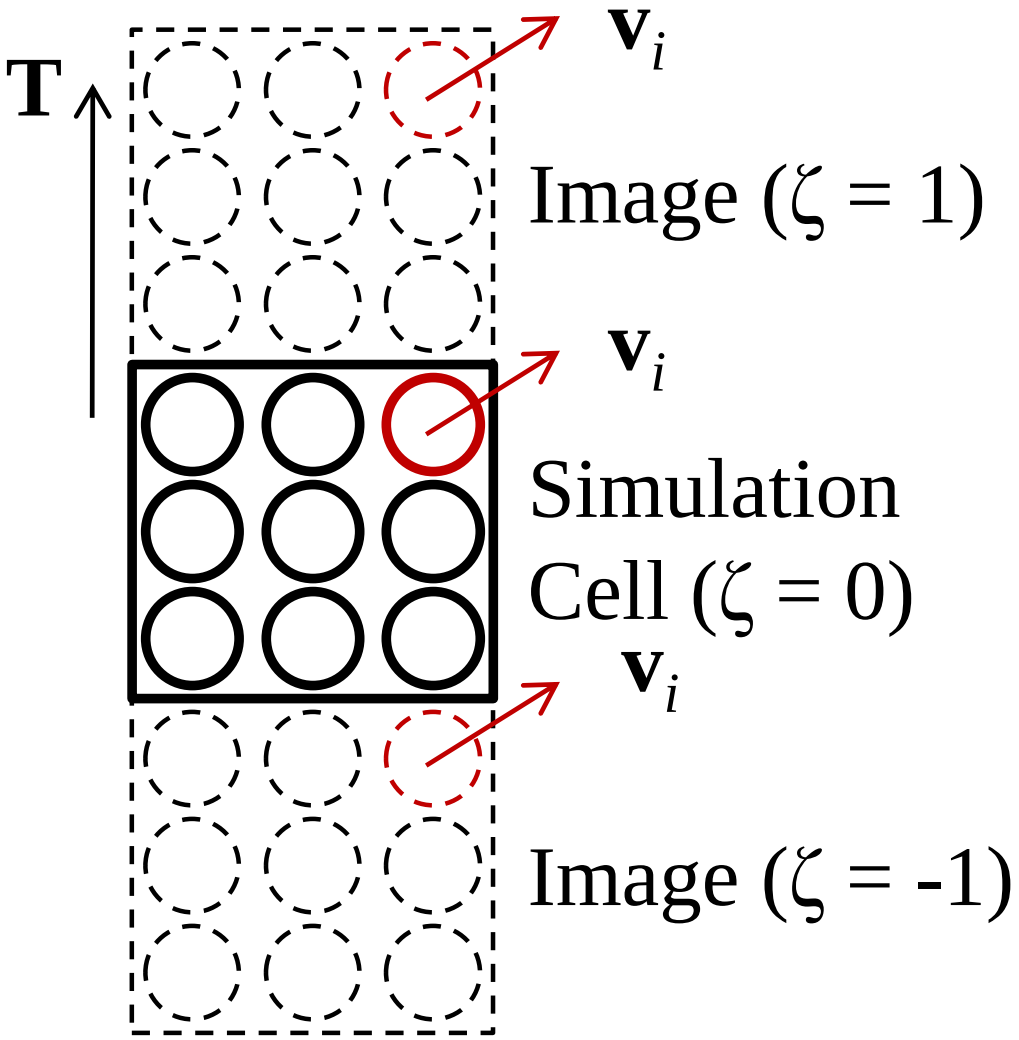

Figure 2.2: Represenation of a molecular dynamics simulation with periodic boundary conditions in one dimension. Solid circles represent atoms in the simulation cell. Dashed circles represent images. **T** designates the translational vector, ζ is the index labeling the simulation image, and $\mathbf{v}_i$ is the velocity of atom i and its images.

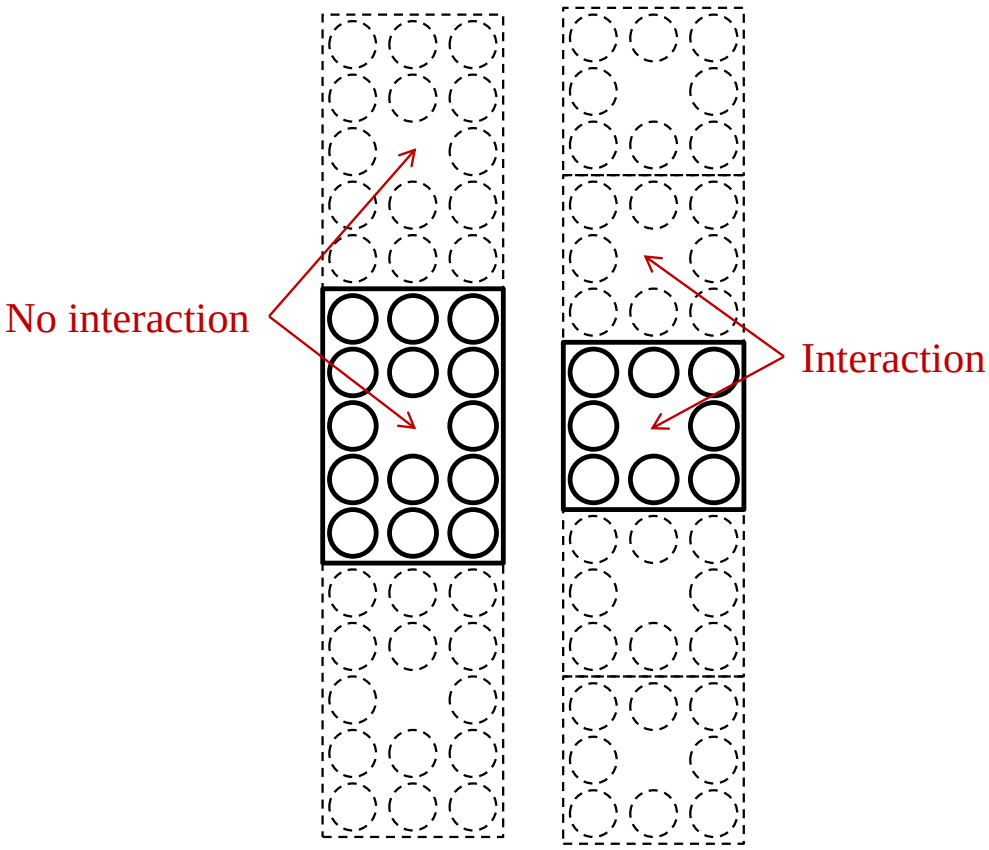

Figure 2.3: Demonstration of the process of selecting a simulation cell size. The simulation on the right is unsuitable for approximating the behavior of an isolated vacancy – the vacancies in the simulation cell will interact with their images because the cell size is too small. The simulation on the left is suitable, because the simulation cell is large enough to avoid this interaction. Note that the simulation on the right may still be used if the interaction is a desired effect.

negligible. Other selection criteria for the simulation cell size include the simulation of thermal phenomena, in which case the simulation cell must be larger than the phonon mean free path, and the simulation of liquids and gases, in which case the cell must be larger than the particle mean free path.

2.3 Objective Molecular Dynamics

Objective molecular dynamics (OMD) is a generalization that allows calculations to take advantage of rotational and/or helical symmetries in the structure of interest, as opposed to only translational symmetry[41].[1] This method is applicable to a wide variety of molecular structures from the nano- and bio-science areas, united under the concept of objective structures [40]. Examples of such structures are carbon nanotubes and other nanostructures now being synthesized, including screw-dislocated nanowires [65], the tails and capsids of many viruses [89], ideal DNA, and amyloid fibrils.

As a generalization of PBC, the repeating rules used to obtain the coordinates of the images from the coordinate cells are no longer restricted to pure translations. Each operation can now be a pure translation, a pure rotation – an *angular* operation – or a combination of the two – a *helical* operation. This creates a myriad of possibilities for describing structures. Here, the description is restricted to the case of one helical operation, termed h, and one angular operation, termed g. The two operations are coaxial. This is nowhere near the most general case possible, but it is the most general case used here – in Chapter 4. In the other chapters, the symmetries are even further specializations of this case. This only demonstrates the power of the method – even with such a restricted case, a wide variety of nanostructures can be simulated. Operation h consists of a translation of magnitude T along the z-axis combined with a rotation of angle γ around the z-axis, while operation g is a rotation of angle ψ around the z-axis:

[1] A note on terminology – "objective molecular dynamics" is the general name for the method. Thus, the method is termed "OMD" even when the simulations are not dynamic.

$$\mathbf{X}_{i,\zeta_h,\zeta_g} = \zeta_h \mathbf{T} + \mathbf{R}_\gamma{}^{\zeta_h} \mathbf{R}_\psi{}^{\zeta_g} \mathbf{X}_{i,0,0} \tag{2.8}$$

$$\mathbf{T} \equiv \begin{bmatrix} 0 \\ 0 \\ T \end{bmatrix}$$

$$\mathbf{R}_\gamma \equiv \begin{bmatrix} \cos\gamma & -\sin\gamma & 0 \\ \sin\gamma & \cos\gamma & 0 \\ 0 & 0 & 1 \end{bmatrix}$$

$$\mathbf{R}_\psi \equiv \begin{bmatrix} \cos\psi & -\sin\psi & 0 \\ \sin\psi & \cos\psi & 0 \\ 0 & 0 & 1 \end{bmatrix}.$$

Fig. 2.4, repeated from Chapter 4, shows an example of how these symmetries can be used to describe a structure. In this example, a (20,10) carbon nanotube is being simulated using just two atoms in the simulation cell. It is self-evident that this is a significant simplification compared to PBC. In this case, in order to simulate the same carbon nanotube with PBC, 140 atoms would be required. In general, because OMD is a generalization of PBC, the number of atoms required to simulate a given structure using OMD is less than or equal to the number required using PBC. In some cases, PBC cannot simulate a structure at all. The specific advantages of OMD over PBC for each structure studied herein are outlined in their respective chapters.

In the case of a dynamic simulation, the treatment of the velocities is complicated somewhat by the presence of the rotations. The velocities of the images are not identical to the velocities of the simulation cell as in PBC. Instead, they must be rotated as the coordinates are:

$$\mathbf{v}_{i,\zeta_h,\zeta_g} = \mathbf{R}_\gamma{}^{\zeta_h} \mathbf{R}_\psi{}^{\zeta_g} \mathbf{v}_{i,0,0}. \tag{2.9}$$

Also, there is a computational caveat regarding the forces. The force on atom i, $\mathbf{f}_i$, is defined as $\mathbf{f}_i = \sum_{n=1}^{N_n} \mathbf{f}_{in}$. Here, n indicates *neighbor* n of atom i, and $\mathbf{f}_{in}$ is the force on atom i due to neighbor n. The neighbors of atom i are either an atom j in the simulation cell, or an image of an atom j. In the interest of computational efficiency, the

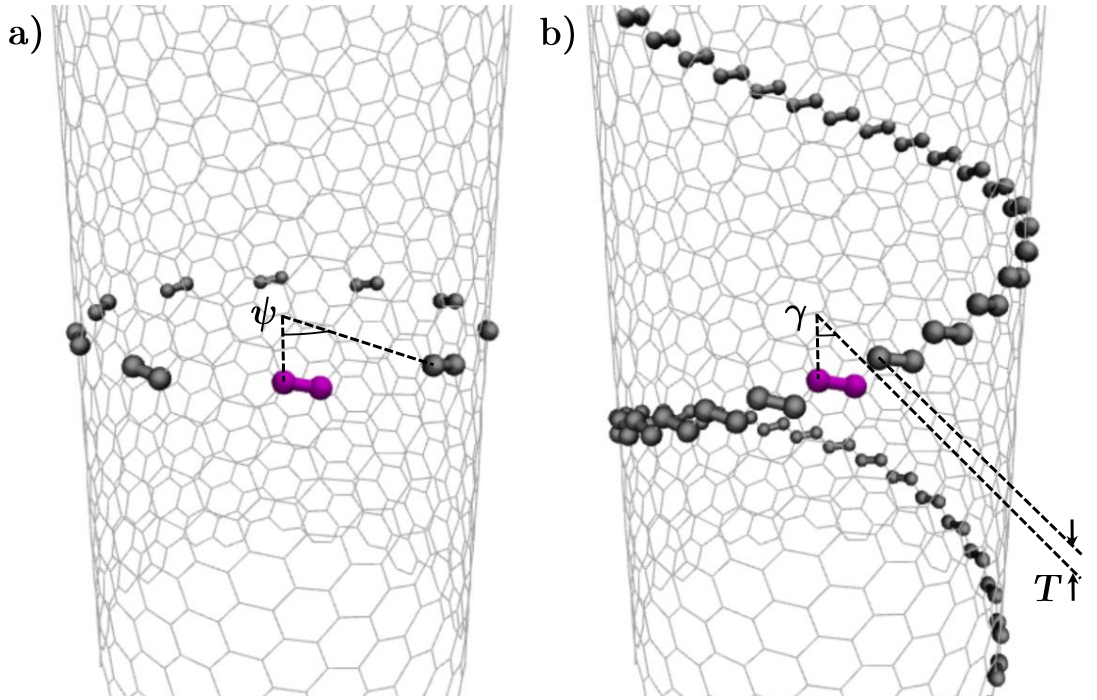

Figure 2.4: Symmetries used in the OMD simulations, for the case of a (20,10) CNT. (a) Operation g – pure rotation around CNT axis of angle ψ. (b) Operation h – rotation around CNT axis of angle γ combined with translation T along CNT axis.

sum is only accumulated when $i \geq j$, and Newton's third law is invoked, accumulating the force back onto the the atom j that n represents, directly or as an image. This is the case in PBC as well. However, in OMD, if n is an image of atom j, the force must be rotated. Thus, the force that is accumulated back onto atom j is $-\mathbf{R}_\gamma{}^{-\zeta_h}\mathbf{R}_\psi{}^{-\zeta_g}\mathbf{f}_{in}$.

In the most rigorous treatment, the presence of a purely angular operation has some implications. The helical operation h is analogous to the translational operations in the PBC case, and $-\infty < \zeta_h < \infty$. However, in the angular direction, the structure is always finite, as the the images will begin to coincide once the total angle in the angular direction exceeds 2π ($|\zeta_g\psi| > 2\pi$). This also means that the angle ψ must be 2π divided by an integer, $\psi = 2\pi/N_g$, where N_g is the total number of images considered in the angular direction, including the simulation cell. One can concieve some esoteric case where this is not true, and the simulation cell is rotated to angles greater than 2π without overlapping to reach some desired atomic coordinates, but such cases are not used herein or in any work the author is familiar with. More pertinently, in the case when a classical potential is used and OMD is used as a method to apply a bending deformation to the simulation cell, only the local environment around the simulation cell is of interest. Thus, the restriction on ψ may be lifted in order to apply arbitrary bending angles. This is used in Chapter 6 and has been previously used in Ref. [60].

The remarks regarding the choice of simulation cell size from Sec. 2.2 apply to OMD as well – the simulation cell choice must be informed with the nature of the phenomenon being studied. An example of the multi-layer graphene simulations carried out in Chapter 6 can be seen in Fig. 2.5. Case (a) uses the minimum possible cell – four atoms per layer. This forces the bending to be smooth. Case (b) uses a much larger cell in the bending direction. This enables study of localized buckling. The large cells not only allow the buckling to occur in the first place, but are large enough that the buckles do not interact with each other. Thus, the obtained behavior accurately represents the behavior of the buckles when they are isolated in an otherwise smoothly bent nanoribbon.

Figure 2.5: Demonstration of the process of selecting a simulation cell size in OMD. Simulation (a) unsuitable for approximating the behavior of an isolated buckle – the symmetry prevents it and forces the bending to be smooth. Simulation (b) is suitable, because the simulation cell is large enough to allow the buckling to occur, and to prevent the buckles from interacting with each other.

2.4 Density Functional-Based Tight-Binding

Tight-binding is a venerable method of treating interatomic interactions in a way that is explicitly quantum-mechanical, yet computationally simple. In fact, for simple structures, computations may even be performed by hand. It is conceptually analogous to linear combination of atomic orbitals (LCAO), the nomenclature difference indicating different sources for the parameters used[37]. The flavor of tight-binding used here, DFTB, *density functional-based* tight binding, sources these parameters from first-principles density functional theory (DFT), and is treated as an expansion approximation of DFT. In DFT, the energy of the system is written as a functional of a charge density $n(\mathbf{r}) = \sum_{\lambda}^{occ} \Psi_{\lambda}^{*}(\mathbf{r})\Psi_{\lambda}(\mathbf{r})$ (the sum runs over all occupied one-electron states), where $\Psi_{\lambda}(\mathbf{r})$ is the wavefunction of the λ-th state. The energy, is[109, 5] (atomic units)

$$E = \sum_{\lambda}^{occ} \langle \Psi_{\lambda} | -\frac{\nabla}{2} + V_{ext} + \frac{1}{2}\int' \frac{n(\mathbf{r}')}{|\mathbf{r}-\mathbf{r}'|} |\Psi_{\lambda}\rangle + E_{XC}[n(\mathbf{r})] + E_{ii}. \tag{2.10}$$

The bra-ket notation indicates integration over all space with respect to $\mathbf{r}$, and $\int'$ is shorthand for integration over all space with respect to $\mathbf{r}'$. The first two terms within the bra-ket are the usual one-electron Hamiltonian – the kinetic energy operator and the electrostatic potential due to the ions (the Born-Oppenheimer approximation has aleady been made, so the electrons are considered to exist in a static potential created by the ions). The third term within the bra-ket is the Hartree functional – the electrostatic potential due to electron-electron repulsion. The second-to-last term is the exchange-correlation functional. It can be approximated in the local-density approximation (LDA) as $E_{XC} \approx \int V_{XC}(n(\mathbf{r}))n(\mathbf{r})$ ($\int$ is shorthand for integration over all space with respect to $\mathbf{r}$)[5]. The final term is the ion-ion electrostatic repulsion E_{ii}. DFTB is treated as an approximation to Eq. 2.10. To begin the approach to this approximation, consider an electron density $n(\mathbf{r}) = n_0(\mathbf{r}) + \delta n(\mathbf{r})$, where n_0 is some known reference density and $\delta n(\mathbf{r})$ is a small variation that preserves normalization: $\int \delta n(\mathbf{r}) = 0$[5]. The energy functional can then be rewritten as[109]

$$E = \sum_{\lambda}^{occ} \langle \Psi_\lambda | \hat{H}_0 | \Psi_\lambda \rangle$$
$$-\frac{1}{2} \int \int' \frac{n_0(\mathbf{r}') n_0(\mathbf{r})}{|\mathbf{r} - \mathbf{r}'|} - \int V_{XC}(n_0(\mathbf{r})) n_0(\mathbf{r})$$
$$+E_{XC}[n_0(\mathbf{r})] + E_{ii} + O([\delta n(\mathbf{r})]^2). \tag{2.11}$$

The first term is simply the sum of the single-electron energies of the occupied states, where $\hat{H}_0 \equiv -\frac{\nabla}{2} + V_0$ is the single-particle Hamiltonian due to a ficticious potential V_0, which produces single-electron eigenstates Ψ_λ, $H_0 \Psi_\lambda = \epsilon_\lambda^0 \Psi_\lambda$, such that $\sum_\lambda^{occ} \Psi_\lambda^*(\mathbf{r}) \Psi_\lambda(\mathbf{r}) = n_0$. This potential includes effects from the Hartree and exchange-correlation functionals, so the second and third terms remove the double-counting of these energies. In standard DFTB, the $O([\delta n(\mathbf{r})]^2)$ term is omitted. This term is included in SCC-DFTB and is revisited in Sec. 5.3. Now, all of the terms except $\sum_\lambda^{occ} \langle \Psi_\lambda | \hat{H}_0 | \Psi_\lambda \rangle$ are absorbed into a single pairwise repulsive potential, $E_{rep} = \sum_{ij} E_{pair}(X_{ij})$, where the sum runs over all ions (atoms) i and j and X_{ij} is the interatomic distance. E_{pair} is a short-range spline or polynomial fitted to reproduce (in combination with $\sum_\lambda^{occ} \langle \Psi_\lambda | \hat{H}_0 | \Psi_\lambda \rangle$) DFT energies for reference calculations. Also, in DFTB, only the valence electrons are treated expicitly. The effect of the core electrons on each atom is also absorbed into E_{pair}. Now, the remaining task is to approximate $\sum_\lambda^{occ} \langle \Psi_\lambda | \hat{H}_0 | \Psi_\lambda \rangle$.

This is where tight binding or LCAO enters the picture. The single-electron wavefunctions Ψ_λ are approximated as Φ_λ, which is a linear combination of atom-centered, atomic-*like* orbitals [6] (as will be seen below, the orbitals themselves do not enter the energy calculation, only precomputed interactions between them):

$$|\Phi_\lambda\rangle = \sum_{i,\alpha} c_{i\alpha}^\lambda |\phi_{i\alpha}\rangle \tag{2.12}$$

Here, the sum runs all of the atoms i to be considered, and over all of the atomic-like orbital symmetries α. For example, here α will run over the set s, p_x, p_y, p_z.[2] Then, $|\phi_{i\alpha}\rangle = \phi_{i\alpha}(\mathbf{r}) = \phi_\alpha(\mathbf{r} - \mathbf{X}_i)$ is the wavefunction of the atomic-like orbital α centered

[2] The treatments for d and f orbitals are analogous but *much* more messy mathematically, and will not be presented here.

on atom i located at $\mathbf{X}_i$, and the constants $c_{i\alpha}^{\lambda}$ are to be determined (λ is an index, not a power). Now, the variational method, introduced in most basic quantim mechanics texts [7], is used. It states that if one guesses a wavefunction Φ, then the quantity $\frac{\langle\Phi|\hat{H}|\Phi\rangle}{\langle\Phi|\Phi\rangle}$ will be greater to or equal to the actual ground state energy corresponding to the ground state eigenfunction Ψ of the system described by the Hamiltonian $\hat{H}$, with the equality holding if and only if $\Phi = \Psi$. Thus, by introducing parameters into the guess Φ and minimizing $\frac{\langle\Phi|\hat{H}|\Phi\rangle}{\langle\Phi|\Phi\rangle}$ with respect to those parameters, one may approximate the ground-state energy of the system. Here it is applied by minimizing the approximate single-electron energies

$$\epsilon_\lambda = \frac{\langle\Phi_\lambda|\hat{H}_0|\Phi_\lambda\rangle}{\langle\Phi_\lambda|\Phi_\lambda\rangle} \tag{2.13}$$

with respect to the LCAO coefficients $c_{i\alpha}^{\lambda}$. To do this, the inegrals in Eq. 2.13 must be calculated and expressed in terms of $c_{i\alpha}^{\lambda}$. Invoking Eq. 2.12, the numerator of Eq. 2.13 becomes

$$\langle\Phi_\lambda|\hat{H}_0|\Phi_\lambda\rangle = \sum_{i\alpha j\beta} c_{i\alpha}^{\lambda *} c_{j\beta}^{\lambda} \langle\phi_{i\alpha}|\hat{H}_0|\phi_{j\beta}\rangle \tag{2.14}$$

and the denominator becomes

$$\langle\Phi_\lambda|\Phi_\lambda\rangle = \sum_{i\alpha j\beta} c_{i\alpha}^{\lambda *} c_{j\beta}^{\lambda} \langle\phi_{i\alpha}|\phi_{j\beta}\rangle, \tag{2.15}$$

where the quadruple sums run over all atoms i and j and over all atomic-like orbital symmetries α and β. The integrals $\langle\phi_{i\alpha}|\hat{H}_0|\phi_{j\beta}\rangle$ and $\langle\phi_{i\alpha}|\phi_{j\beta}\rangle$ are defined as the *hamiltonian matrix elements* $\mathbf{H}_{i\alpha j\beta}$ and *overlap matrix elements* $\mathbf{S}_{i\alpha j\beta}$, respectively. Optimizing ϵ_λ with respect to $c_{i\alpha}^{\lambda *}$, after substituting Eqs. 2.14 and 2.15 into Eq. 2.13, it can be shown with some algebra that[6] requiring $\frac{\partial\epsilon_\lambda}{\partial c_{i\alpha}^{\lambda *}} = 0$ for any i, α is equivalent to requiring that $\mathbf{H}\mathbf{c}^{\lambda} = \epsilon_\lambda \mathbf{S}\mathbf{c}^{\lambda}$, where $\mathbf{H}$ is the $M \times M$ Hamiltonian matrix built from $\mathbf{H}_{i\alpha j\beta}$, $\mathbf{S}$ is the $M \times M$ overlap matrix built from $\mathbf{S}_{i\alpha j\beta}$, and $\mathbf{c}^{\lambda}$ is the M-dimensional vector of coefficients built from $c_{i\alpha j\beta}^{\lambda}$. M is the total number of atomic-like orbitals considered on all atoms considered. Thus, the allowed single-electron energies are obtained from solving a generalized eigenvalue equation, of which there will be M solutions (indexed by λ). Finally, the ground state electronic energy E_{el} of the system is obtained by

filling the the bottom λ_{occ} allowed states, where λ_{occ} is the number of occupied states, $E_{el} = \sum_{\lambda=1}^{\lambda_{occ}} \epsilon_\lambda$.

Now, all that remains is to compute the matrix elements (easier said than done!) The potential V_0 is now expressed as a superpostition of atom-centered terms, $V_0(\mathbf{r}) = \sum_i V_i(\mathbf{r} - \mathbf{X}_i)$, where V_i is the potential centered at atom i located at $\mathbf{X}_i$. Thus, $\hat{H}_0 = -\frac{\nabla}{2} + \sum_i V_i$.[6] The Hamiltonian matrix elements then write

$$\mathbf{H}_{i\alpha j\beta} = \langle \phi_{i\alpha} | -\frac{\nabla}{2} | \phi_{j\beta} \rangle + \sum_k \langle \phi_{i\alpha} | V_k | \phi_{j\beta} \rangle. \tag{2.16}$$

Now, the *two-center approximation* is made [6, 109]. All terms in the sum over k are neglected, except when $k = i$ and/or $k = j$. When $i = j$, the orbitals are centered on the same atoms. In that case, the matrix elements $\mathbf{H}_{i\alpha i\beta}$ and $\mathbf{S}_{i\alpha i\beta}$ are fixed parameters – they are the values of the integrals evaluated *a priori* using DFT for isolated atoms. The remaining matrix elements are interactions between orbitals on two different atoms i and j, under the influence of the potential components V_i and V_j. It is desirable to express these matrix elements in terms of integrals evaluated *a priori* using DFT, which are only dependent on the interatomic distance $\mathbf{X}_{ij}$. When both of the orbitals being considered are s orbitals, this is straightforward – s orbitals are spherically symmetric, and their interaction is indeed purely distance-dependent, $\mathbf{H}_{isjs} = \mathbf{H}_{ss}(X_{ij})$ and $\mathbf{S}_{isjs} = \mathbf{S}_{ss}(X_{ij})$. These functions are stored as tables and interpolated as needed when the tight-binding matrices are calculated. When an s orbital interacts with a p orbital, however, the interaction depends not only on the interatomic distance X_{ij} but also on the direction of the interatomic vector (the unit vector $\hat{\mathbf{X}}_{ij}$). Here, the concept of *orbital decomposition* is invoked[6] (also used in Sec. 4.2 to analyze the quantum chemistry of graphene bending). Consider a p orbital that lies along cartesian unit vector $\hat{\mathbf{a}}$. For example, for p_x, $\hat{\mathbf{a}} = \hat{\imath}$. This orbital can be expressed as a linear combination of two p orbitals, one that lies along $\hat{\mathbf{X}}_{ij}$, and one that is perpendicular to $\hat{\mathbf{X}}_{ij}$. These are termed p_σ and p_π, respectively, after the quantum chemistry concepts of σ and π bonds. Because of orbital symmetry, the Hamiltonian and overlap integrals between an s and a p_π orbital are always zero, while the integrals between an s and a p_σ orbital are a dependent only on X_{ij} and can be precomputed with DFT and stored as $\mathbf{H}_{sp_\sigma}(X_{ij})$ and $\mathbf{S}_{sp_\sigma}(X_{ij})$. Formally, then,

$$\begin{aligned}
\mathbf{H}_{isjp_a} &= \langle\phi_{is}|\hat{H}_0|\phi_{jp_a}\rangle = \langle\phi_{is}|\hat{H}_0(c_\sigma|\phi_{jp_\sigma}\rangle + c_\pi|\phi_{jp_\pi}\rangle) \\
&= c_\sigma\langle\phi_{is}|\hat{H}_0|\phi_{jp_\sigma}\rangle = c_\sigma\mathbf{H}_{sp_\sigma}(X_{ij}) \\
\mathbf{S}_{isjp_a} &= \langle\phi_{is}|\phi_{jp_a}\rangle = \langle\phi_{is}|(c_\sigma|\phi_{jp_\sigma}\rangle + c_\pi|\phi_{jp_\pi}\rangle) \\
&= c_\sigma\langle\phi_{is}|\phi_{jp_\sigma}\rangle = c_\sigma\mathbf{S}_{sp_\sigma}(X_{ij}),
\end{aligned} \tag{2.17}$$

where c_π is some unused constant and $c_\sigma = \hat{\mathbf{a}}\cdot\hat{\mathbf{X}}_{ij}$, from the vector algebra involved in the orbital decomposition. For interaction between two p orbitals, the situation is analogous, but more complex. Each orbital is decomposed into three components, each laying along the axis of a Cartesian coordinate system (same for both atoms in the pair) rotated so that one of its axes, the σ-bond axis, lies along $\hat{\mathbf{X}}_{ij}$. The other two axes are π-bond axes, call them π_1 and π_2. Orbital symmetry means the only nonzero integrals are between like components, so when the integrals are computed as in Eq. 2.17 only three terms will survive, each of which is a constant arising from the vector algebra involved in the decomposition multiplied by a pre-computed distance-dependent term (which is the same for both π axes), e.g.

$$\begin{aligned}
\mathbf{H}_{isjp_a} &= c_\sigma\mathbf{H}_{p_\sigma p_\sigma}(X_{ij}) + c_{\pi_1}\mathbf{H}_{p_\pi p_\pi}(X_{ij}) + c_{\pi_2}\mathbf{H}_{p_\pi p_\pi}(X_{ij}) \\
\mathbf{S}_{isjp_a} &= c_\sigma\mathbf{S}_{p_\sigma p_\sigma}(X_{ij}) + c_{\pi_1}\mathbf{S}_{p_\pi p_\pi}(X_{ij}) + c_{\pi_2}\mathbf{S}_{p_\pi p_\pi}(X_{ij}).
\end{aligned} \tag{2.18}$$

This completes the discussion of the evaluation of the matrix elements, and is all the information needed to evaluate the tight-binding energy.

2.4.1 Periodic Systems

The preceding discussion makes no recourse to any periodicity and is only suitable for an isolated system simulated in its entirety. It is clear that the repulsive energy E_{rep} will simply be evaluated by considering additional neighbors in adjacent images, but how is the electronic energy E_{el} treated with tight-binding? Bloch's theorem states that for a solid with translational periodicity, the allowed wavefunctions satisfy[104]

$$\Psi^\lambda(\mathbf{r}+\mathbf{T}) = e^{i\mathbf{k}\mathbf{T}}\Psi^\lambda(\mathbf{r}). \tag{2.19}$$

Here, $\mathbf{T} = \zeta_1\mathbf{T}_1 + \zeta_2\mathbf{T}_2 + \zeta_3\mathbf{T}_3$ is some linear combination of integer multiples of the translational vectors of the system. $\mathbf{k}$ is the wavevector of an electron in the structure. To satisfy Eq. 2.19 under tight-binding, so-called *Bloch sums*, or *crystal-like wavefunctions* (as opposed to atomic-like wavefunctions) $|\varphi^{\mathbf{k}}_{i\alpha}\rangle$ can be constructed for each orbital $i\alpha$ in the simulation cell[6]:

$$\varphi^{\mathbf{k}}_{i\alpha}(\mathbf{r}) = N_T^{-1/2}\sum_{\mathbf{T}} e^{i\mathbf{k}\mathbf{T}}\phi_{i\alpha}(\mathbf{r}-\mathbf{T}). \tag{2.20}$$

Here, the sum over all allowed values of $\mathbf{T}$ (including zero). So, instead of a single atomic-like orbital of type α, the Bloch sum is a linear superposition of atomic-like orbitals of type α, centered on all the possible images of atom i, multiplied by the complex factor $e^{i\mathbf{k}\mathbf{T}}$. N_T is the total number of translational cells in the full structure, so $N_T \to \infty$. It will cancel out shortly. The treatment proceeds exactly the same as before, except the atomic-like orbitals $|\phi^{\mathbf{k}}_{i\alpha}\rangle$ are replaced with $|\varphi^{\mathbf{k}}_{i\alpha}\rangle$. Because the latter are linear superpositions of the same types of orbitals, all of the same procedures, approximations and decompositions apply, except now there is a separate generalized eigenvalue problem, complete with a unique Hamiltomian matrix, overlap matrix, and solution for each $\mathbf{k}$ point in the first Brillouin zone.[3] . The $\mathbf{k}$-dependent Hamiltonian and overlap matrix elements are

$$\begin{aligned}\mathbf{H}^{\mathbf{k}}{}_{i\alpha j\beta} &= \langle\varphi^{\mathbf{k}}_{i\alpha}|\hat{H}_0|\varphi^{\mathbf{k}}_{j\beta}\rangle \\ \mathbf{S}^{\mathbf{k}}{}_{i\alpha j\beta} &= \langle\varphi^{\mathbf{k}}_{i\alpha}|\varphi^{\mathbf{k}}_{j\beta}\rangle\end{aligned} \tag{2.21}$$

Substituting Eq. 2.20 into Eq. 2.21 yields, after some algebra,

$$\begin{aligned}\mathbf{H}^{\mathbf{k}}{}_{i\alpha j\beta} &= \sum_{\mathbf{T}} e^{i\mathbf{k}\mathbf{T}}\langle\phi_\alpha(\mathbf{r}-\mathbf{X}_i)|\hat{H}_0|\phi_\beta(\mathbf{r}-\mathbf{T}-\mathbf{X}_j)\rangle \\ \mathbf{S}^{\mathbf{k}}{}_{i\alpha j\beta} &= \sum_{\mathbf{T}} e^{i\mathbf{k}\mathbf{T}}\langle\phi_\alpha(\mathbf{r}-\mathbf{X}_i)|\phi_\beta(\mathbf{r}-\mathbf{T}-\mathbf{X}_j)\rangle\end{aligned} \tag{2.22}$$

[3] Reciprocal space, where the wavevectors $\mathbf{k}$ live, is periodic, with translational symmetry related to the translational symmetry of the crystal lattice. The *Brillouin zone* is essentially the unit cell in reciprocal space, and contains all unique solutions to the $\mathbf{k}$-dependent electronic problem

The summands, then, are computed in the same way as the Hamiltonian and overlap matrix elements for the isolated structure and then multiplied by the phase factor $e^{i\mathbf{k}\mathbf{T}}$, except the location $\mathbf{X}_j$ of atom j is shifted by some translational vector $\mathbf{T}$. Because the two-center integrals decay with distance, the sums can be truncated. With these matrix elements, the generalized eigenvalue problem can be solved to obtain a set of eigenvalues $\epsilon_\lambda^{\mathbf{k}}$ for each $\mathbf{k}$. As before, the total energy is computed by summing the bottom λ_{occ} eigenvalues, where λ_{occ} is the number of occupied states per simulation cell, except now the procedure is done for each $\mathbf{k}$: $E_{el}^{\mathbf{k}} = \sum_{\lambda=1}^{\lambda_{occ}} \epsilon_\lambda^{\mathbf{k}}$. For an infinite structure, $\mathbf{k}$ is continuous, and the electronic energy per simulation cell is the integral of $E_{el}^{\mathbf{k}}$ over the first Brillouin zone. In practice, this integral evaluated by sampling $E_{el}^{\mathbf{k}}$ for a number of $\mathbf{k}$, and computing a weighed average.

The Bloch sum construction has been generalized to objective boundary conditions[8, 46]. Under OMD (restricted to helical-angular as in Eq. 2.8), the Bloch sums read

$$\varphi_{i\alpha}^{l\kappa}(\mathbf{r}) = (N_h N_g)^{-1/2} \sum_{\zeta_g,\zeta_h} e^{il\psi\zeta_g + i\kappa\zeta_h} \phi_{i\alpha}(\mathbf{R}_\psi^{-\zeta_g}\mathbf{R}_\gamma^{-\zeta_h}[\mathbf{r} - \zeta_h\mathbf{T}]), \tag{2.23}$$

where the helical symmetry operation g consisting of rotation $\mathbf{R}_\gamma$ and translation $\mathbf{T}$ (note that the meaning of $\mathbf{T}$ has changed compared to the PBC description, it is now a fixed vector and does not vary with the summation), and the angular operation g consisting of rotation $\mathbf{R}_\psi$ are defined in Eq. 2.8. The most obvious difference with PBC is that the operation which shifts the orbital includes rotations as well as a translation. This not only moves the location of the orbital, but also rotates the orbital. So, a p_a orbital that was aligned along $\hat{\mathbf{a}}$ becomes aligned along $\mathbf{R}_\psi^{\zeta_g}\mathbf{R}_\gamma^{\zeta_h}\hat{\mathbf{a}}$. κ is the wavenumber corresponding to the helical operation h, and it is normalized so that the first Brillouin zone is $-\pi \leq \kappa < \pi$, regardless of the parameters of the symmetry operations. Other than that difference, the helical operation h is treated completely analogously to a translational operation. The operation h is repeated infinitely, so $N_h \to \infty$, and κ is continuous. The operation g, however, is finite, as discussed in Sec. 2.3. Thus, $N_g = 2\pi/\psi$ and, because of the finite operation, l is *discrete*. The values of l that fall within the first Brillouin zone are $l = 0, 1, ..., (N_g - 1)$. The OMD equivalent of Eq. 2.22, the $l\kappa$-dependent matrix elements, are

$$\mathbf{H}^{l\kappa}_{i\alpha j\beta} = \sum_{\zeta_g,\zeta_h} e^{il\psi\zeta_g + i\kappa\zeta_h} \langle \phi_\alpha(\mathbf{r} - \mathbf{X}_i) | \hat{H}_0 | \phi_\beta(\mathbf{R}_\psi^{-\zeta_g} \mathbf{R}_\gamma^{-\zeta_h} [\mathbf{r} - \zeta_h \mathbf{T}] - \mathbf{X}_j) \rangle$$

$$\mathbf{S}^{l\kappa}_{i\alpha j\beta} = \sum_{\zeta_g,\zeta_h} e^{il\psi\zeta_g + i\kappa\zeta_h} \langle \phi_\alpha(\mathbf{r} - \mathbf{X}_i) | \phi_\beta(\mathbf{R}_\psi^{-\zeta_g} \mathbf{R}_\gamma^{-\zeta_h} [\mathbf{r} - \zeta_h \mathbf{T}] - \mathbf{X}_j) \rangle$$

Just as under PBC, the summands are computed in the same way as the Hamiltonian and overlap matrix elements for the isolated structure and then multiplied by the phase factor. This time the location $\mathbf{X}_j$ of atom j is moved according to the objective operations,[4] and the orbital β is rotated. The rotation does not complicate any of the procedures. After all, if a given orbital of type β can be decomposed into a linear combination of some basis orbitals, the same can be done to a rotated orbital of the same type. As before, the generalized eigenvalue equation is solved to get sets of $l\kappa$-dependent eigenvalues $\epsilon_\lambda^{l\kappa}$ and the occupied states are added together to get total $l\kappa$-dependent electronic energies $E_{el}^{l\kappa}$. The Brillouin zone in the κ direction is sampled like the PBC Brillouin zone. Because l is discrete, usually the average is taken of all of the allowed values in that direction.

Since non-SCC-DFTB has been coupled with objective MD, it has been successfully utilized to study homonuclear structures such as hexagonal, polycrystalline silicon nanowires [46], carbon nanotubes [47, 48, 83], graphene [16] and graphene nanoribbons [112], and often produced compelling results. As mentioned, it is used here in Chapters 3 and 4.

[4] Actually, $\mathbf{X}_j$ is the only vector that stays constant, but by applying the inverse of the objective symmetry operations to $\mathbf{r}$, essentially the entire coordinate system is moved, which has the same effect as moving the orbital $\phi_{j\beta}$ in the opposite manner

Chapter 3

Applications of non-SCC objective DFTB: Screw Dislocations in $\langle 110 \rangle$ Silicon Nanowires

Adapted with permission from I. Nikiforov, D.-B. Zhang, and T. Dumitrică, Screw Dislocations in ⟨100⟩[sic] Silicon Nanowires: An Objective Molecular Dynamics Study, *J. Phys. Chem. Lett.* **2**, 2544 (2011) (`http://pubs.acs.org/doi/abs/10.1021/jz201102h`) [111].

3.1 Introduction

Dislocations – the line imperfections in an ordered lattice – play a central role in the mechanical response and growth of three dimensional crystalline structures. In recent years there has been an increased practical interest in screw-dislocated nanowires (NWs) [65, 66, 67, 68, 70, 71, 69]. Unfortunately, there is little theoretical understanding about the structural and electronic properties of these structures. The reason for an axial screw dislocation to exist in a NW in the first place is its involvement in growth processes. The long known whisker crystallization induced by axial screw

dislocations [72] approach proved versatile enough to enable fabrication of NW from a variety of materials, including silicon [66], germanium [67], lead sulphide [68], lead selenide [69], and zinc oxide [70, 71]. The NW growth process occurs by incorporating atoms from the vapor or liquid along the fixed dislocation core.

In bulk, the crystalline region around the dislocation has a stabilizing effect on the structure and its deformation can be successfully described with classical continuum theory [73, 74]. However, the phenomenological theory fails to describe, via a logarithmic divergence, the energy of the high-distortion region close to the dislocation core. An effective method of modeling the energy of a dislocation is to use the continuum treatment, supplemented by an empirical core energy term E_c calculated from atomistic simulations. Most of the recent progress in determining E_c stems from advances in quantum mechanical microscopic calculations, parallel computing and hybrid continuum-atomic simulations [75, 78, 76, 77, 79]. When an infinite crystal contains a screw dislocation, the crystal lattice becomes distorted at finite distances from the core. This presents a challenge in atomistic modeling, as this prevents periodic boundary conditions from being able to accurately describe the atom positions. Three approaches are currently used in literature to overcome this issue: To simulate either a finite "cluster" representation of the dislocation core imposing the displacements expected from elasticity theory at its boundaries [78], a hybrid representation containing a "cluster" of atoms with its boundary conditions prescribed by a continuum region [79], or a dislocation dipole of zero net Burger's vector under PBC [75, 76, 77].

When considering a screw dislocated NW, an accurate prediction of the core becomes more important, because the size of the core is comparable to the size of the NW itself. Indeed, estimates for the core radius r_0 range from b to $5b$ [76, 73], where b is the magnitude of the Burger's vector – the vector describing the lattice distortion arising from the dislocation. Additionally, the interaction of the core with the surfaces should be considered. From a continuum perspective, a stable axial screw dislocation residing in a cylindrical rod (with a diameter order of magnitude larger than a NW), couples with twisting deformation known as the "Eshely twist" [74], Figure 3.1(a) and (b). This changes the normal translational symmetry of the nanowire to helical symmetry. Structures with helical symmetry, at best, require a much larger number of atoms to be studied with PBC, and, at worst, cannot be studied with PBC at all. The former

best-case scenario only holds for the discrete values of twist that are an integer multiple of 360° divided by an integer. Of course, any rational number satisfies this, but consider for example, a twist rate of 13.1° per helical objective cell. This would require 3600 helical cells until the periodic boundary conditions are regained – an intractable amount of atoms. The twist rate of a screw-dislocated nanowire is a continuous function of nanowire size, Burger's vector, and analytically-intractable atomistic effects arising in the core region. Thus, there is no reason to assume that the value of twist rate is the high-symmetry case that makes a PBC treatment possible, and continuous optimization over arbitrary values of twist rate is needed. Because of this, there is a void of theoretical explorations of screw dislocated NWs. By comparison, pristine NWs were intensely investigated [82, 80, 81, 46].

Here, this void is addressed using OMD. Hexagonal hydrogen-passivated silicon (Si) NWs with a $\langle 110 \rangle$ growth direction containing axial screw dislocations are considered. The simulation cells used herein contain 276 or less atoms, depending on nanowire diameter. Using the results from a wide range of atomistic calculations, E_c is calculated by modeling the NWs as elastic cylinders with a stress-free surface within the formulation of Eshelby [74]. This formulation, with E_c as the sole fitting parameter, is highly effective at predicting the dislocation energies. The choice of material (Si) for this initial study is motivated by the availability of a large number of experimental and simulation results on the structure and stability of dislocations in bulk Si. Specifically in Si, it was recognized that a screw dislocation in a $\langle 110 \rangle$ direction provides the (111)-plane layers with steps for Si NWs to grow continuously [84]. This is in agreement with the experimental availability of $\langle 110 \rangle$-oriented Si NWs [85, 66]. Nevertheless, the methodology used herein (objective MD implemented in the Trocadero [56, 46] simulation package coupled with density functional-based tight binding [86]) is sufficiently general to be applicable for other NW materials.

It is reasonable to expect that a NW would eject the dislocation to revert to the lower-energy pristine configuration, but there is direct evidence that they remain stable [66, 67]. One explanation for this surprising effect invokes the oxide layer that will always be surrounding these NW. The stress associated with this layer may cancel the image force associated with vacuum [73]. Alternatively, the aforementioned elastic theory predicts that a dislocation will be stable at the center of a cylinder with stress-free

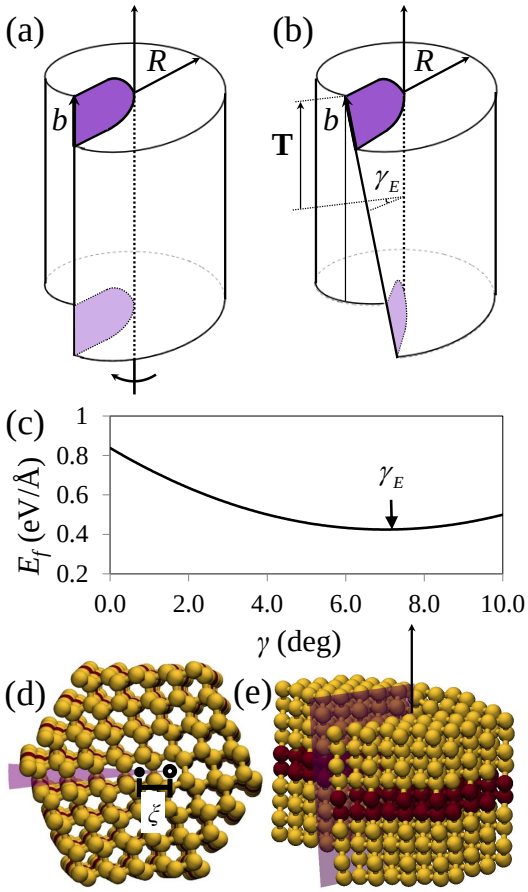

Figure 3.1: Schematics of a screw-dislocated cylinder with Burgers vector b with (a) fixed ends and (b) one free-to-rotate end leading to Eshelby twist. (c) Example of determination of optimal twist rate, in this case for a NW with n_L =4, R =6.27 Å, ξ =0, b =3.84 Å. (d) Axial and (e) side view of a NW supercell, omitting hydrogen atoms. The purple plane represents the cut made to create the dislocation. Note the intrinsic twist. The atoms in the simulation cell are represented in maroon. The unfilled circle represents the dislocation axis. The ⟨110⟩ axial direction is normal to the page in (d). The NW pictured has n_L =8, R =12.54 Å, ξ =3.32 Å, b =3.84 Å.

surfaces, but only when it is allowed to undergo Eshelby twist [74]. The simulations show in remarkable detail the validity of the latter possibility in spite of the nanoscale dimensions. The movement of dislocations in both twisted and straight NW is investigated and it is shown that the dislocation is stable in the center for a twisted NW, but unstable for a straight NW. The agreement between the simulations and the elastic theory supplemented by E_c is exemplified in Fig. 3.2, showing the energy of a dislocation as it shifts its axis radially in a twisted or straight NW, Fig. 3.2(a), as well as the optimal twist, Fig. 3.2(b). These results clearly reveal the importance of accurate accounting for the intrinsic NW twist - without it, one cannot have a stable dislocation in a NW with a stress-free surface. The twist rate can reach values well in excess of 1 deg/Å.

3.2 Simulation Details

Because ⟨110⟩-oriented NWs have surface planes of different orientation, the hexagonal cross section is not regular. In this study, the number of (111) layers in the cross-section, n_L, was varied from 4 to 12 in steps of 2. Because the NWs are not cylindrical, the NW radius R was approximated as $d_{111}n_L/2$, where d_{111} is the (111) plane spacing, 3.14 Å. The radii, then, ranged from 6.27 Å to 18.81 Å. The NWs considered contained "shuffle"-type screw dislocations with Burger's vectors b of 3.843 Å, as well as double and triple that magnitude. To rationalize the core-NW surface interaction, the location of the Hornstra dislocation core was varied, being placed at the NW center as well as at a distance ξ from the core, Fig. 3.1(a).

The objective boundary conditions employed here consist solely of the helical operation h – the combination of a translation of magnitude T along the z-axis a rotation of angle γ around the z-axis. The formal description of the infinite structure is then

$$\mathbf{X}_{i,\zeta} = \zeta\mathbf{T} + \mathbf{R}^{\zeta}\mathbf{X}_{i,0} \tag{3.1}$$

$$\mathbf{T} \equiv \begin{bmatrix} 0 \\ 0 \\ T \end{bmatrix}$$

$$\mathbf{R} \equiv \begin{bmatrix} \cos\gamma & -\sin\gamma & 0 \\ \sin\gamma & \cos\gamma & 0 \\ 0 & 0 & 1 \end{bmatrix}.$$

The unit cell (atoms possessing coordinates $\mathbf{X}_{i,0}$) is highlighted in maroon in Fig. 3.1 (d) and (e) for the 8-layer nanowire. As mentioned, the use of objective boundary conditions meant that the unit cells contained no more than 276 atoms. This meant that the objective simulations carried out here, coupled with DFTB [46] were not computationally intensive. Thus, it was possible to run many simulations with varying geometric parameters in order to optimize them. Each simulation consisted of a conjugate-gradient structural relaxation of the atomic coordinates. Again, these computations would not be possible with PBC for various reasons. The twist angle γ cannot take arbitrary values with PBC, and for the discrete values that are allowed, the simulaton cells would have to be much larger than the small helical cells used here.

An example optimization of the twist angle γ is shown in Fig. 3.1(c). The screw dislocated NW exhibits a minimum at γ_E =14.0 deg, corresponding to a twist rate of γ_E^* =3.64 deg/Å. The value of T (length of the simulation cell) was kept to 3.84 Å for all NWs, as no significant variation in T was found due to the introduction of the dislocations and variation of the Burger's vector and nanowire size. By assuming a circular cross-section as mentioned, these simulations were also used to find the effective shear modulus $G = 0.38$ eV/Å^3 in excellent agreement with the shear modulus appropriate for $\langle 110 \rangle$ screw dislocations in Si calculated from the anisotropic elastic constants [76].

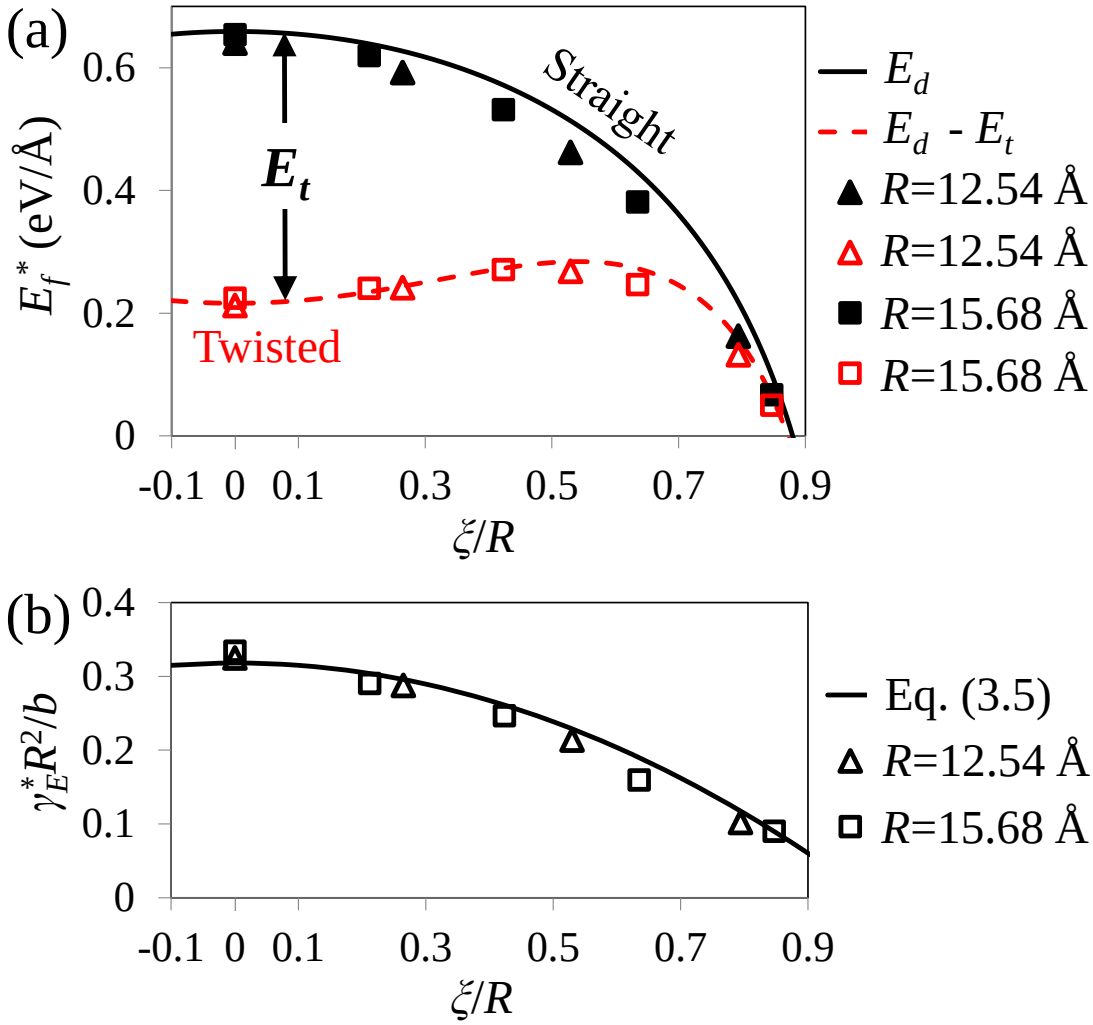

Figure 3.2: (a) Formation energy of off-center dislocations. Lines represent Eq. 3.4 (red, dashed) and Eq. 3.2 (black, solid). Symbols represent simulation results. Data is shifted by $-\frac{Gb^2}{4\pi}\ln(R/r_0)$ to remove radius dependence. The difference between the two curves is E_t of Eq. 3.3. (b) Intrinsic twist rate of NWs with off-center dislocations, divided by b/R^2 to non-dimensionalize and remove radius dependence. Symbols represent simulation results, line represents Eq. 3.5.

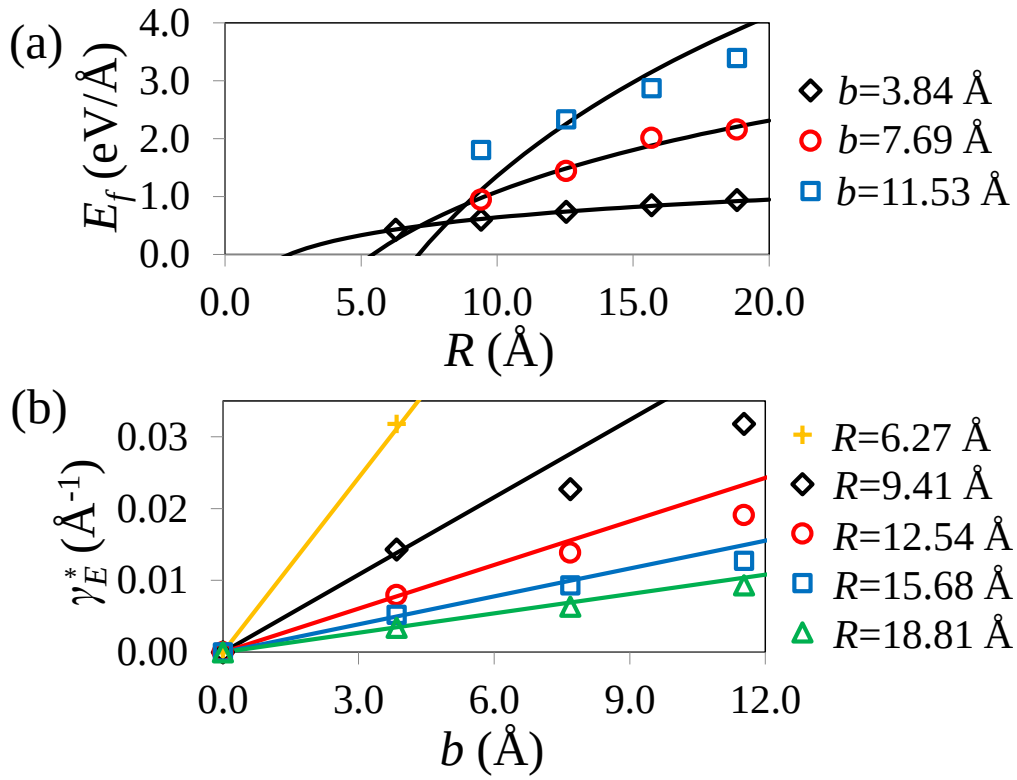

Figure 3.3: (a) Formation energy per length of NWs with ξ =0 for each value of b, as a function of radius. Fitted with Eq. 3.4, E_c = 0.659, 2.39 and 5.91 eV/Å for b = 3.84, 7.69 and 11.53 Å, respectively. Symbols are simulation data, lines are fitting. Note the poor fit for b = 11.53 Å. (b) Eshelby twist per length of the NWs as a function of magnitude of Burger's vector for different radii. Symbols are the results of simulations, lines show twist predicted by Eq. 3.4.

3.3 Simulation Results and Comparison with Continuum Theory

A detailed description of the elastic theory and its agreement with the simulation results is now presented. Eshelby presented the formation energy per length a screw dislocation in a linear elastic isotropic rod [74]. For a rod free of twist, Figure 3.1(a), the energy reads:

$$E_d = E_c + \frac{Gb^2}{4\pi}\ln\left(1-(\xi/R)^2\right) + \frac{Gb^2}{4\pi}\ln\frac{R}{r_0}. \tag{3.2}$$

Here, $G = 0.38$ eV/Å^3 is the shear modulus calculated from torsion optimization as described earlier. As discussed, the first term, E_c is an empirical energy of the material inside the core radius r_0, which cannot be modeled using elasticity. The second and third terms describe the linear elastic energy of the annular region between r_0 and the NW surface radius R. E_c and r_0 depend on b. The Eshelby twist, Figure 3.1(b), reduces the formation energy per length by E_t,

$$E_t = \frac{Gb^2}{(4\pi)}\left[1-(\xi/R)^2\right]^2. \tag{3.3}$$

In summary, the formation energy, compared to a pristine NW, of a dislocated NW allowed to freely twist, is

$$E_f = E_d - E_t. \tag{3.4}$$

The magnitude of the Eshelby twist per length γ_E^* satisfies a non-dimensional relation

$$\gamma_E^* R^2/b = \pi\left[1-(\xi/R)^2\right]. \tag{3.5}$$

In Fig. 3.2(b), the validity of Eq. 3.5 is tested against the microscopic data. The optimized twist is superimposed for the two NWs with varying ξ, scaled in the same way. The excellent agreement is the first piece of evidence suggesting that Eshelby's elastic model works well for these NWs. Next, it is desirable to see if the energetics seen in Fig. 3.2(a) can be predicted by Eq. 3.2 and Eq. 3.4. Since it is not feasible to deconvolute the value of r_0 and the value of E_c, $r_0 \equiv b$ is assumed [76]. All the other quantities are known, so E_c is the sole fitting parameter.

To identify E_c, a wide variety of NWs with dislocations located at the center ($\xi = 0$) was simulated. The data and fitting are shown in Fig. 3.3(a). The NWs had their

twist optimized for minimum energy, and Eq. 3.4 was fitted to the data. Although the data being verified (Fig. 3.2) has $b = 3.84$ Å, NWs with bigger b were also investigated, while keeping $\xi = 0$. The smallest NW, $R = 6.27$ Å, was unable to support dislocations with $b > 3.84$ Å, instead drastically rearranging a $\{110\}$ family plane containing the dislocation axis, so these data points are not included. This justifies the use of Arias and Joannopoulos' $r_0 \equiv b$ [76], as the core region cannot be bigger than the NW itself. When $b = 3.84$ and 7.69 Å, Eq. 3.4 models the formation energy well, with $E_c = 0.659$ and 2.39 eV/Å, respectively. However, for $b = 11.53$ Å, the elastic theory fails to model the energetics. For this value of b, the assumed size of core region exceeds the $R = 9.41$ Å NW as well. In Fig. 3.3(b) the twist predicted by Eq. 3.5 is compared to the twist obtained from the microscopic data at ξ =0. A similar trend emerges as the one seen in the energy comparison. For $b = 3.84$ Å, Eq. 3.4 very closely predicts the simulated twist for all radii. For 7.69 and 11.53 Å, however, the simulated twist drops off from the predicted value. This is likely due to the size increase of the core region of the dislocation.

Now that E_c has been calculated, one can return to the question of whether the stability of the dislocation at the central location shown in Fig. 3.2(a) can be described with Eshelby's Eq. 3.4. To collapse the data and equations onto one plot as a function of ξ/R, the size-dependent term $\frac{Gb^2}{4\pi}\ln(R/r_0)$ is subtracted from E_f. The adjusted energies, termed E_f^*, with no twist should collapse onto one curve, and with twist onto another. As shown in Fig. 3.2(a), there is excellent agreement between the simulated energies and the energies predicted by Eq. 3.2 and Eq. 3.4. This is despite the fact that only the $\xi = 0$ points for *twisted* NW were used to fit E_c. Note again the interesting features of the energetics of dislocation movement. The difference between the two curves is entirely due to Eshelby twist. For twisted wires, the central ($\xi = 0$) dislocations are a local minimum, while for straight wires they are a maximum. As the dislocation moves closer to the surface of the wire, the amount of twist decreases, and the two curves converge.

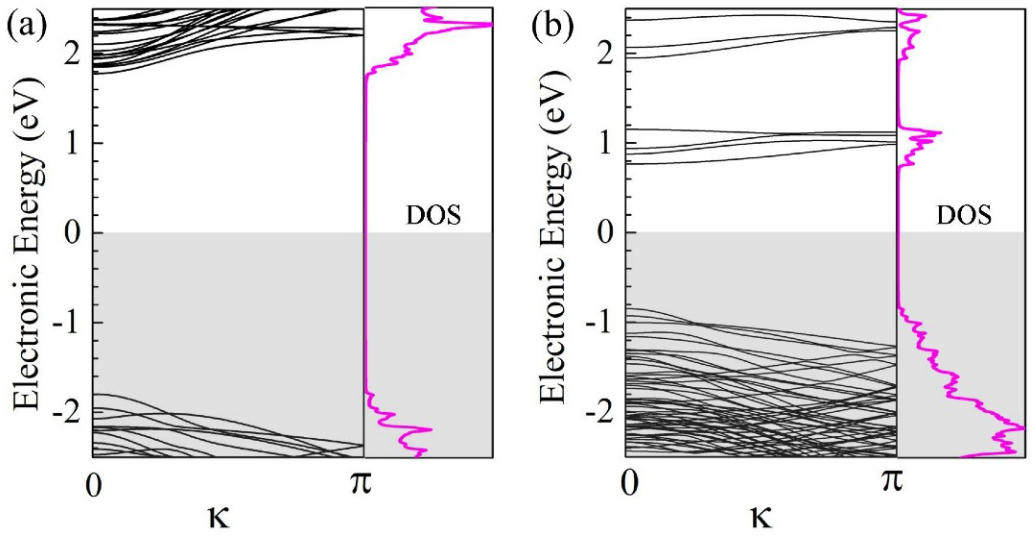

Figure 3.4: Band structure and density of states for NW with $R = 9.41$ Å, (a) pristine and (b) dislocated with $b = 3.84$ Å. The Fermi level was set to zero.

3.4 Electronic Properties

Modulating the electronic structure of Si NWs is of great practical importance. Currently, three methods are investigated: change in quantum confinement by diameter variations, doping with impurities, and surface doping[87]. Band structure and density of states calculations presented combined with the already demonstrated structural stability suggest the involvement of a screw dislocation could provide a fourth way. Indeed, the change in symmetry introduced by the screw dislocation couples effectively to the electronic states around the Fermi level, an effect observed before in Si quantum dots [88]. For example, for the $R = 6.27$ Å NW, the dislocation with $b = 3.84$ Å reduces the bandgap from 3.9 eV to 2.0 eV. For the $R = 9.41$ Å, the reduction is from 3.6 eV to 1.6 eV, Fig. 3.4.

3.5 Conclusion

In conclusion, the recent theoretical innovations of objective molecular dynamics coupled with density functional-based tight-binding [46, 41], a detailed microscopic description

of an axial screw dislocation residing in $\langle 110 \rangle$ Si NWs with radii between 0.5 to 2 nm is provided. The stability of the dislocation can be understood even at larger radii when microscopic calculations are prohibitive, based on the analytical predictions of Eshelby supplemented with the microscopically determined E_c. The methodology presented herein offers a new way to compute the core energy of a dislocation and opens up the possibility for a cross-disciplinary (materials science – continuum mechanics) understanding of a class of nanomaterials [65, 66, 67, 68, 69, 70, 71], with new properties and diverse applications. The uncovered connection between symmetry and electronic states makes these structures very exciting for both fundamental and applied research. The symmetry change introduced by the screw dislocation appears to be a useful strategy for manipulating the electronic response in other NW materials.

Chapter 4

Applications of non-SCC objective DFTB: Bending of Graphene

4.1 Introduction

Bending of graphene [9] continues to attract great interest from both experiment [10, 11, 12] and theory [13, 14, 15, 16, 17, 18, 19]. The understanding of this fundamental deformation mode begins with the early *ab initio* and classical potential atomistic studies [21] of carbon nanotubes (CNTs), which are helical tubules of graphene [22, 23] with radii less than 1 nm. The obtained linear variations of the strain energy with the square of curvature suggested that continuum elastic theory persist well into the small-radius limit.

Continuum modeling of the one-atom thick CNT's wall has been further pursued [24].

In particular the association with a linear-elastic mechanical shell has stirred controversies [25] focused on what thickness should be associated to the atomically thin carbon layer [26, 27, 28, 15]. More recently, it has been recognized [29, 14, 16] that graphene's thickness cannot be defined in the continuum sense and that the linear variation of the bending modulus with the Young's modulus becomes invalid. Thus, the bending of graphene is different from the one expected for plates and shells. Nevertheless, the origin of the non-vanishing bending rigidity remained elusive.

The usual starting point [30, 15, 29, 14] for modeling graphene's bending rigidity is the classical potential description of the carbon-carbon covalent bonding. The classical potentials [31, 32, 33, 34] currently used to model graphene are not derived by solving approximately the electronic structure problem. Instead, they are constructed with functional forms combining molecular mechanics with the concept of bond-order, and containing parameters fitted to reproduce data accessible from experiment and/or *ab initio* atomistic simulations. The physical origin of the finite well-known bending rigidity is encrypted into the specific molecular mechanics picture. For example, Lu et al. [14] obtained that the second-generation Brenner potential [34] captures the bending energy by the effects of bond and dihedral angles [14].

It has been known for some time that the bonding in nonplanar conjugated organic molecules can be well understood with the three dimensional [35, 36] Hückel bond orbitals [37] constructed with the π-orbital axis vector (POAV) scheme [38, 39, 35]. The primary assumption consists in prioritizing the σ bonds by treating them as a "rigid" network. After the adjustment of the geometry to its optimal curved structure, the remaining effect of non-planarity is absorbed into the π system. This POAV analysis provided a useful basis to understand stability in fullerenes and carbon nanotubes.[1]

In this chapter the POAV treatment is used for nanomechanics, to reveal the origin of the finite bending rigidity of graphene directly from the quantum mechanical description of bonding. This result, presented in a brief version elsewhere [16], has implications for both continuum and classical potentials-based modeling of graphene. It provides explanations for the very high Young's moduli obtained by fitting a linear plate model

[1] The bond symmetry breaking due to curvature directly influences the electronic properties of CNTs. See for example C. T. White, J. W. Mintmire, R. C. Mowrey, D. W. Brenner, D. H. Robertson, J. A. Harrison, and B. I. Dunlap, in *Buckminster fullerenes*, edited by W. Edward Billups and Marco A. Ciufolini VCH, New York, 1993.

to the the atomistic simulations data, and for the spread in bending constant values obtained with the classical potential descriptions of graphene.

This chapter is organized as follows. In Section 4.2, the objective symmetry [40] of the cylindrically bent graphene is combined with three dimensional Hückel bond orbital theory to derive an analytical expression for the bending energy under an arbitrary direction. This expression parameterized by Harrison's parameters illustrates how the bending strain is reflected into the energy of the σ and π bonds. Section 4.3 this picture is confirmed using OMD simulations coupled with DFTB. Section 4.4 discusses the implications of these findings for modeling graphene bending. Three of the Appendices are relevant to this chapter. Appendix A gives the rigorous description of the objective atomic structure of bent graphene. To facilitate the discussion in Sections 4.3 and 4.4, Appendix B gives the analytical expressions for bond lengths, bond angles, and dihedral angles of bent graphene. Appendix C contains an analysis of the small deviations from ideal bending that occur due to lattice and elastic effects.

4.2 Hückel molecular orbital theory of Bent Graphene

4.2.1 Structure of bent graphene

The whole structure of bent graphene can be constructed by applying the symmetry operations to only one atom. In the situation when bent graphene represents a CNT, these symmetry operations are given by the discrete group of isometries presented in Appendix A. As described next, in the case of an arbitrary curvature and direction of bending, one atom also can be used to generate a finite size domain of bent graphene structure. This description is not directly related to the objective boundary conditions used elsewhere in this dissertation, but is a local description of the environment surrounding an atom.

Graphene's lattice is a bi-lattice composed of two identical lattices each described by the Bravais basis vectors $\mathbf{t}_1$ and $\mathbf{t}_2$. Fig. 4.1 a) shows a unit cell containing two equivalent carbon atoms. Each atom from one lattice bonds with three nearest-neighbor atoms located on the other simple lattice. The direction of bending is characterized with the help of vector $\mathbf{C}$. In the two-dimensional geometry (before bending), the angles made by $\mathbf{C}$ with the three bonds ($i = 1, 2, 3$) are labeled by β_i . Also, $\beta \equiv \min(\beta_i)$. Then,

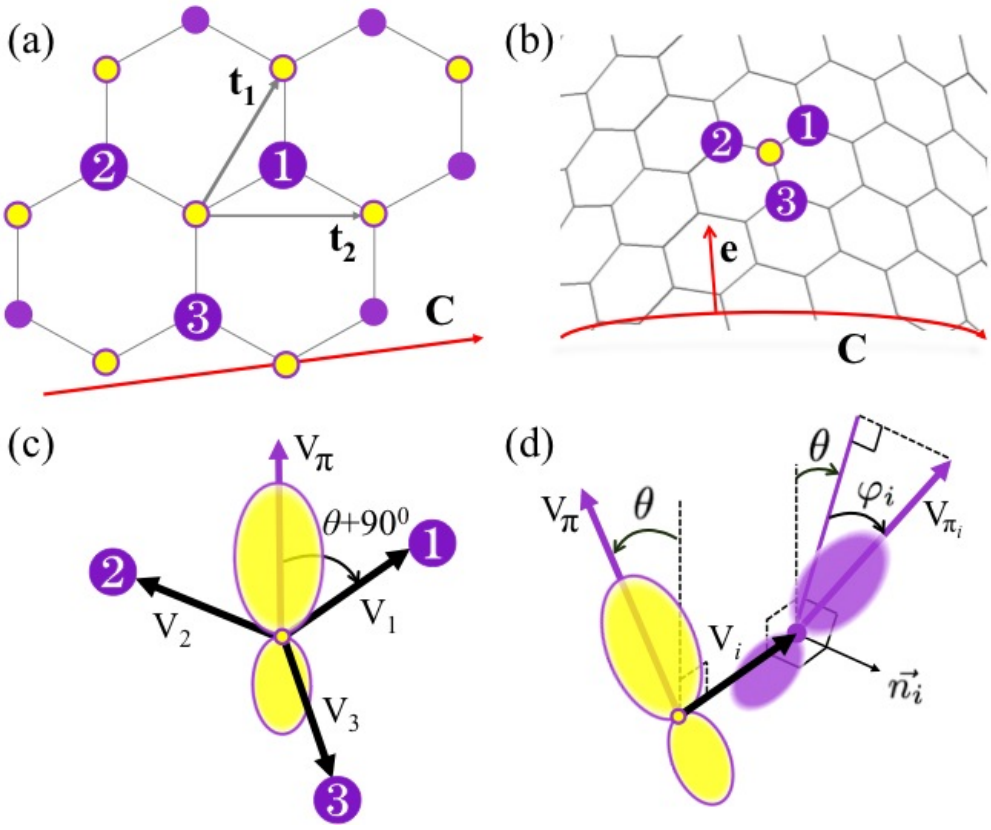

Figure 4.1: (a) Illustration of graphene honeycomb bi-lattice, where $\mathbf{t}_1$ and $\mathbf{t}_2$ are the Bravais basis vectors. (b) Bent graphene along the $\mathbf{C}$ direction. (c) POAV1 construction of π-orbital axis vector $\mathbf{V}_\pi$, where $\mathbf{V}_1$, $\mathbf{V}_2$ and $\mathbf{V}_3$ are the unit vectors lying along the internuclear directions to first-neighboring atoms. (d) Schematics of two adjacent π-orbital axis vectors showing the in-plane θ and torsional (out-of-plane) φ_i misalignment angles.

$\beta_i = \beta + 2\pi(i-1)/3$.

Under a pure bending deformation, Fig. 4.1 b), these bonds become distinct in terms of lengths and angles between them. However, to the first order in curvature the three bonds have identical lengths and the angles between them are 120°, see Appendix B. Moreover, the two carbon atoms continue to be equivalent as they see the same environment. Each atom and its 3 nearest neighbors are now located in the corners of a isosceles pyramid rather than in one plane. Thus, the microscopic bi-lattice structure is constructed with successive symmetry operations applied to one primary carbon atom. As described in Ref. [41], the atoms within the same sub-lattice are related by repeated applications of two independent helical operations delineated by the $\mathbf{t}_1$ and $\mathbf{t}_2$ vectors. The nearest-neighbor atoms belonging to the different sub-lattices will be obtained with 180° rotation operations around a radial axis that passes through the center of the bond [42]. This symmetry operation preserves objectivity and replaces the established method of relating the sub-lattices by an isolated helical operation [43]. The preservation of objectivity allows every atom in the entire structure to be treated identically, simplifying the subsequent electronic orbital energy analysis.

The morphology of the purely bent graphene (free of in-plane strains) of finite curvature $1/R$ represents an exact isometric mapping of the graphene sheet onto a nanotube of radius R. Let

$$\mathbf{X} = \{\mathbf{R}, \mathbf{0}, -(\mathbf{a/2})\sin\beta_{\mathbf{1}}\}. \tag{4.1}$$

be the position of one primary atom, where a is the carbon-carbon equilibrium bond length. For each atom i, the values of the azimuthal angles α_i write $\alpha_i = (a/R)\cos\beta_i$, $i = 1, 2, 3$. Atom 1 is obtained from atom located at $\mathbf{X}$ by a 180° rotation about the axis $\mathbf{e}_1 = \{\cos(\alpha_1/2), \sin(\alpha_1/2), 0\}$, or equivalently, by applying the matrix

$$\mathbf{R}_f = \begin{pmatrix} \cos\alpha_1 & \sin\alpha_1 & 0 \\ \sin\alpha_1 & -\cos\alpha_1 & 0 \\ 0 & 0 & -1 \end{pmatrix}. \tag{4.2}$$

Atoms $i = 2$ and 3 are found by rotating atom 1 by $(\alpha_i - \alpha_1)$ around the axis $\mathbf{e} = \{0, 0, 1\}$ with

$$\mathbf{R}_{(\alpha_i-\alpha_1)} = \begin{pmatrix} \cos(\alpha_i-\alpha_1) & -\sin(\alpha_i-\alpha_1) & 0 \\ \sin(\alpha_i-\alpha_1) & \cos(\alpha_i-\alpha_1) & 0 \\ 0 & 0 & 1 \end{pmatrix}, \tag{4.3}$$

and then translating along **e** with

$$\tau_i = a(\sin\beta_i - \sin\beta_1). \tag{4.4}$$

The result is

$$\begin{aligned}
\mathbf{X}_1 &= \mathbf{R}_f\mathbf{X}, \\
\mathbf{X}_2 &= \mathbf{R}_{(\alpha_2-\alpha_1)}\mathbf{R}_f\mathbf{X} + \{0, 0, a(\sin\beta_2 - \sin\beta_1)\}, \\
\mathbf{X}_3 &= \mathbf{R}_{(\alpha_3-\alpha_1)}\mathbf{R}_f\mathbf{X} + \{0, 0, a(\sin\beta_3 - \sin\beta_1)\}.
\end{aligned} \tag{4.5}$$

4.2.2 The π-orbital axis vector (POAV) analysis

To gain a clear physical picture of bonding in bent graphene, the classical Hückel molecular orbital (HMO) theory is used [44, 37]. Each carbon atom contributes to bonding with four electrons. In the planar case, three electrons are promoted to orthogonal sp^2 hybrid orbitals constructed to follow the symmetry of the lattice. The fourth electron is in an atomic-like p orbital positioned perpendicularly on the graphene sheet. In order to calculate the amount of rehybridization in bent graphene, π-orbital axis vector analysis (POAV) is employed [38, 39, 35]. With the σ-bonds forced to lie along the internuclear axes, orbital orthogonality is used to solve for the π-orbital hybridization and direction. The hybrid orbitals are

$$|h_{\sigma_i}\rangle = \frac{1}{\sqrt{1+\lambda_i^2}}(|s\rangle + \lambda_i|p_i\rangle), \qquad \lambda_i^2 = \frac{1}{\lambda^2\sin^2\theta}, \qquad n = \lambda_i^2, \tag{4.6}$$

$$|h_{\pi}\rangle = \frac{1}{\sqrt{1+\lambda^2}}(|s\rangle + \lambda|p_z\rangle), \qquad \lambda^2 = \frac{1-3\sin^2\theta}{2\sin^2\theta}, \qquad m = 1/\lambda^2, \tag{4.7}$$

where the atomic $|p_i\rangle$ orbitals directed along the three internuclear axes and

$$\theta = \frac{a}{4R} \tag{4.8}$$

is the pyramidalization angle [36]. $|h_{\sigma_i}\rangle$ constructed this way are the bonding orbitals directed along the three internuclear axes to the adjacent atom described by vectors $\mathbf{V}_i$ of Fig. 4.1 c). If one imagines starting with the sp^2 hybrids of graphene, the hybridization changes to sp^n.

The direction of $|h_\pi\rangle$, $\mathbf{V}_\pi$, is conveniently determined with the POAV1 [38] construction as

$$\mathbf{V}_\pi = (\mathbf{V}_2 - \mathbf{V}_1) \times (\mathbf{V}_3 - \mathbf{V}_1)/|(\mathbf{V}_2 - \mathbf{V}_1) \times (\mathbf{V}_3 - \mathbf{V}_1)|. \tag{4.9}$$

The direction of the pure $|p_z\rangle$ atomic orbital is $\mathbf{V}_\pi$. If one imagines starting with the pure $|p_z\rangle$ atomic orbital as it is present in graphite, when it becomes $|h_\pi\rangle$, the hybridization changes to $s^m p$.

The goal is to apply this approach to bent graphene, where $\mathbf{V}_i = (\mathbf{X}_i - \mathbf{X})/|\mathbf{X}_i - \mathbf{X}|$. Substituting eqs. (4.1) and (4.5) into Eq. (4.9) and taking the Taylor series expansion with respect to θ results in

$$\mathbf{V}_\pi = \{1,\, \theta\cos 3\beta,\, \theta \sin 3\beta\} + O(\theta^3). \tag{4.10}$$

The objective symmetry makes it easy to identify the orientation of the $|h_\pi\rangle$ on all the other atoms. For the three neighboring atoms,

$$\begin{aligned} \mathbf{V}_\pi^1 &= \mathbf{R}_f \mathbf{V}_\pi, \\ \mathbf{V}_\pi^2 &= \mathbf{R}_{(\alpha_2-\alpha_1)} \mathbf{R}_f \mathbf{V}_\pi, \\ \mathbf{V}_\pi^3 &= \mathbf{R}_{(\alpha_3-\alpha_1)} \mathbf{R}_f \mathbf{V}_\pi. \end{aligned} \tag{4.11}$$

The key point is that the $\mathbf{V}_\pi^i \nparallel \mathbf{V}_\pi$, Fig. 4.1 d). In the plane of vectors $\mathbf{V}_\pi$ and $\mathbf{V}_i$, misalignment is quantified by the pyramidalization angle. Additionally, there is out-of-plane torsional misalignment measured by the angles φ_i made by $\mathbf{V}_\pi^i$ with the plane delineated by $\mathbf{V}_\pi$ and $\mathbf{V}_i$. The torsional misalignment angles are

$$\begin{aligned} \varphi_1 &= 4\theta \sin(2\beta) + O(\theta^3), \\ \varphi_2 &= -4\theta \sin(2\beta + \pi/3) + O(\theta^3), \\ \varphi_3 &= -4\theta \sin(2\beta - \pi/3) + O(\theta^3). \end{aligned} \tag{4.12}$$

The above Taylor series expressions, of course, implicitly contain the assumption of small θ. Indeed, here only the small-angle bending is of interest because of the focus on the low-curvature linear bending regime of graphene. Nevertheless, it is instructive to compare the above approach of truncating the Taylor expansion of POAV to the more precise POAV2 treatment [38]. POAV2 is a more complex treatment – it distinguishes

between different bonds unlike POAV, and requires numerical evaluations. However, previous work indicated that POAV gives close predictions to POAV2 for the pyramidalization angle [36]. Here, it is demonstrated that the torsional misalignment angles calculated by the above analytical approach (Eq. 4.12) are in good agreement with those calculated using POAV2 to surprisingly high angles. This is shown in Fig. 4.2 for (n, m) carbon nanotubes characterized by the chirality angle χ, where $\chi = \pi/6 - \beta$. Evidently, even for curvatures causing misalignment angles as high as $\phi \approx 30°$, the approximate analytical treatment gives satisfactory results.

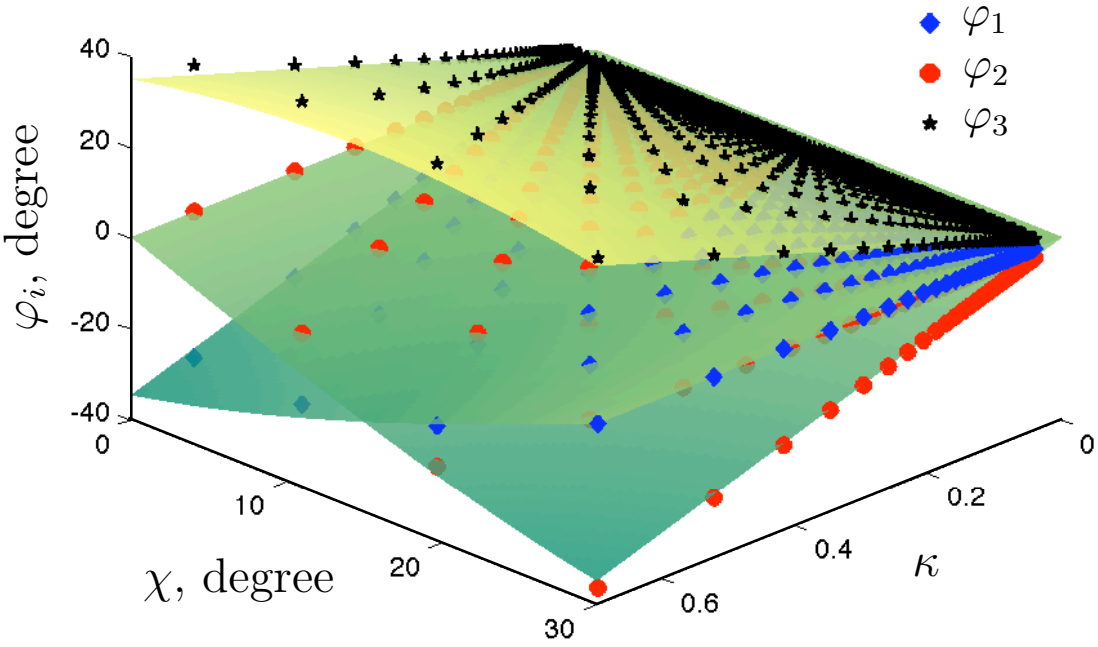

Figure 4.2: Torsional misalignment angles φ_i as functions of chirality angle χ and dimensionless curvature $\kappa = a/R$. Surfaces represent the analytical expressions given by (4.12), whereas the sets of points correspond to misalignment angles of obtained numerically with POAV2.

4.2.3 Strain in Bent Graphene

The change in energy of a graphene sheet with curvature in the HMO approximation is now examined. The total energy of the system is comprised of two parts – the valence

obital component and a repulsive radial potential. Because the interatomic distance does not change in the first-order approximation of the bent geometry, the repulsive radial potential remains constant and is not considered here. Thus, the bending strain energy of graphene is entirely contained in the valence orbital component. The construction of the $|h_\sigma\rangle$ and $|h_\pi\rangle$ hybrid orbitals (Eq. 4.6-4.7) block-diagonalizes the Hamiltonian of the system into blocks corresponding to each σ and π bond. σ bonds involve only the corresponding $|h_\sigma\rangle$ orbitals on two neighboring atoms, while the π bond involves the $|h_\pi\rangle$ orbitals on an atom and all three of its nearest neighbors. Thus, the hybrids centered on a single atom will participate in three identical 2×2 blocks due to each σ bond and one 4×4 block due to the π bond. The ground-state per-atom energy, then, will be the sum of the minimum eigenvalues of each of these blocks – E_σ for the sum of he energy due to the three σ bonds and E_π due to the π bond. These energy expressions will inevitably contain as a term the on-site energy of the corresponding hybrid – the energy of the hybrid if the atom was isolated. However, the sum of these energies over all of the hybrid orbitals is always constant – after all, the hybrid orbital construction is simply a rearrangement of the atomic orbitals for the mathematical convenience of block diagonalization. Thus, the on-site energy term is omitted from the expressions for E_σ and E_π.

The values used here for atomic orbital coupling are Harrison's universal matrix elements [37, p. 24]. They are independent of the chemical element being considered or any other parameter, except for an inverse square proportionality to the interatomic distance. Because the interatomic distance is constant (a =1.42Å) in the first-order analysis, the matrix elements are constant with the values $V_{ss\sigma} = -4.99\,\text{eV}$, $V_{sp\sigma} = 5.37\,\text{eV}$, $V_{pp\sigma} = 8.39\,\text{eV}$, and $V_{pp\pi} = -2.38\,\text{eV}$.

Consider first the σ bonding. The process outlined above results in

$$E_\sigma = \frac{1}{S_0}\sum_{i=1}^{3}\langle h^0_{\sigma_i}|H|h^i_{\sigma_i}\rangle = \frac{1}{S_0}\sum_{i=1}^{3}\left(\frac{1}{1+\lambda_i^2}V_{ss\sigma} - \frac{2\lambda_i}{1+\lambda_i^2}V_{sp\sigma} - \frac{\lambda_i^2}{1+\lambda_i^2}V_{pp\sigma}\right) = \frac{1}{S_0}(V_{ss\sigma} - 2\sqrt{2}V_{sp\sigma} - 2V_{pp\sigma}) + \frac{1}{S_0}(-2V_{ss\sigma} + \sqrt{2}V_{sp\sigma} - 2V_{pp\sigma})\theta^2. \quad (4.13)$$

where $S_0 = 3\sqrt{3}a^2/4$ is the area occupied by one atom. Using the above interatomic Hamiltonian matrix elements, the result is $E''_\sigma = 0.07$ eV, where double prime is the double derivative with curvature. As expected, the model shows that the σ bonding is

practically not affected by curvature.

Consider now the bonding of the h_π hybrids and on how misalignment affects this bonding. Consider the plane formed by $\mathbf{V}_\pi$ and $\mathbf{V}_i$. In order to evaluate the coupling matrix elements, the $|p\rangle$ atomic orbitals should be decomposed geometrically into components that are perpendicular ($|p_\pi\rangle$ and $|p_\perp\rangle$) and parallel ($|p_\sigma\rangle$) to the interatomic separation

$$\begin{aligned} |p_z^0\rangle &= \cos\theta|p_\pi^0\rangle - \sin\theta|p_\sigma^0\rangle, \\ |p_z^i\rangle &= \cos\varphi_i(\cos\theta|p_\pi^i\rangle + \sin\theta|p_\sigma^i\rangle) + \sin\varphi_i|p_\perp^i\rangle, \qquad i=1,2,3. \end{aligned} \tag{4.14}$$

Substituting (4.14) into the first equation in (4.7) and taking the product between the neighboring π-hybrids, the Hamiltonian matrix element can be found as

$$\begin{aligned} \langle h_\pi^0|H|h_\pi^i\rangle = \frac{1}{1+\lambda^2}\left(V_{ss\sigma} + 2\lambda V_{sp\sigma}\sin\theta\cos\varphi_i + \lambda^2 V_{pp\pi}\cos^2\theta\cos\varphi_i - \lambda^2 V_{pp\sigma}\sin^2\theta\cos\varphi_i\right) = \\ 2\theta^2 V_{ss\sigma} + 2\sqrt{2}\theta^2 V_{sp\sigma}\cos\varphi_i + (1-2\theta^2)(1-\theta^2)V_{pp\pi}\cos\varphi_i - (1-2\theta^2)\theta^2 V_{pp\sigma}\cos\varphi_i = \\ V_{pp\pi} + \left(2V_{ss\sigma} + 2\sqrt{2}V_{sp\sigma} - V_{pp\sigma} - 3V_{pp\pi}\right)\theta^2 - V_{pp\pi}\varphi_i^2/2. \end{aligned} \tag{4.15}$$

Diagonalizing the 4×4 block corresponding to the π bond results in a minimum eigenvalue

$$E_\pi = \sqrt{\sum_{i=1}^{3}\frac{\langle h_\pi^0|H|h_\pi^i\rangle^2}{S_0^2}} \tag{4.16}$$

The result is

$$E_\pi = \frac{\sqrt{3}}{S_0}V_{pp\pi} + \frac{\sqrt{3}}{S_0}\left(2V_{ss\sigma} + 2\sqrt{2}V_{sp\sigma} - V_{pp\sigma} - 3V_{pp\pi}\right)\theta^2 - \frac{\sqrt{3}}{6S_0}V_{pp\pi}\sum_{i=1}^{3}\varphi_i^2. \tag{4.17}$$

Making use of (4.12) torsional angles φ_i can be related to θ through $\sum_{i=1}^{3}\varphi_i^2 = 24\theta^2$. It follows that

$$E_\pi'' = \frac{1}{6}\left(2V_{ss\sigma} + 2\sqrt{2}V_{sp\sigma} - V_{pp\sigma} - 3V_{pp\pi}\right) - \frac{2}{3}V_{pp\pi}. \tag{4.18}$$

The main contribution of 1.6 eV comes the second term, which captures the π-orbital torsional misalignment. The first term of 0.63 eV, captures the pyramidalization. This simple analysis serves as a qualitative demonstration that the π-orbital torsional misalignment dominates the bending energy and that the obtained value for the bending

stiffness compares well with the one calculated with accurate atomistic simulations (Table 4.2). The authors of Ref. [35] postulate the same relationship between the bending strain energy contributions, based on their observation that the torsional angles in CNTs are much higher than the pyramidalization angles. They note that this is the reverse of the case of fullerenes, where the torsional misalignment is very small (or zero in the case of C_{60}), and the entirety of the strain energy may be approximated using only pyramidalization angles [39].

4.3 Density functional theory-based tight-binding (DFTB) theory of Bent Graphene

In order to support the above analytical predictions, objective molecular dynamics[41] simulations coupled with DFTB[45] were performed. CNTs of varying diameter were simulated, corresponding to ideal graphene sheets rolled into constant-curvature cylinders.

Similar to the examples regarding cell size in Secs. 2.2 and 2.3, simulations of CNTs using OMD can be carried out on various size simulation domains, which are delineated by knowing the specific symmetry of the CNT [41]. With an appropriate domain choice, OMD can simulate CNT plasticity and nonlinear elasticity [41, 47, 48]. Here this range of complex mechanical phenomena is not considered – only in the linear elasticity of ideal graphene is of interest. Therefore, the minimum simulation cell – just two atoms – is used(Fig. 4.3). It should be noted that in this case OMD reduces to the method of White et al. [43]. Because the two-atom domain is compatible with *any* CNT, large-diameter CNTs can be easily simulated and the small-θ approximation regime described in the preceding sections holds. As usual, carrying out these simulations with PBC would require much more atoms to be included in the simulation cell. Specifically, for an ideal (n,m) CNT, a number of atoms proportional to $(n^2+nm+m^2)/\mathrm{GCD}(2n+m, 2m+n)$ would have to be used, where GCD indicates the greatest common divisor. Thus, when using PBC, the number of atoms in the unit cell is chirality-dependent and proportional to the radius, meaning that very large unit cells are required to simulate large-diameter CNTs, especially if they are chiral. Because the study of graphene bending requires simulations of multiple large CNTs, previous studies that were restricted to PBC have

typically used classical interatomic potentials[29, 15]. Additionally, here the possibility of intrinsic twist is also investigated. This breaks the ideal symmetry, and means the structure cannot be investigated with PBC at all[50, 51, 52, 53] – the situation is similar to that described in Chapter 3, where only discrete values of twist rate are permitted under PBC.

Here, to simulate CNTs, DFTB is coupled with angular-helical objective boundary conditions – the most general case of OMD used in this dissertation. The infinite structure is described from the two-atom motif using the helical operation h and angular operation g:

$$\mathbf{X}_{i,\zeta_h,\zeta_g} = \zeta_h \mathbf{T} + \mathbf{R}_\gamma{}^{\zeta_h} \mathbf{R}_\psi{}^{\zeta_g} \mathbf{X}_{i,0,0}$$

$$\mathbf{T} \equiv \begin{bmatrix} 0 \\ 0 \\ T \end{bmatrix}$$

$$\mathbf{R}_\gamma \equiv \begin{bmatrix} \cos\gamma & -\sin\gamma & 0 \\ \sin\gamma & \cos\gamma & 0 \\ 0 & 0 & 1 \end{bmatrix}$$

$$\mathbf{R}_\psi \equiv \begin{bmatrix} \cos\psi & -\sin\psi & 0 \\ \sin\psi & \cos\psi & 0 \\ 0 & 0 & 1 \end{bmatrix}$$

Starting with a 2-atom unit cell, the derivation of the structural parameters comprising operations h (Fig. 4.3 b)) and g (Fig. 4.3 a)) – the length T and the angles γ and ψ – is non-trivial, and is described in detail in Appendix A. These operations, as well as the tube radius, are shown for a (40,20) CNT in Table 4.1 in the "Initial" row. In fact, the Appendix takes the objective description one step further, constructing the 2-atom unit cell from a 1-atom cell and additional objective operation – f, a 180° rotation around the center of a bond. Here, this operation is not explicitly considered, and the 2-atom simulation cell is used. The bond between the atoms in the simulation cell corresponds to bond $i = 1$ in Section 4.2.

The intent of this section is to demonstrate that CNTs do, in fact, behave as an ideal bent graphene sheet. While at small CNT diameters, the high curvatures may introduce

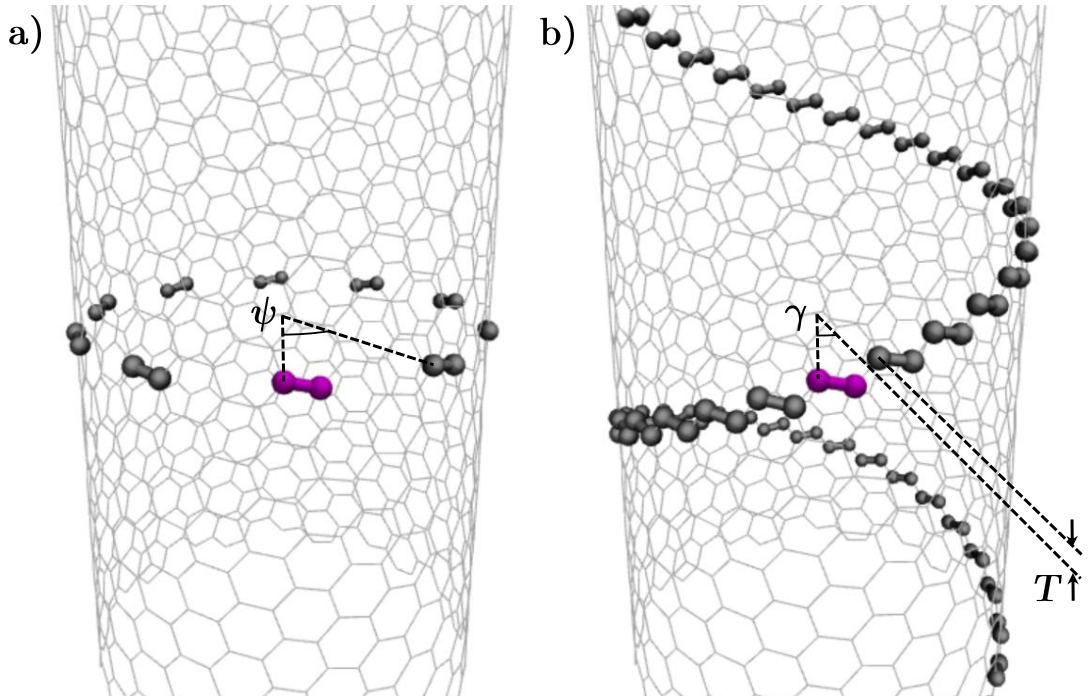

Figure 4.3: Symmetries used in the OMD simulations, for the case of a (20,10) CNT. a) Operation g – pure rotation around CNT axis of angle ψ. b) Operation h – rotation around CNT axis of angle γ combined with translation T along CNT axis.

Table 4.1: Symmetry operation parameters ψ, γ, and ρ, nanotube radius R, and bond strains ϵ_i(with respect to $a = 1.428$ Å) for a (40,20) CNT, as initially generated and (where different) in the fully relaxed configuration.

	ψ	γ	T(Å)	R(Å)	ϵ_1(%)	ϵ_2(%)	ϵ_3(%)
Initial	$\frac{\pi}{10}$	$\frac{\pi}{28}$	0.809	20.822	-0.0182	-0.0036	-0.0002
Relaxed				20.829	0.0046	0.0170	0.0020

non-ideal effects, larger CNTs are expected to match the structure described above, which corresponds to an ideal, unstrained graphene sheet rolled-up into a cylinder. To this end, conjugate-gradient relaxations of ($2m$,m) CNTs ranging from (20,10) to (40,20) were performed, starting with configurations generated as described. The ($2m$,m) family represents generic chiral CNTs, avoiding any idiosyncracies associated with armchair and zigzag tubes.

The conjugate-gradient relaxations were carried out until a tolerance of 10^{-8} Hartree was reached for the two-atom unit cell. The Brillouin zone in the helical direction was sampled with 500 or 1000 k-points, depending on the specific tube, in order to match the 10^{-8} Hartree tolerance. For a ($2m$,m) nanotube, the Brillouin zone in the rotational direction contains m discrete allowed values, all of which were calculated. The description of the carbon-carbon interactions was taken from the popular *pbc-0-3* parameter set designed to treat various solid-state systems[49]. The valence shell basis comprises the *sp* functions located on each carbon atom. In order to avoid errors arising from the parametrization, the geometry of the flat graphene sheet was first optimized using these parameters. The optimal bond length was found to be $a = 1.428$ Å. This is the value used for calculating the initial CNT geometry.

In these simulations, the CNTs expanded to radii slightly larger than that predicted by the ideal roll-up construction. Fig. 4.4 a) shows how small this expansion is – ranging from 0.13% for the (20,10) to a nearly negligible 0.042% for the (40,20). This confirms that large nanotubes do, in fact, behave as a nearly ideal rolled graphene sheet.

The (40,20) CNT is now examined in more detail. In the preceding simulations, the unit cell parameters – the translation T and rotation of angle γ making up operation h

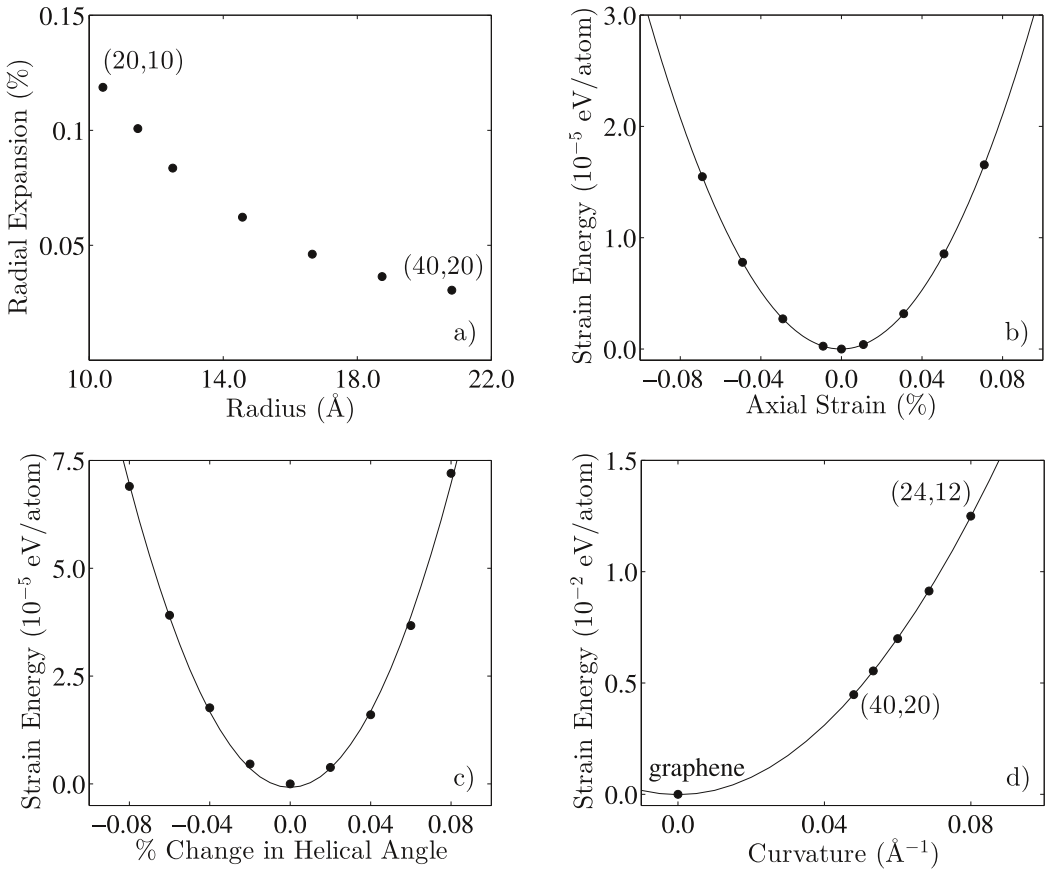

Figure 4.4: a) Radial expansion of CNTs during simulations w.r.t. the ideal roll-up construction, as a function of nanotube radius. b) Strain energy of (40,20) CNT as the translation T is varied compared to the value predicted by the ideal roll-up construction. c) Strain energy of (40,20) CNT as the angle γ is varied compared to the value predicted by the ideal roll-up construction. d) Bending strain energy of $(2m,m)$ CNTs with relation to flat graphene sheet as a function of curvature, with fitted quadratic curve.

– were kept constant at the values predicted by the ideal roll-up construction. They are now varied around the predicted values for the (40,20) CNT and a structural relaxation is performed at each point. The variation over γ would not be possible if PBC was used. The pure rotation angle ψ around the nanotube axis is rigorously determined by the nanotube indices, and therefore is not subject to optimization.

Fig. 4.4 b) shows the variation in energy as the translation T is varied around the value predicted by ideal roll-up construction. As the figure shows, there is no measurable axial pre-strain. The results shown in Fig. 4.4 b) were also used to calculate the in-plane Young's modulus C of graphene, resulting in a value of 24.7 eV/Å^2 (Table 4.2).

Analogously to the optimization of T, Fig. 4.4 c) shows the variation in energy as γ is varied around the ideal predicted value of $\pi/28$. There is no appreciable angular prestrain at all. This means that here there is no intrinsic twist (angular deviation from ideal roll-up prediction) phenomenon previously reported for small-diameter C, MoS_2, TiS_2, ZnO and BN nanotubes[50, 51, 52, 53].

Thus, it has been shown that the radial, axial and torsional deviations from the ideal roll-up construction are all nearly or fully negligible for the larger-diameter CNT structures, meaning that these nanotubes indeed very closely correspond to graphene under pure bending. The results of these simulations are now used to calculate the bending stiffness $E_b^{''}$ of the graphene monolayer. The data points with $> 0.1\%$ radial strain in Fig. 4.4 a) are discarded, as this indicates a significant deviation from ideal bent graphene. The prestrains in the remaining points do not noticeably affect the result. Fig. 4.4 d) shows the strain energy (w.r.t. flat graphene) as a function of curvature. Fitting the data yields $E_b^{''} = 1.49$ eV after dividing by the atomic area S_0.

The contribution of the torsional misalignment and the pyramidalization angles to the bending stiffness can be estimated by once again employing Eq. 4.18 from Section 4.2. Instead of using Harrison's parameters, the values from the integral table containing the tight-binding Hamiltonian matrix elements are used. The entries for the relevant orbital interactions ($V_{ss\sigma}$, $V_{sp\sigma}$, $V_{pp\sigma}$, and $V_{pp\pi}$) are taken at the equilibrium interatomic distance. The substitution results in an estimate of 2.2 eV bending stiffness due to torsional misalignment, and only 0.06 eV bending stiffness due to pyramidalization. These values to not add up to $E_b^{''} = 1.49$ eV because DFTB is non-orthogonal tight binding – the overlap matrix is not the identity. However, just as the analysis in

Section 4.2 using Harrison's parameters, these values provide a demonstration that torsional misalignment is the dominant cause of bending stiffness in monolayer graphene. In the case of DFTB, the dominance of the torsional component is even higher than with Harrison's parameters.

As small as the radius deviations from the roll-up prediction are, it is useful to understand their origins, which are explained here. For smaller nanotubes, these corrections are non-negligible and need to be taken into account. Here, these corrections are quantified for the nanotubes considered and it is shown that they are truly negligible. There are two mechanisms responsible for the radial expansion observed. The first of these is a geometric non-ideality in the roll-up construction. In the circumferential direction, the construction projects each carbon-carbon bond onto an arc. The actual bond in the CNT, however, is the chord of this arc – the shortest distance between the atoms. This means that the roll-up construction creates a nanotube with slightly compressed bonds. This effect will be more significant in bonds that are more circumferentially oriented, i.e. $\beta_i \approx 0$ or π. The resulting bond length a_i is calculated in Appendix B (Eq. B.1). The strains as compared to the undeformed length $a = 1.428$ Å are shown in Table 4.1 for the bonds in a (40,20) CNT, in the "Ideal" row.

If this bond distortion was the only effect present, the optimal configuration would be one where the sum of the squares of the bond strains was minimized. In this configuration, the bond strains would either all be zero, or have different signs. However, as seen in the "Relaxed" row of Table 4.1, the bonds all have positive strain in the optimal (after conjugate-gradient relaxation) configuration. Thus, there is some other effect causing the bonds to expand compared to their value in flat graphene, $a = 1.428$ Å.

This additional expansion can be explained by a simple linear-elastic effect. When an elastic layer is rolled into a cylinder, setting the circumference of the cylinder to the undeformed length of the roll-up vector creates a configuration that has zero in-plane strain energy – the total strain energy is comprised entirely of the bending strain energy. However, this is not the minimum *total* strain energy. The configuration that results in the minimum total strain energy will see the structure increase its radius by a small amount, taking on a finite in-plain strain energy in exchange for reducing the bending strain energy.

The expected radial expansion due to both of these mechanims is calculated in detail

in Appendix C for the CNTs considered herein. As Fig. C.1 b) shows, the combination of these mechanisms accounts for the entirety of the radial expansion observed in the OMD-DFTB simulations. A consideration of the total linear-elastic strain energy of the system in the Appendix (Eq. C.3) also represents an opportunity to quantify the effect that the deviations from pure bending have on the strain energy. Consider the (24,12) CNT – the smallest, and therefore least ideal tube used in the $E_b^{''}$ fitting. The total strain energy is 0.013 eV/atom. The geometry after the bond length correction but before the energy competition correction corresponds to pure bending – zero in-plane strain. The ideal roll-up construction has a smaller radius, increasing the in-plane strain energy by 7.5×10^{-6} eV/atom and the bending strain energy by 1.2×10^{-5} eV/atom, for a total strain energy increase of only 0.15%. The fully relaxed configuration has energy deviations of similar magnitude, but they are, of course, of opposite sign – the in-plane strain energy is increased by 4.7×10^{-6} eV/atom, while the bending strain energy is decreased by 9.5×10^{-6} eV/atom, for a total strain energy decrease of 0.04%. Thus, either the ideal roll-up construction or the fully relaxed configuration can be safely considered to be in a state of pure bending without any significant error. In theory, the radial expansion due to the strain competition effect would also cause slight axial compression due to the Poisson effect. However, this compression is so small – 0.006% in the case of the (24,12) – that it is not noticeable. This is why there is no visible pre-strain in Fig. 4.4 b) – for the (40,20) CNT in that figure, the compression is even smaller.

It is instructive to compare the OMD-DFTB results for the in-plane modulus C and the bending stiffness $E_b^{''}$ with those of Kudin et. al[54]. The authors carried out *ab initio* calculations of these constants (Table 4.2). The agreement between the $E_b^{''}$ values is remarkable – the *ab initio* value is 1.46 eV, only 0.03 eV different from the OMD-DFTB value, speaking to the strength of the pbc-0-3 parametrization. Unfortunately, the *ab initio* value of C is 21.5 eV/$\mathring{A}^2$, 10% lower than the OMD-DFTB value – overbinding is a known problem with DFTB.

4.4 Discussion

The preceding analysis indicates that the source of strain in the bent monolayer can be largely attributed to the torsional misalignment between neighboring POAVs. The σ orbitals, which are in turn responsible for the large in-plane stiffness of graphene, are practically not contributing to the bending strain energy. This has important implications on the application of the continuum mechanics model of plate to graphene. On one hand, the difficulty of finding a plate model for graphene is often tied to the limitation of a continuum cross-section assumption – after all, the thickness of a graphene sheet is a single atom, an object with no well-defined thickness. There is disagreement on what plate thickness should be used[26, 27, 28, 15]. On the other hand, the analysis in Sections 4.2 and 4.3, based the quantum chemistry of the bonds, highlights directly the inadequacy of the plate model for graphene: The bending stiffness of a plate arises from the compression and tension in the material away from the plate centerline. This mechanism is in no way analogous to the quantum-mechanical source of graphene bending stiffness.

Table 4.2: The second derivative of the bending energy density with curvature and in-plane stiffness of graphenene mono-layer from *ab initio*, DFTB [45], and the following classical potentials: Tersoff [32], Brenner [33, 34], and AIREBO [55]. The data were collected from Refs. [14, 54, 56, 57, 41, 29, 55, 58, 59]. The last two columns present the resulting plate model.

	$E_b^{''}$ (eV)	C (eV/Å^2)	Y (TPa)	h (Å)
ab initio	1.46	21.5	3.9	0.89
DFTB	1.49	24.7	4.7	0.84
Tersoff	1.11	25.1	5.7	0.71
Brenner (1990)	0.84	15.0	3.0	0.80
AIREBO	0.91	20.0	4.4	0.73
Brenner (2002)	1.41	15.4	2.4	1.00

It is still possible (at least for infinitesimal strains) to fit to the microscopically obtained bending and stiffness values of graphene by choosing appropriate thickness and

Young's modulus of a continuum plate. Only a very thin plate constructed of a very stiff material will have a low bending stiffness as in graphene. Depending on the underlying microscopic description, the procedure leads to a spread of very high Young's moduli and small thicknesses, none that match the 1 TPa Young's modulus and 3.35 Å thickness deduced from experiment (Table 4.2). The origin of this paradox [25] is, of course, the error in assuming that the plate mechanics is rigorous for graphene.

The molecular orbital analysis and DFTB simulations also have implications for describing graphene bending with classical interatomic potentials. While the molecular orbital analysis in Sec. 4.2 only includes the nearest neighbors of a given atom, this is due to the fact that the curvature of the sheet is constant and known. In a general deformation, it is necessary to consider second-nearest neighbors in order to calculate the torsional misalignment. Thus, an interatomic potential must include second-nearest neighbor interactions in order to produce an effect that is analogous to π-orbital torsional misalignment in the general case. Typically, the second-nearest-neighbor interaction takes the form of a dihedral-angle term, such as in the second-generation Brenner[34] potential. A direct connection between dihedral angles and torsional misalignment is made in Appendix B - under pure bending, six out of the twelve dihedral angles associated with a given carbon atom are equivalent to the torsional misalignment angles. Table 4.2 shows a comparison of the bending and Young's moduli of several interatomic potentials as well the results from Section 4.3 and *ab initio* values[54]. Clearly, the inclusion of the dihedral-angle term in the second-generation Brenner potential drastically improves the description of E_b'' compared to potentials that are nearest-neighbor-only (Brenner 1990[33] and Tersoff[31]). However, this improvement is dependent on the parametrization of the dihedral-angle term. In Brenner's second-generation potential, it is appropriately parametrized for graphene. The AIREBO[55] potential also includes a dihedral-angle term. However, its form (discussed later in this section) is not appropriate for graphene, leading to a bending modulus that is actually less accurate than the Tersoff potential.

While the bending moduli given by the nearest-neighbor-only potentials are low, they are finite and arguably – in the case of the Tersoff potential (for a detailed description, see Appendix E) – accurate enough for certain studies. For example, I successfully studied the rippling under bending of MWCNTs using the Tersoff potential[60]. Because

rippling under bending arises from an interplay of compressive and bending stresses, an accurate description of bending is important. A later experimental study showed good agreement with my results[61]. Chapter 6 of this dissertation presents a similar success – it is an experimental-computational collaboration studying the buckling of graphene and boron-nitride nanoribbons. Once again, the buckling of graphene from an interplay of compressive and bending stresses, so it is a good test for the accuracy of the bending. And, once again, the experiments contained therein are in good agreement with the simulation predictions. Thus, the Tersoff potential provides satisfactory bending properties while being highly computationally efficient – the description of the potential specifically states that dihedral-angle forces are purposefully omitted in order to avoid extra computational cost[32]. What then, is the source of bending stiffness in nearest-neighbor-only potentials, if they are unable to reproduce an effect analogous to torsional misalignment, which has been shown to be primary source of bending energy in graphene?

The answer is the term dependent on the bond angles θ_{ij}. The exact way this term enters the Tersoff potential can be seen in Section E.1. Appendix B shows that these angles have a quadratic dependence on the pyramidalization angle θ, and thus on the curvature of the graphene sheet. The dependence of the energy on the bond angles in these potentials is non-zero in the first order[15], thus giving a finite second-order dependence on the curvature of the graphene sheet. This is the bending stiffness. Even though the bending stiffness arising from the bond-angle term does not correspond to the physical picture, it is, in theory, possible to fit this stiffness to any desired accuracy. However, interatomic potentials aim to describe much more than constant-curvature bending of a single allotrope of carbon. At the minimum, the potential must describe properties of several allotropes of a given element, both near equilibrium and when containing defects or under deformation. Potentials with broader intended applications additionally aim to describe properties of compounds, phase transitions, and chemical reactions. Thus, with only a limited number of fitting parameters, potentials must compromise between different properties. For example, in the Tersoff potential, the bond-angle term is the *only* multi-body term. In concept, its primary purpose is to describe coordination. Instead of looking at the entire environment of a given atom, the potential sums over three-atom terms which are weakened by deviation from the bond

angles preferred by the system being studied (carbon in this case), thus simulating an atom's tendency for specific coordinations. In reality, the bond-angle term also affects or determines a number of other simulated properties, including elastic constants. As such, the errors in the elastic properties of graphene in the Tersoff potential are no surprise – using only a single multi-body term, a perfect fit of elastic properties of every allotrope is simply not possible while maintaining acceptable accuracy in other properties of interest. The first-generation Brenner potential adds special coordination terms which simply count the number of bonds a given atom has, to gain additional parameter fitting freedom. However, the aim of the Brenner potential is different and more complex than the Tersoff potential – Brenner's goal was a description of reactions in hydrocarbons. Because of this, even with the additional terms, the description of elastic properties of graphene is worse in the first-generation Brenner potential.

The simple lack of parameters is not the only problem with nearest-neighbor-only potentials. The use of a bond-angle term as the sole multi-body term has some additional peculiar drawbacks. These observations also apply to Brenner's first-generation potential – the aformenentioned coordination terms remain constant under deformation, and only affect bond breaking and formation. One drawback is that, at infinitesimal strain, a potential that includes only bond-angle and interatomic distance terms has torsional and antibiaxial bending stiffnesses that are identically zero[15]. This is an unrealistic result – previous studies have shown that π-orbital misalignment creates a finite torsional stiffness at infinitesimal strain [62]. The inclusion of dihedral-angle terms naturally fixes this problem, as any torsion will involve rotation around bonds, changing the dihedral angles. In fact, the names of "torsional" and "dihedral-angle" terms are often used interchangeably in potential descriptions[55]. Note that at higher strains, torsional strain energy in graphene is dominated by tension and compression [63], so it is still possible to reproduce acceptable results with nearest-neighbor-only potentials in this case. Antibiaxial bending transforms into pure torsion under a 45° rotation of the differential stress element of the plate, similar to the stress transformation from antibiaxial normal strain to pure shear. Thus, the preceding discussion of torsion is equally applicable to antibiaxial bending.

Another drawback of nearest-neighbor potentials is evident in the ratios between bending and in-plane stiffnesses seen in Table 4.2. In both the Tersoff and Brenner's

first-generation potentials, the bending stiffness is low in comparison to the in-plane stiffness. The reason for this stems from the dependence of multiple properties on the bond-angle term. The dependence of bending on the bond-angle term has already been discussed. Thus, in order to make graphene stiff under bending, the bond-angle term must be made stronger. However, the bond angles also change when uniaxial tension is applied to a graphene sheet, meaning that a strong bond-angle term increases the Young's modulus. So, as can be seen in the Tersoff potential, making the bond-angle dependence strong enough to provide a reasonable bending stiffness causes the in-plane stiffness to be overestimated. The addition of a dihedral term alleviates this problem because it allows the bending stiffness to be tuned independently of the in-plane stiffness, as dihedral angles are not affected by in-plane deformations.

The attributes of second-nearest-neighbor potentials are now examined, starting with a comparison of the form of the dihedral-angle term in the second-generation Brenner potential and the AIREBO potential. The details differ, but in both potentials, assuming no bond-breaking or formation, there is an independent energy component that is proportional to the dihedral-angle term summed over all dihedral angles associated with a bond. See Appendix B for detailed definitions and computations of the dihedral angles Θ_{ijk}. In the second-generation Brenner potential, the dihedral-angle term is

$$V_{DH} \propto 1 - \cos^2(\Theta_{ijk}). \tag{4.19}$$

This form has minima at $\Theta_{ijk} = 0$ and $\Theta_{ijk} = \pi$, which are the two values the dihedral angles take in planar graphene. Thus, it allows for an effective fitting of the bending behavior of graphene. In the AIREBO potential, the term takes the form

$$V_{DH} \propto \cos^{10}\left(\frac{\Theta_{ijk}}{2}\right). \tag{4.20}$$

This form, on the other hand, has a minimum at $\Theta_{ijk} = \pi$, but a maximum at $\Theta_{ijk} = 0$. AIREBO is an earlier potential, and this form is inspired by molecular mechanics methods [64]. In individual molecules, the $\Theta_{ijk} = 0$ configuration is unfavorable, leading to this form that is not ideal for graphene due to having a maximum at one of the equilibrium values. Additionally, the authors of AIREBO note that sum over all angles has the correct form for sp^3 hybridized carbon. This difference in the dihedral-angle terms explains the difference in the accuracy of the two potentials when modeling graphene

bending. This, of course, highlights an inherent issue with empirical interatomic potentials – they are most useful only in situations fitted and anticipated by the creators. On the other hand, tight-binding is more transferrable due to its explicit treatment of the atomic orbitals, being able to accurately describe both sp^2 and sp^3 bonding.

The second-generation Brenner potential is now considered in more detail. This potential still contains a bond-angle term just like nearest-neighbor potentials, but adds the aforementioned dihedral-angle term as well. Both terms will change under bending and both will contribute to the bending stiffness of graphene. Although the inclusion of the dihedral-angle term means the machinery of this potential is less phenomenological and closer to the molecular orbital picture, ultimately the dihedral-angle term is not a pure representation of the torsional misalignment of π-orbitals. It is a term that allows extra freedom in the fitting of deformation energies of molecules and solids by considering second-nearest neighbors. For example, the bending stiffness is split approximately 50/50 between the dihedral-angle term and the bond-angle term[29]. If the dihedral-angle term was directly analogous to torsional orbital misalignment, this would run contrary to molecular orbital theory predictions that the torsional misalignment energy dominates graphene bending, found herein in Sections 4.2 and 4.3 and in Ref. [35]. Because the dihedral term is just another piece of the overall parameter fitting, even with the extra freedom, the second-generation Brenner potential doesn't have perfectly fitted elastic properties (Table 4.2). Just like the first-generation Brenner's potential, although to a much smaller extent, it must sacrifice some accuracy in the elastic properties of graphene in order to better fit its intended purpose – a general description of reactions in hydrocarbons.

An examination of Ref. [29] and comparison with the OMD-DFTB simulations provides additional insight into the behavior of the second-generation Brenner potential. Using this potential, the authors carry out a calculation of the bending stiffness E_b'' of graphene equivalent to the OMD-DFTB simulations carried out in Section 4.3. However, the authors deemed it necessary to the constrain the radius of the CNTs to avoid radial expansion to obtain an accurate E_b''. In contrast, in the simulations in Section 4.3, the radial expansion observed in the larger tubes was too small to significantly affect E_b''. Undoubtedly, this is partially due to the smaller sizes considered in Ref. [29] – while most of the tubes therein were just as large or larger than those used to calculate E_b'' in

Sec. 4.3 ($R > 10$ Å), the authors included tubes as small as (10,0) with $R = 2.5$ Å in their fitting. However, a closer look at the (10,0) CNT suggests that there is also a spurious expansion that arises from the Brenner parametrization. Ref. [29] contains the results of a radial optimization for a (10,0) CNT, without axial optimization. The authors observe a radial expansion of 1.3%. However, their analysis of the competition between the in-plane and bending strain energies, analogous to the analysis in Appendix C and carried out with the appropriate elastic constants obtained from the Brenner potential, predicts a radial expansion of only 0.5%. It is unclear if the authors compensated for geometric non-ideality of the roll-up construction. The subsequent analysis makes the conservative assumption that they did not. Using the procedure outlined in Appendix C, the geometric non-ideality would contribute approximately 0.4% to the radial expansion, for a total predicted radial expansion of 0.9%. Thus, in the simulation using the Brenner potential, there is at least 0.4% of additional radial expansion unaccounted for. For comparison, consideer an analogous OMD-DFTB relaxation on the (10,0) CNT, carried out using the same procedure as in Sec. 4.3. The result is a radial expansion of 0.9%. The energy competition correction predicted by the procedure outlined in Appendix C, used with the appropriate elastic constants for the DFTB parameters used (Table 4.2) predicts an correction of 0.4%, which, in combination with the 0.4% expansion due to the geometry correction, would account for nearly the entirety of the radial expansion observed, although the extra 0.1% that is unaccounted for demonstrates the deviation from linear-elastic behavior at high curvatures. Thus, Brenner's second generation potential causes excessive bend-stretch coupling that is not supported by DFTB simulations. This coupling may be the result of an overly strong bond-angle term.

4.5 Conclusion

Using analytical POAV analysis combined with Hückel bond orbital theory, it is demonstrated that the primary source of the bending stiffness of graphene is the torsional misalignment of the π hybrid orbitals. Using density functional-based tight-binding, atomistic simulations were carried out on a number of large-diameter CNTs. These capture the behavior of graphene in the low-curvature linear elastic regime, not achieved previously by investigations of small-diameter SWCNTs. These simulations were enabled

by objective molecular dynamics, which permitted CNTs of arbitrary diameter to be simulated with only two atoms. The simulations demonstrated that large CNTs very closely represent graphene under pure bending. A bending stiffness of 1.49 eV/Å^2 was obtained, remarkably close to the *ab initio* value of 1.46 eV/Å^2.

Previously, graphene under bending has typically been simulated using a continuum plate model or empirical interatomic potentials, largely due to the large unit cells required – a problem solved by OMD. It was illustrated that these approaches do not correspond to the physical molecular orbital description of graphene bending, but, nevertheless, they can be used to reproduce bending behavior. Some specific problems with the classical potential approaches are highlighted. Nearest-neighbor classical atomistic potentials are highly phenomenological and have no terms that are analogous to torsional misalignment. Additionally, specific properties of the functional form cause zero torsional stiffness at infinitesimal strains – an unrealistic result – and a tendency to overestimate the in-plane stiffness while underestimating the bending stiffness. Consideration of second-nearest-neighbors allows inclusion of a dihedral-angle term that can be thought of as analogous to torsional misalignment, but only if it is parametrized appropriately for graphene. Even when this term is appropriately parametrized, as in the second-generation Brenner potential, it still serves as an empirically-fitted part of an overall phenomenological scheme. This can result in unrealistic behavior in unanticipated cases, such as spurious bend-stretch coupling in graphene.

It is likely that this analysis and these computation methods can be applied to other atomic monolayers, such as hexagonal boron-nitride. The results and discussion may be instructive for design of interatomic potentials, and selection thereof for future studies.

Chapter 5

Ewald summation on a helix: A route to self-consistent charge density-functional based tight-binding objective molecular dynamics

5.1 Introduction

To carry out objective MD simulations with forces derived from electronic structure methods for structures with electrostatic and microscopic dispersion interactions, it is necessary to evaluate the potential at a reference point located at $\mathbf{X} = (r' \cos\gamma', -r' sin\gamma', T')$.

The electrostatic potential from an infinite helical distribution of unit point charges is

$$V(\mathbf{X}) = \sum_{\zeta=-\infty}^{+\infty}{}' \frac{1}{|\mathbf{X} - \mathbf{X}_\zeta|} \,, \tag{5.1}$$

while the dispersion part of the van der Waals energy is

$$W(\mathbf{X}) = \sum_{\zeta=-\infty}^{+\infty}{}' \frac{1}{|\mathbf{X} - \mathbf{X}_\zeta|^6} \,, \tag{5.2}$$

when $\mathbf{X}_\zeta$ are equidistantly distributed over an ideal helix, as shown in Fig. 5.1(a). The coordinates of the charges considered here correspond to the OMD case with only the helical operation h

$$\mathbf{X}_\zeta = \mathbf{R}^\zeta \mathbf{X}_0 + \zeta \mathbf{T}, \quad \zeta = -\infty, ..., +\infty \,. \tag{5.3}$$

Note that in the fundamental problem here, the repeating unit is just one point. In the above equation, there is a charge located at position $\mathbf{X}_0 = (r\cos\gamma_0, -rsin\gamma_0, T_0)$ in the $\zeta = 0$ cell. There is a singularity if $\mathbf{X}$ coincides with the position of $\mathbf{X}_0$. The symbol $\sum'$ indicates that in this situation, the singular term from $\zeta = 0$ is excluded from the summation. As per the usual OMD convention, the basic helical operation is defined by a rotation ofangle γ, described by the matrix $\mathbf{R}$, and a translation $\mathbf{T}$,

$$\mathbf{T} \equiv \begin{bmatrix} 0 \\ 0 \\ T \end{bmatrix} \tag{5.4}$$

$$\mathbf{R} \equiv \begin{bmatrix} \cos\gamma & -\sin\gamma & 0 \\ \sin\gamma & \cos\gamma & 0 \\ 0 & 0 & 1 \end{bmatrix} .$$

In fact, the fundamental problem of evaluating the electrostatic field generated by discrete charges distributed in helical patterns is encountered in a number of areas of modern science. For example in condensed matter physics, it is highly relevant for chiral charge-density waves [90] and for understanding the spin selective transport in helical molecular systems [91]. In biological physics and soft matter, this problem is important in understanding the relation between the helical structural and the generated local

electric field [92, 93, 94], the electrostatic interaction between biological helices [96, 95], and the electrostatic-driven helical patterns formed in fibers, nanotubes, and pores [97]. With the Green-function technique and cylindrical and helical coordinates, analytical solutions have been derived. Unfortunately, these formulas are quite complex and appear less usable in practice, especially when they are expressed in terms of helical Bessel functions [98]. Similar to the approach explored here, the electrostatic interaction between discrete helices of charge with parallel axes have been examined based on truncated Fourier expansions of the discrete Coulomb sums [95].

Direct numerical summations of Eq. (5.1) or Eq. (5.2) are computationally inefficient and become intractable in the context of molecular dynamics and electronic structure calculations. For bulk systems with translational symmetry, Ewald [99] techniques [100, 101, 102] are currently utilized to evaluate such summations. These are mixed space approaches based on the classical Ewald method presented in diverse textbooks [103, 104]. The short range contributions is evaluated in real space (where it decays rapidly) while the long range part is converted into a reciprocal space sum that is also fast converging. Originally proposed in three dimensions, the method has been generalized to one and two dimensions [105, 106, 107, 108]. Because objective MD renounces to translational symmetry, none of these approaches are applicable here. Unfortunately, the utility of a helical Ewald approach has not been yet explored. The generalization from helical objective boundary conditions to angular-helical boundary conditions is not considered here, as it is conceptually trivial. Objective boundary conditions are finite in the direction of the angular operation g, and thus the electrostatic and dispersion sums in the helical-angular case can simply be evaluated by direct summation of all of the angular images.

The particular objective here is to enable microscopic calculations in objective structures within the self-consistent charge (SCC) density-functional based tight-binding (DFTB) scheme [109]. Although non-SCC-DFTB coupled with OMD [86] can successfully model homonuclear structures [46, 47, 48, 83, 16, 112] (even having been used with dispersion forces, albeit in a less accurate, less efficient cutoff approximation [110]), and has been used for this purpose in the previous chapters, it is insufficient to tackle the rich variety of available helical nano- and bio-structures (for a recent review see Ref. [113]) showing complex microscopic interactions, or for describing large mechanical

deformations, or making credible predictions of new helical materials. The SCC-DFTB generalization is instead needed as it is more closely connected with first principles density functional theory (DFT) methods. As presented on several occasions [109, 114, 115], SCC-DFTB offers a superior description of chemical binding, especially in heteronuclear systems, while still being computationally efficient enough to allow for dynamical simulations. Both aspects are important for objective MD simulations of complex structures. The SCC-DFTB description is superior to force field approaches and, in fact, has even been used [115] as the high-level method in QM/MM simulations.

Unfortunately, evaluation of the aforementioned Coulomb sums on helices is a requirement for calculating the SCC-DFTB corrections in the objective MD framework. To approach this problem, the Ewald method is generalized to helical symmetry here. In Section 5.2 the Ewald formulas for Coulomb and dispersion sums are derived, and their applicability is demonstrated with a numerical example. In Section 5.3 it is indicated how these formulas are then used in the SCC-DFTB formalism. The power of the resultant method is next illustrated with proof of concept self-consistent simulations of a BN nanotube, a ZnO nanowire containing a screw dislocation, and an ideal DNA molecule including van der Waals interactions. All of the presented simulations are otherwise inaccessible to current methods without objective boundary conditions. Section 5.4 gives the conclusions.

5.2 The Helical Ewald Method

5.2.1 Coulomb Sums

The approach investigated here is a direct generalization of the original Ewald method [99]. To calculate the sum (5.1), the identity

$$\frac{1}{|\mathbf{X}-\mathbf{X}_\zeta|} = \frac{1}{\sqrt{\pi}} \int_0^\infty t^{-1/2} exp(-|\mathbf{X}-\mathbf{X}_\zeta|^2 t) dt \tag{5.5}$$

is employed, obtained based on the integral representation of the gamma function [116]. Next, with the help of an adjustable Ewald parameter η, the integration is split into long (V^L) and short (V^S) ranged terms

$$V^L = \sum_{\zeta=-\infty}^{+\infty}{}' \frac{1}{\sqrt{\pi}} \int_0^\eta t^{-1/2} exp(-|\mathbf{X}-\mathbf{X}_\zeta|^2 t) dt \tag{5.6}$$

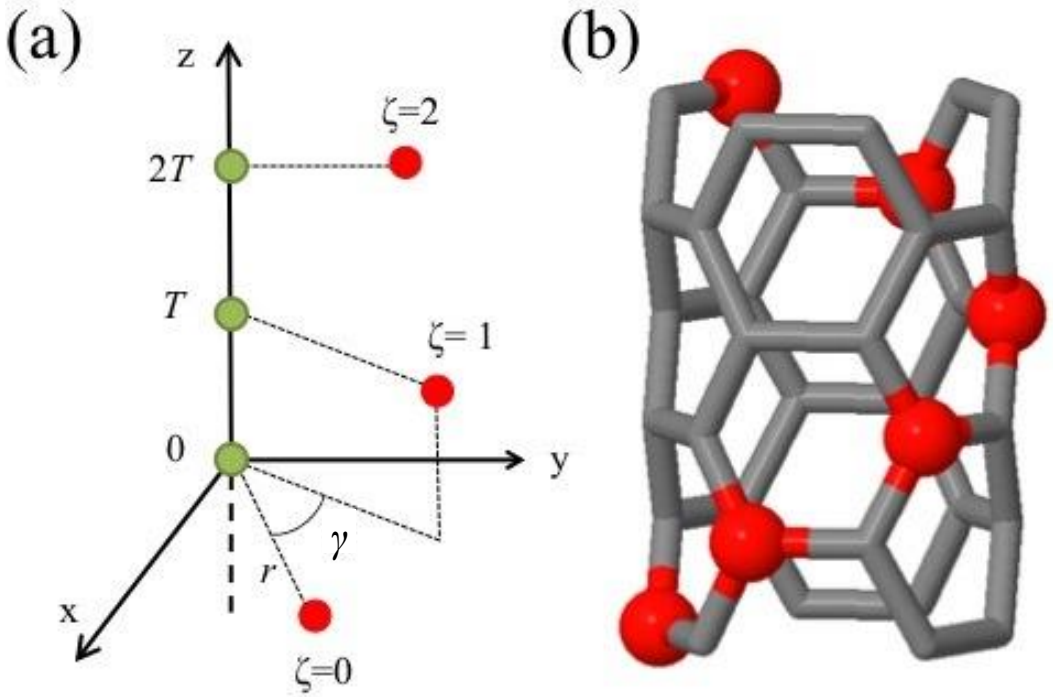

Figure 5.1: (a) Geometry for a discrete helical charge distribution, charges on the helix at sites $\zeta = 0, 1, 2$ are shown in red, while compensating charges on the axis are green. (b) Example of a helical distribution of atoms in a boron nitride nanotube with one helix marked as red sites.

and

$$V^S = \sum_{\zeta=-\infty}^{+\infty}{}' \frac{1}{\sqrt{\pi}} \int_\eta^\infty t^{-1/2} exp(-|\mathbf{X} - \mathbf{X}_\zeta|^2 t) dt. \tag{5.7}$$

The distance between the observation point, $\mathbf{X}$, and the location of charge ζ, at $\mathbf{X}_\zeta = (r\cos(\zeta\gamma + \gamma_0), -rsin(\zeta\gamma + \gamma_0), \zeta T + T_0)$, is

$$|\mathbf{X} - \mathbf{X}_\zeta|^2 = r^2 + r'^2 - 2rr'\cos(\zeta\gamma + \gamma_0 - \gamma') + (\zeta T + T_0 - T')^2. \tag{5.8}$$

Consider first V^L. Concerning the angular term in γ, it is important to Fourier

transform it as

$$e^{2rr'\cos(\zeta\gamma+\gamma_0-\gamma')t} = \sum_{l=-\infty}^{+\infty} I_l(2rr't)e^{-il(\zeta\gamma+\gamma_0-\gamma')}, \tag{5.9}$$

where index l is an integer and I_l is the modified Bessel function of the first kind. The translational part is appropriate for the standard Poisson summation formula [117, p. 69.], which in one-dimension allows for [118]

$$\begin{aligned}\sum_{\zeta=-\infty}^{+\infty} e^{-t(\zeta T+T_0-T')^2-il\zeta\gamma} &= \sum_{k=-\infty}^{+\infty}\int_{-\infty}^{+\infty} e^{-t(xT+T_0-T')^2}e^{-i(l\gamma+2\pi k)x}dx \\ &= \frac{\sqrt{\pi}}{T}\sum_{k=-\infty}^{+\infty} t^{-1/2}e^{-i(l\gamma+2\pi k)\frac{T'-T_0}{T}}e^{-\frac{(l\gamma+2\pi k)^2}{4tT^2}}.\end{aligned} \tag{5.10}$$

Combining these results, the above integration was solved after recognizing that it represents the Fourier transform of a Gaussian function. Thus,

$$\begin{aligned}V^L = \frac{1}{T}\sum_{l=-\infty}^{+\infty}\sum_{k=-\infty}^{+\infty} e^{-il(\gamma_0-\gamma')}e^{-i(l\gamma+2\pi k)\frac{T'-T_0}{T}}\int_0^{\eta} t^{-1}I_l(2rr't)e^{-\frac{(l\gamma+2\pi k)^2}{4tT^2}-(r^2+r'^2)t}dt \\ - 2\sqrt{\frac{\eta}{\pi}}\delta_{\mathbf{X}_0,\mathbf{X}}.\end{aligned} \tag{5.11}$$

The integral in the first term differs from the leaky aquifer function [119] encountered when performing Ewald summation in the pure one-dimensional case [106], due to the presence of the modified Bessel function. Notice also that the original Poisson formula still includes the $\zeta = 0$ term, regardless of the possible singularity mentioned above. The last term in the above equation is needed in order to insure consistency with Eq. (5.6).

The summation in Eq. (5.1) diverges because the infinite extent of the helix. This is remedied by using the concept of a compensating background charge. The key point is that this divergence is due to the $l = k = 0$ term of Eq. (5.11). It is eliminated by subtracting the $k = 0$ term [106] (itself divergent) arising from an equispaced line of counter charges located along the z-axis, starting at the origin and spaced at an interval of T, as depicted in Fig. 5.1(a). The corrected term then becomes

$$V^L_{l=k=0} = \frac{1}{T}\int_0^{\eta} t^{-1}I_0(2rr't)e^{-(r^2+r'^2)t}dt - \frac{1}{T}\int_0^{\eta} t^{-1}e^{-r'^2t}dt. \tag{5.12}$$

The remaining term can be written as

$$V^L_{l\&k\neq 0} = \frac{1}{T}\sum_{l=-\infty}^{+\infty}\sum_{k=-\infty}^{+\infty} e^{-il(\gamma_0-\gamma')}e^{-i(l\gamma+2\pi k)\frac{T'-T_0}{T}}\int_0^{\eta} t^{-1}I_l(2rr't)e^{-\frac{(l\gamma+2\pi k)^2}{4T^2t}-(r^2+r'^2)t}dt \quad (5.13)$$

To summarize, the long-ranged part of the electrostatic potential due to the helical charge distribution, less the background term, is

$$V^L = V^L_{l=k=0} + V^L_{l\&k\neq 0} - 2\sqrt{\frac{\eta}{\pi}}\delta_{\mathbf{X}_0,\mathbf{X}}. \quad (5.14)$$

The V^S term is treated with an approach similar to the one carried out for the one-dimensional lattice case [106]. After performing the change in variables $y_\zeta = |\mathbf{X}-\mathbf{X}_\zeta|^2 t$ and $y = r'^2 t$, one obtains

$$V^S = \sum_{\zeta=-\infty}^{+\infty}{}' \frac{1}{\sqrt{\pi}|\mathbf{X}-\mathbf{X}_\zeta|}\int_{\eta|\mathbf{X}-\mathbf{X}_\zeta|^2}^{\infty} y_\zeta^{-1/2}exp(-y_\zeta)dy_\zeta - \frac{1}{T}\int_{\eta r'^2}^{+\infty} y^{-1}e^{-y}dy \quad (5.15)$$

$$= \sum_{\zeta=-\infty}^{+\infty}{}' \frac{\Gamma(1/2,\eta|\mathbf{X}-\mathbf{X}_\zeta|^2)}{\sqrt{\pi}|\mathbf{X}-\mathbf{X}_\zeta|} - \frac{\Gamma(0,\eta r'^2)}{T}.$$

Here, Γ is the incomplete gamma function. The second term after the equal sign is the remaining short-range background contribution from the neutralizing line of charge.

This is how the above approach is used in practice. The infinite structure under objective boundary conditions is built from helical unit cells, Figs. 5.4(b), 5.5(b), 5.6(b). The quantity of interest is the electrostatic potential at a given atomic site due to all other atoms in the infinite structure. To calculate it, the infinitely long structure is viewed as a collection of infinitely-long helices with a common axis - each individual atom in the unit cell becomes a separate helix. For example, a (3,3) nanotube shown in Fig. 5.1(b) is composed of six helices such as the one delineated with big (red) balls. To each helix, one line of charges of opposite sign is added. As mentioned, these have a spacing of T and lay on the z-axis, starting at the origin. Thus, the lines of counter-charges from each helix coincide geometrically. Assuming the unit cell is neutral, when the contributions from all of the helices are summed to obtain the electrostatic potential, the effect of the counter-charges cancels out. An explicit example of this cancellation, for a unit cell comprised of two opposite charges is shown in Fig. 5.2. The neutralizing charges are revisited in Sec. 5.3, where the expression for the electrostatic potential is shown and a proof of the aforementioned cancellation is provided.

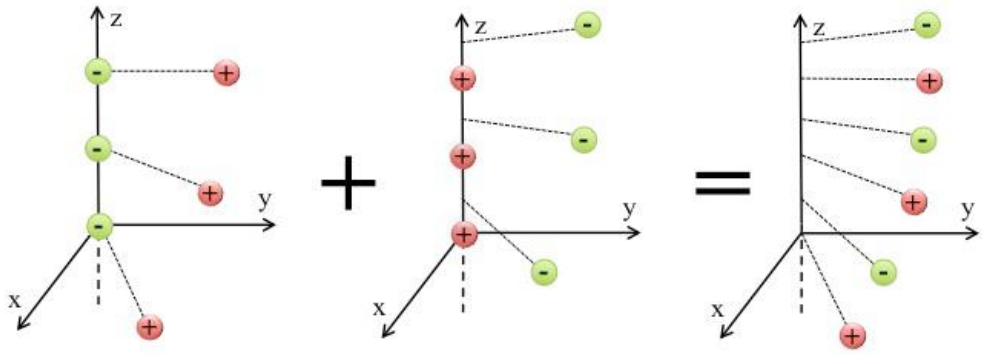

Figure 5.2: Demonstration of how individual helices arising from single atoms in the unit cell, compensated by counter-charges (Fig. 5.1 (a)), are combined to form the full neutral structure. The counter-charges cancel out completely and have no effect on the final result.

5.2.2 Dispersion Sums

To calculate the sum in Eq. (5.2), the identity

$$\frac{1}{|\mathbf{X}-\mathbf{X}_\zeta|^6} = \frac{1}{2}\int_0^\infty t^2 exp(-|\mathbf{X}-\mathbf{X}_\zeta|^2 t)dt \tag{5.16}$$

is used. As before, with the help of a controlling parameter η, Eq. (5.2) is split into long (W^L) and short (W^S) ranged components.

For W^L the result is

$$W^L = \frac{\sqrt{\pi}}{2T}\sum_{l=-\infty}^{+\infty}\sum_{k=-\infty}^{+\infty} e^{-il(\gamma_0-\gamma')}e^{-i(l\gamma+2\pi k)\frac{T'-T_0}{T}}\int_0^\eta t^{3/2} I_l(2rr't)e^{-\frac{(l\gamma+2\pi k)^2}{4tT^2}-(r^2+r'^2)t}dt - \frac{\eta^3}{6}\delta_{\mathbf{X}_0,\mathbf{X}}. \tag{5.17}$$

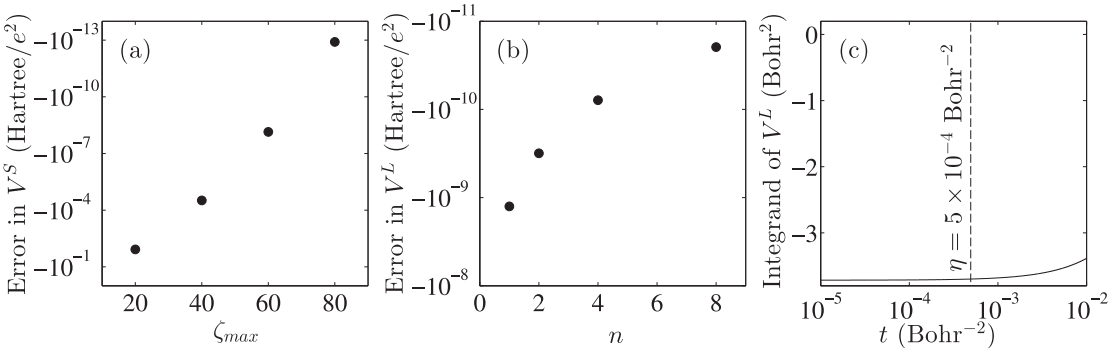

Figure 5.3: (a) Convergence of V^S with increasing ζ_{max}. (b) Convergence of V^L with the number of integration nodes n. (c) Integrand of V^L, showing upper limit of integration with dashed line.

Note that a background term is not needed here because Eq. (5.2) is convergent.

Regarding W^S, after performing the change in variables $y_\zeta = |\mathbf{X}-\mathbf{X}_\zeta|^2 t$ and $y = r'^2 t$, the result is

$$W^S = \sum_{\zeta=-\infty}^{+\infty}{}' \frac{1}{2|\mathbf{X}-\mathbf{X}_\zeta|^6} \int_{\eta|\mathbf{X}-\mathbf{X}_\zeta|^2}^{\infty} y_\zeta^2 exp(-y_\zeta) dy_\zeta = \sum_{\zeta=-\infty}^{+\infty}{}' \frac{\Gamma(3, \eta|\mathbf{X}-\mathbf{X}_\zeta|^2)}{2|\mathbf{X}-\mathbf{X}_\zeta|^6}. \quad (5.18)$$

5.2.3 Numerical Example

It is not immediately obvious if the formulas presented above are numerically tractable and accurate in a truncated form, i.e. when indices $|\zeta|$, $|l|$, and $|k|$ are bounded by ζ_{max}, l_{max}, and k_{max}, respectively. The evaluation of the integral in V^L also introduce some complexity as it requires a quadrature over the variable t, typically discretized as n nodes.

The Ewald formulas for V and W have been implemented into as an independent Fortran module (see Appendix D). Here, the applicability of the electrostatic sums for a simple numerical example is explored. The geometry of the $(3,3)$ nanotube shown in Fig. 5.1(b) is used, on translating by $T = 1.42$ Å along z the unit cell repeats with a rotation of $\gamma = 60°$. To calculate the Ewald sum for the interaction of an atom with its helical images (such as the set of atoms highlighted in red in Fig. 5.1(b)), $\mathbf{X}'$ and $\mathbf{X}_0$ are placed on the surface of a tube of radius of $r = r' = 1.02$ Å. The rest of the

quantities are taken $\gamma' = \gamma_0 = T' = T_0 = 0$.

The Ewald approach is robust since, when converged, the result will not depend on the specific value for the controlling parameter η. However, careful selection of η is desirable for increasing the computational efficiency as the numerical approach is a balancing act between the cost of V^L and V^S evaluations. Lowering η increases the ζ_{max} that needs to be considered for the sum in V^S, but decreases the l_{max}, k_{max} and n required for the V^L term to converge. Trial runs revel that the sum V^S can be computed relatively quickly, and, as can be seen from Fig. 5.3(a), converges approximately exponentially with ζ_{max}. The function evaluation and numerical integration (using a simple trapezoidal rule) involved in calculating V^L is more time-consuming and shows only an approximately power law convergence with the number of nodes (Fig. 5.3(b)). Therefore, the optimal choice for η is small. So small as a matter of fact, that V^S is dominant enough to be considered a first-order approximation to V. In this case, $\eta = 5 \times 10^{-4}$ Bohr^{-2} provides a fast computational time, for which $V^S = -0.542$ Hartree$/e^2$, while $V^L = -0.0259$ Hartree$/e^2$. Here e is the electron charge.

The number of summation indices and numerical integration nodes required to achieve a precision greater than 10^{-10} Hartree$/e^2$ is now examined. From Fig. 5.3(a) it can be seen that $\zeta_{max} = 80$ is more than sufficient for this precision in V^S. Regarding V^L, because the variable of integration t is kept small, the exponential factor $exp(-\frac{(l\gamma+2\pi k)^2}{4T^2t})$ in the integrand of Eq. (5.13) decays extremely quickly with $l\gamma + 2\pi k$. Thus, $|k| > 0$ terms almost never have to be considered, and $|l| > 0$ terms do not have to be considered when γ is large, such as in this example. Fig. 5.3(b) shows that $n = 8$ is sufficient to reach the desired accuracy. This is because the integrand of V^L is relatively flat in the interval of integration $0 < t < \eta$, Fig. 5.3(c). The computational time required with these values is nearly negligible, ~ 10 ms on a single core. The errors shown in Fig. 5.3 are calculated with respect to V^S evaluated with $\zeta_{max} = 160$ and V^L evaluated with $n = 1,000,000$. These quantities are converged to 10^{-15} Hartree$/e^2$ - doubling the parameters produces identical results to that precision. As expected, increasing (reducing) η requires a lower (higher) value of ζ_{max} in the evaluation of V^S, while increasing (decreasing) l_{max} and n in evaluating V^L. The optimal ηT^2 value increases with decreasing r/T and r'/T.

When γ is small however, the $k = 0$, $|l| > 0$ terms of V^L need to be also considered.

Because the integrands become more non-linear, an increased number of nodes of integration will be required. Thus, for small γ, it is even more important to keep η small to reduce the computational effort of computing V^L. This, in turn, would require more terms to be considered in the V^S sum.

5.3 SCC-DFTB under objective boundary conditions

The above results are encouraging, and thus the developed module was used to couple SCC-DFTB to the helical symmetry. This represents the key step for developing the SCC-DFTB objective MD capability.

As before, consider an infinite objective structure possessing the helical symmetry of operation h

$$\mathbf{X}_{i,\zeta} = \zeta\mathbf{T} + \mathbf{R}^{\zeta}\mathbf{X}_{i,0}, \quad i = 1, ..., n_h, \quad -\infty < \zeta < \infty. \tag{5.19}$$

$$\mathbf{T} \equiv \begin{bmatrix} 0 \\ 0 \\ T \end{bmatrix}$$

$$\mathbf{R} \equiv \begin{bmatrix} \cos\gamma & -\sin\gamma & 0 \\ \sin\gamma & \cos\gamma & 0 \\ 0 & 0 & 1 \end{bmatrix}.$$

Note that now the full structure is being considered, with multiple atoms n_h in the objective simulation cell.

Recall that in the expansion of the DFT energy with respect to charge density fluctuation $\delta n(\mathbf{r})$ (Eq. 2.11), the second-order and higher terms $O([\delta n(\mathbf{r})]^2)$ were neglected. When explicitly written, the second-order term is, using the same notation and integral shorthand as in Sec. 2.4,

$$\frac{1}{2}\int\int'\left(\frac{1}{|\mathbf{r}-\mathbf{r}'|} + \frac{\delta^2 E_{XC}}{\delta n \delta n'}\Big|_{n_0(\mathbf{r})}\right)\delta n(\mathbf{r})\delta n'(\mathbf{r}), \tag{5.20}$$

where the second term inside the parentheses indicates a second functional derivative evaluated at the reference density $n_0(\mathbf{r})$. The charge density fluctiation $\delta n(\mathbf{r})$ can be expanded in terms of atom-centered terms, e.g. $\delta n_i(\mathbf{r})$ centered on atom i located at $\mathbf{X}_i$. Each of these atom-centered terms is a sum of spherical harmonics Y_{ml}, each multiplied

by a radial dependence. In SCC-DFTB, only the lowest spherical harmonic is kept, i.e. the atom-centered terms $\delta n_i(\mathbf{r})$ are purely radial[109]:

$$\delta n_i(|\mathbf{r}-\mathbf{X}_i|) = \Delta q_i F_{00}^i(|\mathbf{r}-\mathbf{X}_i|)Y_{00}, \tag{5.21}$$

where Δq_i is the change (with respect to neutrality) in the total charge associated with atom i, and F_{00}^i is the radial dependence normalized so that $\int \delta n_i(|\mathbf{r}-\mathbf{X}_i|) = \Delta q_i$. In this fashion, the fluctuation in the electron density is related to the charges on each atom. Substituting Eq. 5.21 into Eq. 5.20, one gets the second-order correction to the DFTB energy

$$E_{2nd} = \frac{1}{2}\sum_{i,j} \Delta q_i \Delta q_j \gamma_{ij}, \tag{5.22}$$

where the sum runs over all atom pairs i, j and

$$\gamma_{ij} = \int\int' \Gamma[\mathbf{r}, \mathbf{r}', n_0(\mathbf{r})] \frac{F_{00}^i(|\mathbf{r}-\mathbf{X}_i|)F_{00}^j(|\mathbf{r}'-\mathbf{X}_j|)}{4\pi}, \tag{5.23}$$

where Γ is a functional that lumps together the terms that are inside the parentheses in Eq. 5.20 – the Hartree and the exchange-correlation coefficients. The task now is to construct a simple method to approximate γ_{ij}. Consider first the self-interaction limit, γ_{ii}. In this case, the simple approximation is made that $\gamma_{ii} = U_i$[109], where U_i is the Hubbard parameter for atom i, calculated as the the second derivative of the energy of the atom i with respect to the occupation number of the highest occupied atomic orbital. It is approximately equal to double the chemical hardness of atom i, η_i. This is calculated *a priori* with DFT, and is thus a well-defined, non-empirical parameter. Now, to estimate γ_{ij} for separate atoms, first the spherical charge density of atom i is taken as $n_i(|\mathbf{r}-\mathbf{X}_i|) = \frac{\tau_i^3}{8\pi}e^{-\tau_i|\mathbf{r}-\mathbf{X}_i|}$, in accordance to the Slater-type orbitals used in the DFT calculations that DFTB is fitted to[109]. Here τ_i is some atom-dependent parameter. This determines the form of $F_{00}^i(|\mathbf{r}-\mathbf{X}_i|)$ and $F_{00}^j(|\mathbf{r}'-\mathbf{X}_j|)$ in Eq. 5.23. Now, the exchange-correlation part of Γ is ignored, and the integrals are computed, resulting in a pairwise term

$$\gamma_{ij}(|\mathbf{X}_j-\mathbf{X}_i|) = \frac{1}{|\mathbf{X}_j-\mathbf{X}_i|} - S(\tau_i, \tau_j, |\mathbf{X}_j-\mathbf{X}_i|), \tag{5.24}$$

where S is a short-range function with exponential decay (for an exact form see Ref. [109]). Setting $i = j$, letting $|\mathbf{X}_i - \mathbf{X}_i| \to 0$, and expanding Eq. 5.24 results in $\gamma_{ii} = \frac{5}{16}\tau_i$. Equating this with the previous estimate of $\gamma_{ii} = U_i$ fixes the unknown parameter τ_i for every atom i.

Thus, Eq. 5.24 is now fully determined, and, by extension, so is Eq. 5.22:

$$E_{2nd} = \frac{1}{2}\sum_{i,j}\frac{\Delta q_i \Delta q_j}{|\mathbf{X}_j - \mathbf{X}_i|} - \frac{1}{2}\sum_{i,j}\Delta q_i \Delta q_j S_{ij}(|\mathbf{X}_j - \mathbf{X}_i|). \tag{5.25}$$

For an extended structure, the sums are evaluated between an atom j and the atom i, as well as all images of i. The second sum is a short-range two-body term and can be evaluated in direct space by considering a handful of images adjacent to the simulation cell. It also now clear how the Ewald sums enter the energy expression. The first term is a long-range electrostatic term that can be rewritten as

$$E^{es}_{2nd} = \frac{1}{2}\sum_{j}\Delta q_j V_j, \tag{5.26}$$

where the sum runs over all atoms j in the simulation cell and V_j is the electrostatic potential at atom j due to the rest of the structure,

$$V_j = \sum_i \Delta q_i \sum_\zeta{}' \frac{1}{|\mathbf{X}_j - \mathbf{X}_{i\zeta}|} = \sum_i \Delta q_i V(\mathbf{X}_j)|_{\mathbf{X}_0 = \mathbf{X}_i}, \tag{5.27}$$

where the sum runs over all atoms j in the simulation cell and $V(\mathbf{X}_j)|_{\mathbf{X}_0=\mathbf{X}_i}$ is precisely the electrostatic potential from Eq. 5.1 evaluated at $\mathbf{X}_j$ due to a helix of atoms originating at $\mathbf{X}_i$. This can be evaluated with Eqs. 5.14 and 5.15, completing the calculation of E_{2nd}.

To calculate the total electronic energy of the system, E_{2nd} is added to the band structure energy $E_{bs} = \sum_\lambda^{occ}\langle\Psi_\lambda|\hat{H}_0|\Psi_\lambda\rangle$, which is calculated in the same way as described in Sec. 2.4. However, there is a correction to the Hamiltonian matrix elements. This is because when charge transfer occurs between atoms, the atomic-like (and consequently the crystal-like) orbitals are changed, as they become "less than one electron" or "more than one electron". The SCC matrix elements read

$$\mathbf{H}^{\kappa}_{i\alpha j\beta}{}^{SCC} = \mathbf{H}^{\kappa}_{i\alpha j\beta} + \frac{1}{2}\mathbf{S}^{\kappa}_{i\alpha j\beta}\sum_{n}(\gamma_{in}+\gamma_{jn})\Delta q_n$$

$$= \mathbf{H}^{\kappa}_{i\alpha j\beta} + \frac{1}{2}\mathbf{S}^{\kappa}_{i\alpha j\beta}\sum_{n}\Delta q_n[V(\mathbf{X}_i)|_{\mathbf{X}_0=\mathbf{X}_n} + V(\mathbf{X}_j)|_{\mathbf{X}_0=\mathbf{X}_n} + S_{in} + S_{jn}]$$

$$= \mathbf{H}^{\kappa}_{i\alpha j\beta} + \frac{1}{2}\mathbf{S}^{\kappa}_{i\alpha j\beta}(V_i + V_j + \sum_{n}\Delta q_n[S_{in}+S_{jn}]), \tag{5.28}$$

where the sum runs over all atoms n in the simulation cell and all of their images, and $\mathbf{H}^{\kappa}_{i\alpha j\beta}$ and $\mathbf{S}^{\kappa}_{i\alpha j\beta}$ are the non-SCC Hamiltonian and overlap matrix elements as defined in Sec. 2.4 (because there is no angular symmetry, the matrix elements are not l-dependent). The overlap matrix is unchanged by SCC. As before with γ_{ij}, the sum of γ_{in} and γ_{jn} is split into short-range and long-range interactions, the short-range interactions being evaluated directly over a small amount of neighboring cells, and the long-range interactions being sums of electrostatic potentials (Eq. 5.1), evaluated at $\mathbf{X}_i$ and $\mathbf{X}_j$, due to helices originating at $\mathbf{X}_n$, which ultimately sum to the total potentials at $\mathbf{X}_i$ and $\mathbf{X}_j$, termed V_i and V_j (Eq. 5.27). With this matrix, the generalized eigenvalue problem can be solved, the energies filled, averaged over the first Brillouin zone, and E_{bs} obtained.

The final piece of the puzzle is finding Δq_i for each atom i – they are still unknown! They are obtained by Mulliken charge analysis from the LCAO coefficients, $c^{\lambda}_{i\alpha}$ which form the eigenvectors $\mathbf{c}^{\lambda}$ of the generalized eigenvalue equation.

$$\Delta q_i = \left[\sum_{\lambda}^{occ}\sum_{\alpha}\sum_{j\beta}(c^{\lambda *}_{i\alpha}c^{\lambda}_{j\beta}S_{i\alpha j\beta} + c^{\lambda *}_{j\beta}c^{\lambda}_{i\alpha}S_{j\beta i\alpha})\right] - q^0_i, \tag{5.29}$$

where q^0_i is the Mulliken charge calculated for a neutral atom. For helical objective systems, this is κ-dependent and needs to be averaged. However, we have a problem: the charges are both determined by the generalized eigenvalue equation, and determine the Hamiltonian matrix in the equation. This where the self-consistent procedure comes into play. Some charges are assumed, then the eigenvalue problem is solved with a Hamiltonian matrix based on those charges. The procedure is iterated, adjusting the charges used in constructing the Hamiltonian matrix, until the charges resulting from the solution match those used for matrix construction.

Finally, note that a repulsive pairwise energy E_{pair} is still present, to capture ionic repulsion, as well as electronic effects omitted by the various approximations made.

It is now shown why the neutralizing lines of charges in this implementation do not affect the value of V_j. When the counter-charges are explicitly included, Eq. (5.27) becomes $V_j = \sum_{i=1}^{n_h} \sum_{\zeta=-\infty}^{\prime\infty} \Delta q_i (\frac{1}{|\mathbf{X}_j - \mathbf{X}_{i,\zeta}|} - \frac{1}{|\mathbf{X}_j - \mathbf{X}_{c,\zeta}|})$. Here, the additional term is the potential due to the infinite line of counter-charges $\mathbf{X}_{c,\zeta}$ located on the z-axis at z= $(-\infty, ..., -2T, -T, 0, T, 2T, ..., \infty)$. In the present Ewald implementation, it is comprised of the latter terms of eqs. (5.12) and (5.15). However, since the locations of the counter-charges are identical for each helix (independent of i), one can write $V_j = \sum_{i=1}^{n_h}{}' \sum_{\zeta=-\infty}^{\infty} \frac{\Delta q_i}{|\mathbf{X}_j - \mathbf{X}_{i,\zeta}|} - \sum_{\zeta=-\infty}^{\infty} \frac{1}{|\mathbf{X}_j - \mathbf{X}_{c,\zeta}|} \sum_{i=1}^{n_h} \Delta q_i$. For a neutral system, $\sum_{i=1}^{n_h} \Delta q_i$ is zero, thus the value of V_j is not affected by the introduction of the counter-charges.

The original DFTB has deficiencies in describing the long-ranged dispersion forces. To remedy this, a van der Waals term is added to the SCC-DFTB energy [121, 122, 110]. Its long range attractive component is

$$E_{dis} = -\sum_{j=1}^{n_h} W_j \tag{5.30}$$

where

$$W_j = \sum_{i=1}^{n_h} \sum_{\zeta=-\infty}^{\infty}{}' \frac{C_6^{ij}}{|\mathbf{X}_j - \mathbf{X}_{i,\zeta}|^6}. \tag{5.31}$$

Here C_6^{ij} is the van der Waals coefficient between atoms i and j. W_j represents the attraction between atom j and the atoms distributed over helices, labeled by i. It will be evaluated with Eqns. (5.17) and (5.18).

Thus, the classical Ewald summation method for both electrostatic and dispersion interactions, which has previously only been able to treat systems with translational symmetry, has successfully been generalized to helical boundary conditions. This pivotal development, combined with the previously developed coupling of non-SCC DFTB with objective molecular dynamics [46], allows the implementation of objective SCC-DFTB. The implementation detailed here is helical-only, without consideration of the pure angular operation g. As mentioned, however, the sum over the finite angula operation can be carried out directly, and thus is a conceptually trivial development.

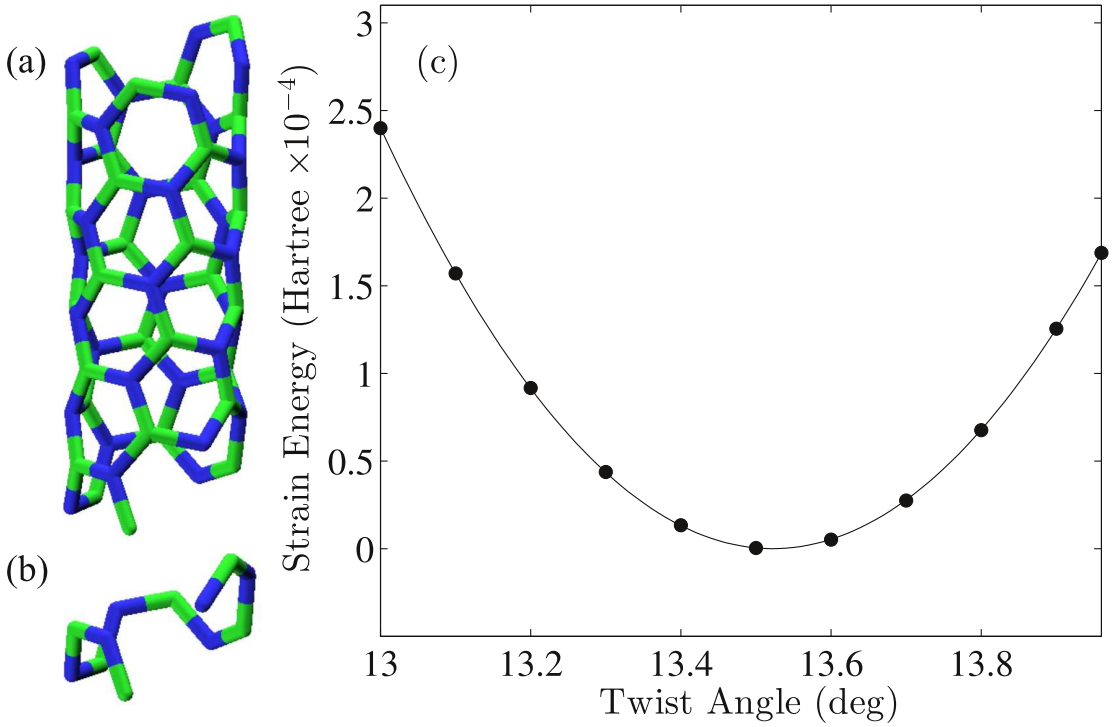

Figure 5.4: SCC-DFTB simulation of intrinsic twist of $(4, 2)$ BN nanotube. (a) Atomic structure and (b) objective computational domain containing $n_h = 12$ atoms. (c) Minimization of strain energy with respect to twist angle.

Helical SCC-DFTB was implemented in the DFTB+ [120] simulation package. Presented below are structural relaxations of several sample helical structures. The simulations were considered converged when the magnitude of the maximum force on any atom was less than 1.0^{-4} Hartree/Bohr.

5.3.1 Chiral BN Nanotube

First, the method is demonstreated for one-atom-thick heteronuclear nanotubes. This system demonstrates the suitability of the proposed electrostatic approach when $r \approx r'$ and angle γ is relatively large.

The advantages of simulating nanotubes with OMD instead of PBC were well-established in Chapter 4. Here, a boron nitride nanotube is considered, rolled from

a planar sheet of hexagonal boron nitride instead of graphene.

As briefly mentioned in Chapter 4, it has recently been obtained with non-SCC-DFTB objective MD that a general (n, m) nanotube can lose the translational periodicity predicted by the rolled-up construction due to a shear strain manifested as an intrinsic structural twist; for such cases, simulations relying on translational symmetry would become even more demanding [52].

Because only helical symmetry is used, the simulation cell is not the two-atom cell used for graphene in Chapter 4. For the $(4, 2)$ BN nanotube, Fig. 5.4(a), a computational cell consisting of six B-N dimers (12 atoms) is used, following the screw-dislocation procedure described in Refs. [47, 52] (Fig. 5.4(b)). The SCC treatment allows for better description of the partially ionic bonding in BN. The most up to date DFTB parameters are used [123].

The numerical parameters and maximum summation indices listed in Table 5.1 are used in order to achieve a tolerance of $< 10^{-10}$ Hartree in the electrostatic energy with this configuration, with the k-point grid chosen based on the ideas of Ref. [124]. The error is calculated by increasing the integration nodes and maximum summation indices – the bare minimum values required for this level of convergence are listed in parentheses. Starting with the ideal rolled-up configuration (modified to match each twist rate value examined), conjugate-gradient relaxations are performed. These calculations involved two stages: first the atomic positions with fixed twist angle γ at constant T were relaxed. Next, the NT parameter T was optimized for these atomic coordinates, at the considered γ. These simulations take only a few minutes each on a single core.

The net Mulliken charges on B and N atoms are found to be $\pm$ 0.366 e. The energy due to the Coulomb part of the SCC correction is -0.438 Hartree for the 12-atom unit cell. For comparison, this value was also evalued using direct summation. Over 4000 images in each direction are required to reach a tolerance of $< 10^{-10}$ Hartree, a significantly increased computational effort compared to the Ewald approach. The numerical values are equal up to this tolerance, demonstrating the validity of the Ewald method. The total energy difference due to the introduction of SCC corrections, including the Coulomb interaction, the short-range corrections, and the self-consistent adjustment of the wavefunction expansions, is +0.0231 Hartree.

The ideal roll-up construction predicts values for γ and T of 12.86°/cell and 2.466 Å/cell,

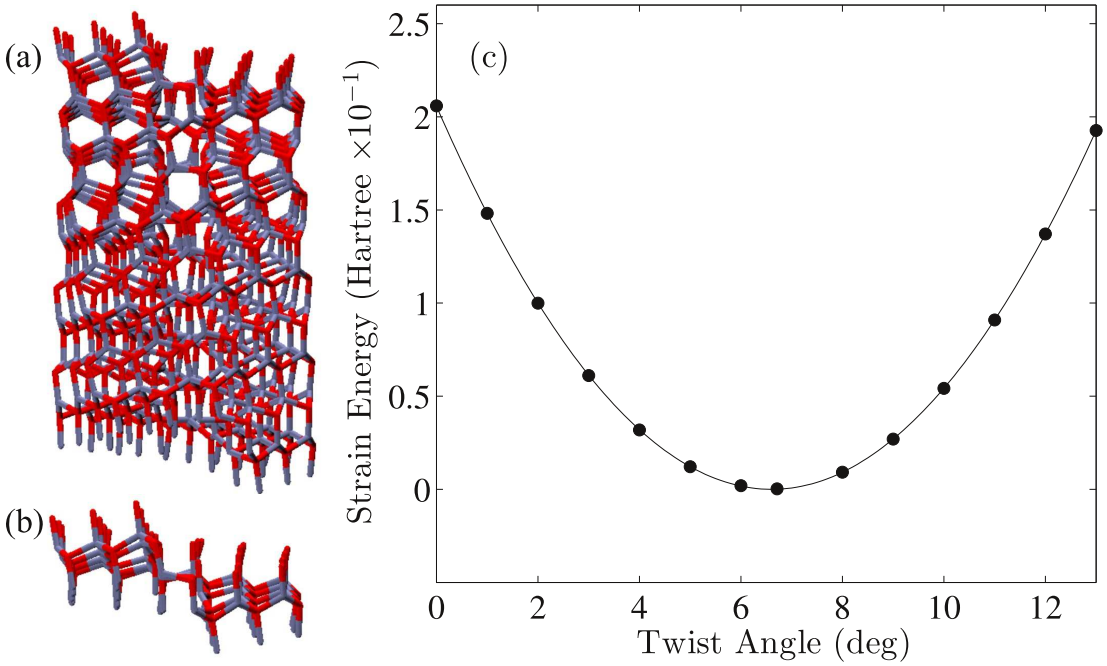

Figure 5.5: SCC-DFTB simulation of Eshelby twist of a ZnO nanowire. (a) Atomic structure and (b) objective computational domain containing $n_h = 108$ atoms. (c) Minimization of strain energy with respect to twist angle, showing an Eshelby twist of 6.61°.

respectively. As can be seen in Fig. 5.4(c), the untwisted (rolled-up) morphology does not correspond to a metastable state, in agreement with previous predictions [52]. The analogous non-SCC simulations predicts a twist angle of 13.51°/cell and a length of 2.520 Å/cell. The present simulation predicts a very similar twist angle of 13.52°/cell, and a significantly differing (0.3 % strain) length of 2.513 Å/cell.

5.3.2 Screw-Dislocated ZnO Nanowire

The method is now demonstrated for heteronuclear nanowires, when γ is small and $r \neq r'$ occurs. As shown in Chapter 3 for homonuclear silicon nanowires (the hydrogen passivation does not affect the properties significantly) and experimentally observed[65], when a thin rod contains an axial screw dislocation, it becomes intrinsically twisted [74]. This twist makes it impossible or difficult to simulate screw-dislocated nanowires using

PBC. Thus, objective MD is necessary to model screw-dislocated nanowires in their fully relaxed configuration. In Refs. [125, 126], screw-dislocated ZnO nanowires were studied with the non-SCC DFTB method coupled with OMD. SCC provides an improved description of the binding by including the effects of electronic charge transfer from Zn to O.

The optimal length and twist of a ZnO nanowire of 8.53 Å radius extending along the [0001] direction is calculated, Fig. 5.5(a). The wire contains a centered axial screw dislocation, with the 5.4 Å minimum Burger's vector allowable in ZnO. The simulation cell contains 108 atoms, the same as in the minimum translational cell of the wire, Fig. 5.5(b). As before, a tolerance of 10^{-10} Hartree is the goal, and the numerical Ewald parameters used are listed in Table 5.1. The increased number of integration nodes required for the 0° case stems from the increased importance of the finite-l terms (here $l_{max} = 1$) at small angles. In general, because the integrand of the finite-l terms is more nonlinear, more nodes of integration are needed.

The simulations start with relaxed configurations previously obtained with non-SCC-DFTB, or SCC results geometrically twisted to predict a configuration at a new angle (e.g. by applying the ideal geometric twist to the the simulation result at 1° to begin the 2° simulation). Each full conjugate-gradient relaxation took several hours (less than 10) on a single core.

The net charges on the Zn and O atoms range ±0.432–0.575 e. The total energy difference due to the introduction of SCC corrections is +1.07 Hartree for the 108-atom unit cell. The previous, non-SCC study of this structure predicted a twist angle of 6.71°/cell and a length of 5.32 Å/cell [125]. The introduction of SCC changes these values to 6.61°/cell and 5.28 Å/cell, respectively, Fig. 5.5(c), confirming that these relaxed structures and their the amount of twist can be rationalized with Eshelby's model [74].

5.3.3 DNA Strand

Finally, the simulation of heteronuclear biomolecules with this method is demonstrated, when γ is large and $r \neq r'$ is possible. Here, a larger number of atomic species is present and both the electrostatic and van der Waals sums are simultaneously needed.

Biomolecules are perhaps the most obvious application for objective MD coupled

Table 5.1: SCC-DFTB calculations under objective boundary conditions. Numerical parameters required to reach a tolerance of 10^{-10} Hartree in helical Ewald summation of different structures and configurations considered. In order: Ewald split parameter η, maximum short-range summation index ζ_{max}, maximum long-range summation indices l_{max} and k_{max}, and number of nodes n used for numerical integration of V^L. Number of k-points required for energy convergence also listed. Actual parameters used listed first, bare minimum parameters required to reach required tolerance listed in parentheses.

Structure	η (Bohr^{-2})	ζ_{max}	l_{max}	k_{max}	n	k-points
$(4,2)$ BN nanotube	5×10^{-5}	500(200)	1(0)	1(0)	100(<50)	20(10)
ZnO nanowire:						
$\gamma \geq 1^\circ$	5×10^{-5}	100(<50)	2(1)	1(0)	100(<50)	10(5)
$\gamma = 0^\circ$	5×10^{-5}	100(<50)	2(1)	1(0)	1000(500)	10(5)
DNA:						
V	5×10^{-5}	200(100)	1(0)	1(0)	100(50)	10(5)
W	5×10^{-5}	100(50)	1(0)	1(0)	100(50)	

with SCC-DFTB and dispersion. They often possess helical symmetry, and are almost universally characterized by dispersion interactions. All biomolecules are heteronuclear, requiring the consideration of charge transfer for the most accurate description possible. As an emblematic example, here an ideal single strand of DNA is considered.

Traditionally, DNA is simulated using either a cluster approximations or by PBC with the particle mesh Ewald method [127, 128]. Both of these methods can be problematic. Cluster simulations may introduce spurious end effects, and make the treatment of long strands of DNA computationally intensive. PBC overcomes these issues, but imposes translational symmetry constraints on the structure. The number of atoms in the PBC cell is large – the situation is analogous to that of helical nanowires – and quantum treatments becomes less applicable. For this reason, simulations of DNA are typically carried out using empirical force-field models [127].

The objective method carries none of these drawbacks. Segments of arbitrary length may be simulated as part of an infinite helix possessing arbitrary twist, allowing for study of sequence-dependent or general properties without end effects. Additionally, the objective simulation cells typically contain a small number of atoms, permitting the

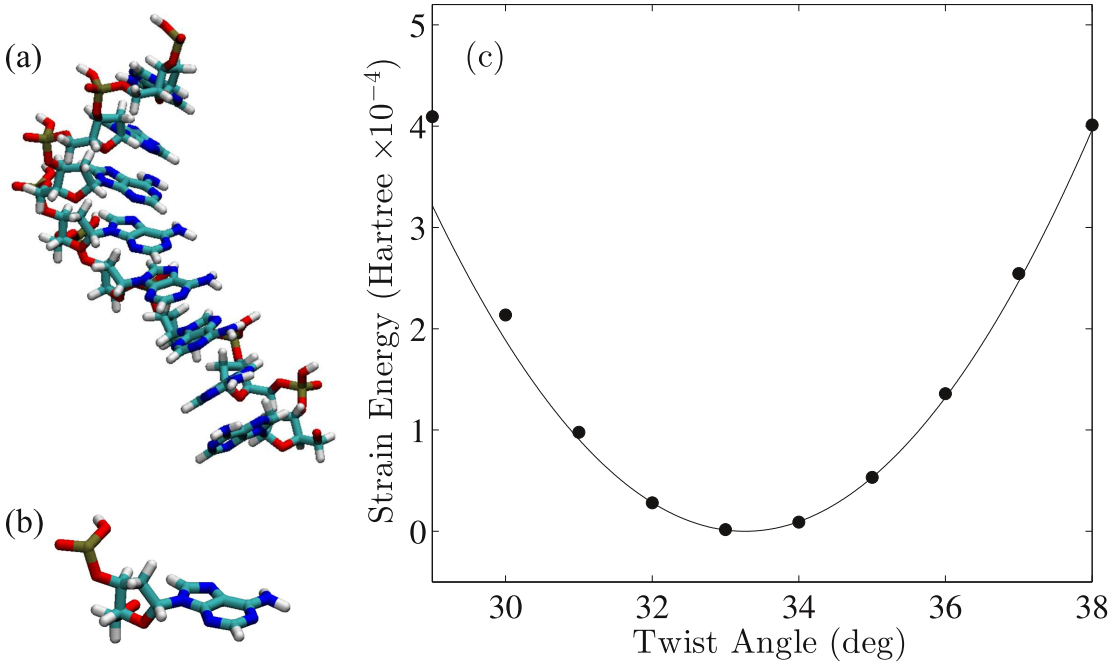

Figure 5.6: SCC-DFTB determination of optimal twist of a DNA molecule with $T = 3.38$ Å. (a) Relaxed atomic structure and (b) objective computational domain containing $n_h = 33$ atoms. (c) Minimization of the strain energy with respect to twist angle, showing optimal twist of 33.27°/cell. Quadratic curve is fitted only to the four points nearest to the minimum. The torsional stiffness is 0.329 Hartree Å.

application of SCC-DFTB, which offers superior description of the interatomic interactions.

A series of calculations on a single strand DNA molecule – a helix comprised of adenosine nucleotides – ar successfully carried out Fig. 5.6(a). The computational cell contains 33 atoms and comprises a single nucleotide, as shown in Fig. 5.6(b). Because DNA is a soft structure with many possible metastable configurations [127], this demonstration is focused on the determination of the optimal twist angle at a fixed $T = 3.38$ Å. This is the typical value for the DNA B-type double helix, which was used as the starting configuration for the single-helix simulation. The coordinates used are the default coordinates generated for the B-helix by the `nab` language [129, 130, 131]. Formerly, in order to apply PBC to a DNA structure, investigators had to impose the constraint

that there must be an integer number of nucleotides within one or a few 360-degree turns of the helix. This artificial constraint runs contrary to the highly flexible and variable nature of the DNA configuration, and is not required here. The twist per single nucleotide is arbitrary and may represent a structure that possesses no translational periodicity whatsoever.

The interatomic interactions involving elements P, O, N, C, H were described with the mio-1-1 parameter set [109, 132]. The required accuracy remains at 10^{-10} Hartree, and the values for both the V and W sums are shown in Table 5.1. These simulations take several hours (less than 5) on a single core, implying also that SCC-DFTB calculations on larger objective cells (containing an integer multiple repeat of the 33 atom cell) should be tractable. The optimal twist is 33.27°/cell, see Fig. 5.6(c). Thus, this simulation predicts that the single helix differs significantly from the 36°/cell twist angle typically associated with the B-double helix. The optimized structure does not possess translational periodicity over any reasonable length. Its behavior deviates significantly from linear elasticity in the angle range studied. This is to be expected when such a soft material, with a complicated configuration space, is placed under large strain. Thus, the quadratic fitting is restricted to the four points closest to the minimum. The torsional stiffness is 0.329 Hartree Å. The P atom is the most positively charged with 1.23 e, while the O atoms carry varying negative charges, as large as -0.62 e. The other atoms are all closer to neutral. The total dispersion energy is +0.14 Hartree for the 33-atom cell, while the total energy difference due to SCC corrections (not including dispersion) is of a similar value, +0.15 Hartree.

5.4 Conclusions

In this chapter, it is demonstrated that the generalization of the Ewald method to a helical geometry gives numerically tractable formulas for both the electrostatic potential and van der Waals energies. This approach provides an elegant and robust way to incorporate helical symmetry into self-consistent treatments of the interatomic interactions, including SCC-DFTB and DFT. Proof of concept SCC-DFTB simulations are successfully under objective bounder conditions in charge-neutral heteronuclear nano- and bio-structures with various levels of complexity. Overall, objective MD benefits

immensely from the coupling with SCC-DFTB as it increases the number and variety of objective structures which can be simulated with unprecedented accuracy. It is further appealing to explore the formulated expression for the Coulomb sum against the background provided by the neutralizing line of charge even in charged-cell objective calculations, to compute for example formation energies of charged defects in objective structures.

Chapter 6

Nanoscale Bending of Multilayered Boron Nitride and Graphene Ribbons: Experiment and Objective Molecular Dynamics Calculations

Adapted from I. Nikiforov, D.-M. Tang, X. Wei, T. Dumitrică, and D. Golberg, Nanoscale Bending of Multilayered Boron Nitride and Graphene Ribbons: Experiment and Objective Molecular Dynamics Calculations, *Phys. Rev. Lett.* **109**, 025504 (2012) (`http://journals.aps.org/prl/abstract/10.1103/PhysRevLett.109.025504`) [2].

6.1 Introduction

Recently, there has been an increased interest in understanding the physical properties of multilayered structures of graphene and hexagonal boron nitride (h-BN), such as nanosheets and nanoribbons (NRs) [133, 134, 135]. A common feature of these materials

is that they have a highly anisotropic layered structure. The atoms within individual layers possess strong short-ranged covalent bonding, while the interlayer binding is via comparatively weak long-ranged van der Waals (vdW) forces. Despite the relative weakness of the vdW binding, there is significant energetic advantage in maintaining Bernal stacking where the atoms in sequential layers do not eclipse each other [110, 136].

Often, the more complex multilayered NR structures possess different but similarly fascinating properties than the more-studied single-layer forms [9, 137]. For example, in the electronic domain, the three-layered graphene has an intriguing quantum Hall response different from that of the single- and bi-layer graphene [134]. In the mechanical domain, the weak vdW interlayer gluing makes multilayered nanostructures prone to a shear deformation mode [133] in which individual stiff layers glide against each other. It is *a priori* unclear if graphene and h-BN NRs would respond to mechanical deformation in a platelike manner, or if the layers tend to slide past each other. A detailed understanding of the consequences of this weak interlayer coupling on the primary mechanical deformation modes is important both for developing applications, and fundamentally, to investigate the validity limits of classical continuum mechanics.

In this Chapter, the bending behavior of graphene NRs (GNRs) and boron-nitride NRs (BNNRs) is inspected via direct bending experiments combined with microscopic simulations. The experimentation is enabled by novel capability to both synthesize NRs of each type and directly manipulate nanostructures *in situ* within a high-resolution TEM [135, 138]. It is demonstrated that both nanomaterials show remarkable resilience against mechanical manipulation. Rather than fracturing, they bend reversibly and form localized kinks. On the theoretical side, the mechanisms involved are revealed by atomistic simulations performed with objective molecular dynamics [40, 41]. Bending is, of course, an angular deformation, and therefore breaks translational symmetry, and is much more easily studied with OMD. Because kinking is caused by the severe compression of the inner layers, bending of both graphene and h-BN is platelike, with no layer sliding occurring.

6.2 Experiments

The NRs used in the experiments were picked up under high-resolution TEM (HRTEM) imaging of synthetic powders, which mostly contained the corresponding multiwalled nanotubes (MWNTs). The nanotubes (NTs) were produced at high yields using so-called boron oxide assisted chemical vapor deposition procedure (BN) and an arc-discharge technique (C). The NRs were by-products of the respective syntheses. The number of layers in the NRs used in the experiments ranged from 9 to 13. The mechanical tests reported here were performed inside a 300 kV high-resolution field emission TEM (JEM 3100FEF) equipped with a state-of-art STM-TEM sample holder (Nanofactory Instruments) with a piezotube driven manipulator. A chemically etched Wnanoprobe was mounted onto the manipulator to act as a movable probe that can be driven in 3D with nanometer precision under the piezotubes' drives. The NRs were attached to the edge of a counterpart Au wire, which was set onto the fixed terminal facing the W probe. Under TEM observations, individual NRs protruding from the Au wire edge were first selected, and their structure was entirely characterized using high-resolution TEM imaging. Under the control of the manipulator, the W nanoprobe was moved to contact with the free end of a NR.

Both materials exhibited localized kinking under bending, as shown for a 12-layer BNNR in Fig. 6.1(a) and a 9-layer GNR in Fig. 6.1(b). The bending process is fully reversible, with the NRs returning to a pristine straight state when unloaded. Very little deformation is required to initiate kinking. In the case of a very long and flexible NR, as the 9-layer 1 μm-long GNR seen in Fig. 6.1(b), a smooth-bending stage can be observed prior to kinking. The curvature range in which kinking initiates is in agreement with the computational predictions. The morphology of the kink area further emerges from the HRTEM image presented in Fig. 6.2, where the characteristic dark fringes indicate the wrinkling of the constituent layers. The atomistic details of the morphology leading to these fringes were uncovered in the simulations, Fig. 6.3(a).

6.3 Simulations

What is the underlying mechanism leading to kinking? When considering the pure bending of graphene and h-BN, two contrasting mechanisms are conceivable: platelike

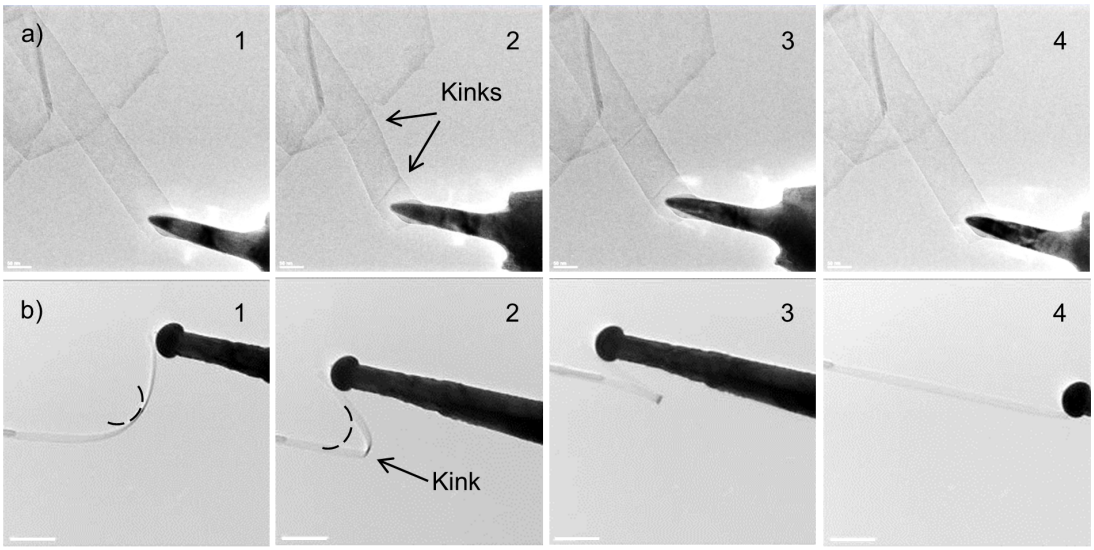

Figure 6.1: a) Bending (1), (2) and recovery (2), (3) cycle of 12-layer BNNR. Scale bars are 50 nm. Width is 82 nm, length is $\approx$ 300 nm. b) Bending (1)-(3) and recovery (4) cycle of 9-layer GNR, showing critical curvature for kinking predicted from simulations (dotted line). Scale bars are 200 nm. Width is 34 nm, length is $\approx$ 1 μm.

bending, where the layers bend collectively and do not slide relative to each other, or a mechanism where layer sliding occurs (Fig. 6.4. One can identify these mechanisms by simply bending a stack of paper. On one hand, in the platelike case there is an invariant neutral surface, on the opposite sides of which there is extension and compression of the constituent layers. On the other hand, bending accompanied by layer sliding efficiently releases these in-plane strains on both sides of the neutral surface. Only in the first case would the compression of the inner layers cause them to wrinkle and a kink to arise. Thus, the occurrence of kinking itself, as well as the layer wrinkling seen in Fig. 6.2, are indications that bending in graphene and h-BN commences in a platelike manner.

Relying on the above arguments, simulations of the bending process using objective MD were performed. The objective boundary conditions used here consisted of two operations – one pure translation and one pure angular rotation. In the context of the previously established nomenclature, the pure translation can be viewed as the helical operation h with the helical angle γ set to zero. Thus, the objective boundary conditions are (Fig. 6.5)

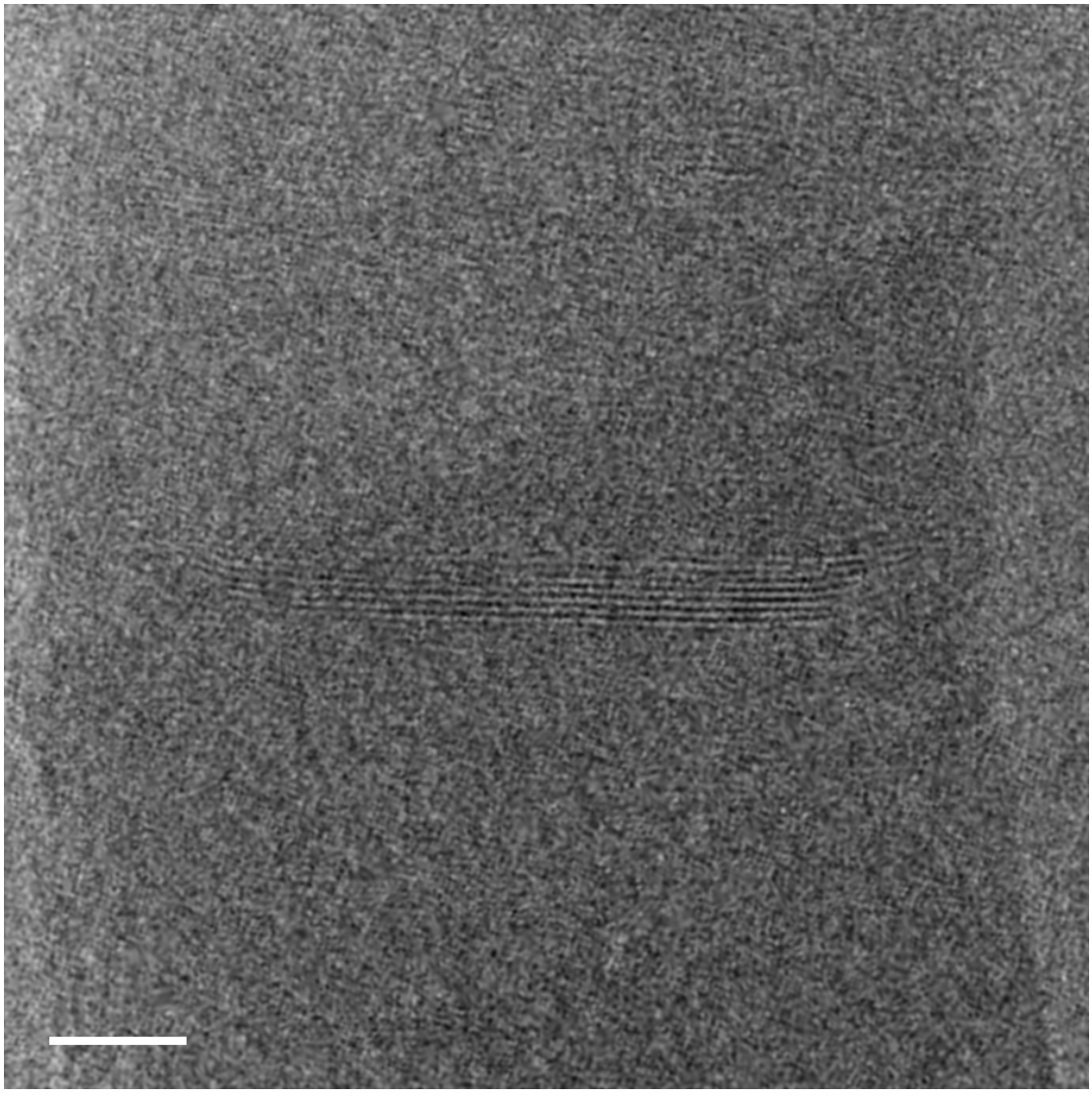

Figure 6.2: Kink developed in 9-layer GNR. This HRTEM image was taken towards the end of the bending stage [different experiment than Fig. 6.1(b)]. It shows typical dark fringes, the cause of which is shown in Fig. 6.3(a). Scale bar is 5 nm.

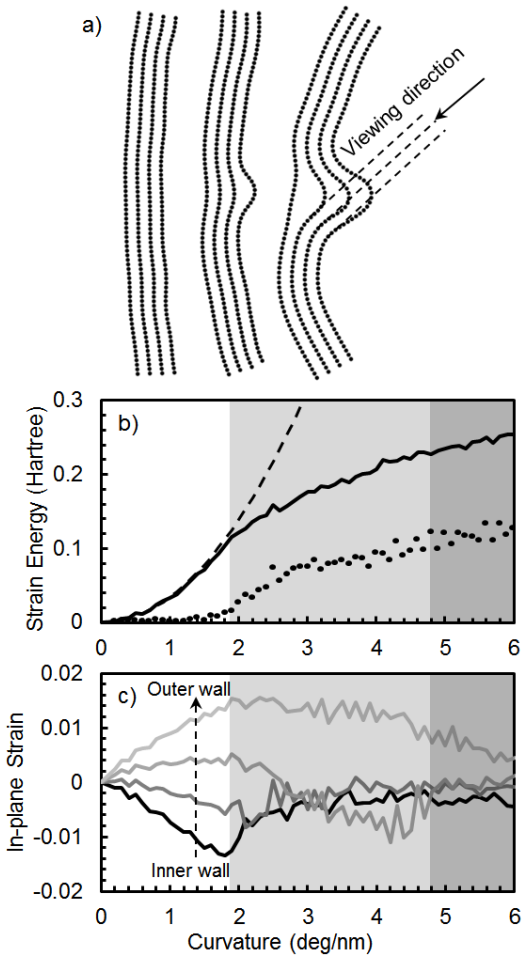

Figure 6.3: Objective MD simulations for the bending of 4-layer h-BN. Three stages are indicated–(i) ideal platelike (no layers wrinkled-unshaded on graphs), (ii) intermediate (some layers wrinkled-shaded light gray), and (iii) final (only outer layer not wrinkled-shaded dark gray). (a) Morphology, revealing the origin of the dark fringes seen in the TEM Fig. 6.2. (b) Energy-dashed line indicates plate behavior as described by Ref. [16], solid line indicates total bending energy, dotted line indicates interlayer vdW component. (c) In-plane strain in individual layers.

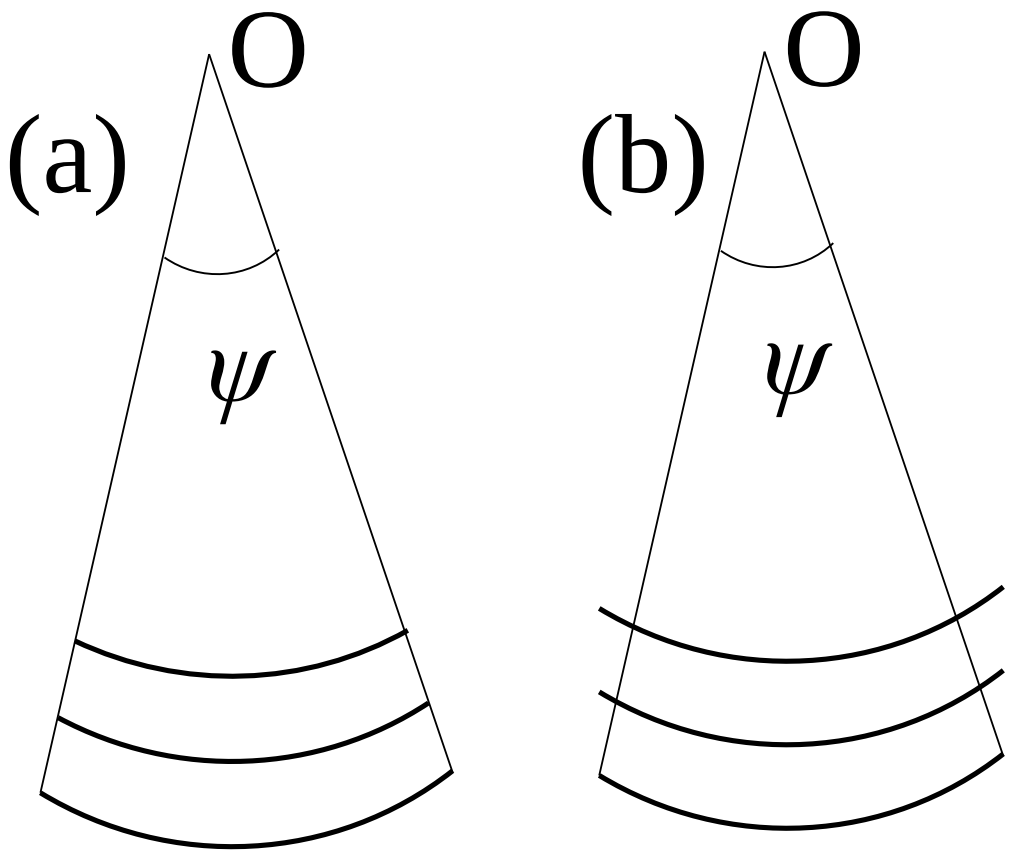

Figure 6.4: Demonstration of the two conceivable mechanisms of bending of layered materials. (a) Plate-like bending, where the layers do not slide with respect to each other, and (b) bending with layer sliding. The OMD boundary conditions implicitly assume case (a).

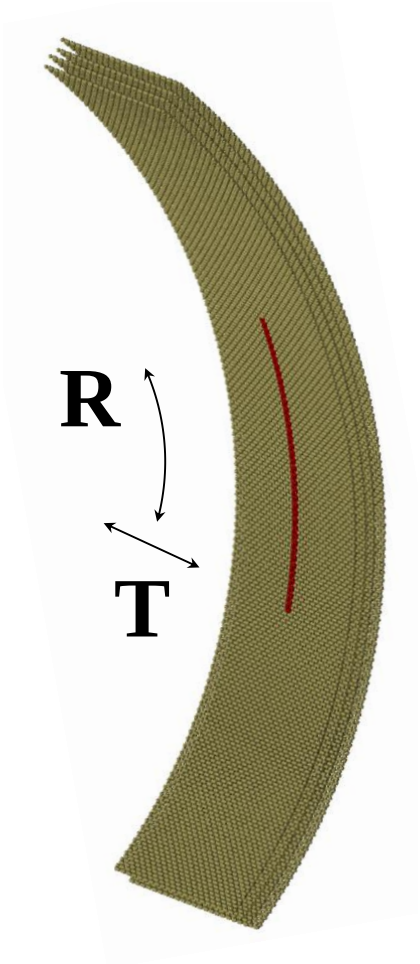

Figure 6.5: Objective boundary conditions employed in the multi-layer graphene and h-BN simulations

$$\mathbf{X}_{i,\zeta_h,\zeta_g} = \zeta_h \mathbf{T} + \mathbf{R}^{\zeta_g} \mathbf{X}_{i,0,0} \tag{6.1}$$

$$\mathbf{T} \equiv \begin{bmatrix} 0 \\ 0 \\ T \end{bmatrix}$$

$$\mathbf{R} \equiv \begin{bmatrix} \cos\psi & -\sin\psi & 0 \\ \sin\psi & \cos\psi & 0 \\ 0 & 0 & 1 \end{bmatrix}$$

Note that these boundary conditions implicitly constrains the system to platelike bending (Fig. 6.4, (a)) [16]. Because kinking is a localized mechanical phenomenon, large unit cells must be used in order to accurately represent the behavior of an isolated kink. Pure bending simulations of h-BN and graphene sections with a length of 10 nm in the bending direction were performed. Up to 10 layers were considered, with simulation cells containing between 320 and 1600 atoms. Despite not being able to use the minimum simulation cell possible from lattice symmetry, OMD is still highly advantageous in this case. The simulations represent imposing pure bending on the simulation cell, with no possibility of spurious boundary effects. The only constraint in the angular direction is the bending angle, and no total shear or in-plane strain is permitted – any in-plane strain is allowed to relax away under these boundary conditions. This is a significant advancement. Because the structure cannot be treated with PBC in the bending direction, formerly structures under bending were simulated by considering an isolated simulation cell with no boundary conditions. Bending was applied by fixing the end sections of the structure and rotating them. This meant that extra care had to be taken to avoid the aforementioned end effects – large simulation cells were needed in order to prevent the boundaries from affecting the behavior of the kink, and the fixed ends had to be moved in order to avoid shear and in-plane strain.

Only bending in the zigzag direction was considered, as graphene and h-BN in-plane behavior is nearly isotropic at low strains [139, 140, 52]. The synthesized NRs have widths of tens of nanometers, or hundreds of atomic distances, and the experimental load is applied directly along the length, so the finite width of the NRs should have little effect. Thus, although the simulations represent an infinite plate, they can be

accurately applied to the NR experiments. Various degrees of bending were applied to the simulation cell by varying the curvature in steps of at most 1 deg =nm of tube length. In order to prevent the simulation from getting trapped in metastable states, MD was performed to randomize the configuration at each step, followed by energy minimization. This protocol has previously been successful in simulating bending of nanotubes [60] and, indeed, the energy graphs [Fig. 6.3(b)] show that the transition between smoothly bent and kinked states does not show any energy discontinuity-the simulation relaxes to the lowest energy configuration. The covalent interatomic interactions within the layers were described here with the Tersoff potential [141], a many-body potential widely used for studying deformations of graphitic structures. For BN the parameters of Verma et al. [142] are used. The long-range interlayer interactions were accounted for with a standard Lennard-Jones potential. The parameters for graphene (ϵ = 2.39 meV, σ = 3.41 Å) were the well-proven parameters of Girifalco et al. [142], while the parameters for h-BN (ϵ = 5.0 meV, σ = 3.35 Å) were fitted to match the interlayer spacing and binding energy obtained from the recent dispersion-corrected density-functional theory calculations of Maromet et al. [136] For a detailed description of these interatomic potentials, see Appendix E. Note that the interlayer binding in BN is approximately twice as strong as in graphene.

Figure 6.3 shows the (a) morphologies, (b) energetics, and (c) the individual layers' in-plane strain, characteristic of *all* the bending simulations, using the example of 4-layer h-BN. The bending strain energy is displayed, as well as the interlayer vdW energy component. The in-plane strain was defined as the fractional difference between the deformed and original length of each layer in the bending direction. Bending of NRs is characterized by three stages. (i) At first the bending is smooth in all layers [Fig. 6.3(a), left), and the strain energy closely follows the finite-size-corrected plate model of Zhang *et al.* [16], using the in-plane Young's modulus of the appropriate set of Tersoff potential [Fig. 6.3(b)]. The energy depends quadratically on the curvature and the coefficient scales as the cube of the number of layers, N^3. This strain energy is due to the compression of the inner layers and the elongation of outer layers [Fig. 6.3(c)], i.e., platelike behavior. The vdW component of the strain energy is negligible during the smoothbending stage. (ii) At the critical curvature κ_{cr}, the inner layer wrinkles [Fig. 6.3(a), middle). The vdW component becomes non-negligible due to the layer

spacing becoming nonoptimal at the kink, and the total strain energy begins to fall off from the plate model [Fig. 6.3(b)]. (iii) As the curvature increases, the wrinkling propagates to inner layers until only the outermost layer is not wrinkled [Fig. 6.3(a), right). From Fig. 6.3(c) it can be seen that after each layer kinks, it quickly returns to its undeformed length, releasing *all* compressive strain. This behavior is in agreement with previous literature on wrinkling of layered structures [144]. The tensile strain in the outer layers, meanwhile, is released by the movement of the entire simulation cell towards the rotation axis, slightly increasing the curvature.

6.4 Analysis

The simulation results are in good agreement in all important respects with the experimental behavior, indicating that the above microscopic picture may be used to predict the kinking behavior of NRs. Broadly, the prediction is that both graphene and h-BN should demonstrate kinking at very small deformations, as seen in the experiments. The kinking morphology seen in the simulations is consistent with the dark fringes seen in HRTEM images of kinks, while the lack of bond breaking in the simulations is consistent with the reversibility of the bending in the experiments. The experiment shown in Fig. 6.1(b) lends itself to direct quantitative comparison to the simulations because a smooth-bending stage can be observed before kinking. Additionally, the length and flexibility of this GNR means that the deformation is nearly pure bending.

The dependence of the critical curvature for kinking κ_{cr} on the number of layers n_L is now given. As simulations suggest, the compression of the inner layer is the key cause of kinking. This suggests assumption that kinking begins at a fixed material-specific critical stress σ_{cr} in the innermost layer. In the simplified Euler-Bernoulli case, the in-plane stress at distance d from the neutral axis is $\sigma_{cr} \propto \kappa_{cr} d$. For the most inner layer $d \propto n_L - 1$, thus

$$\kappa_{cr} = \frac{B}{n_L - 1}, \tag{6.2}$$

where B is a proportionality constant. Note that this simplified model precludes any length dependence. Essentially, the assumption is being made that the simulation cell chosen is long enough in the angular direction for the kink to be truly isolated.

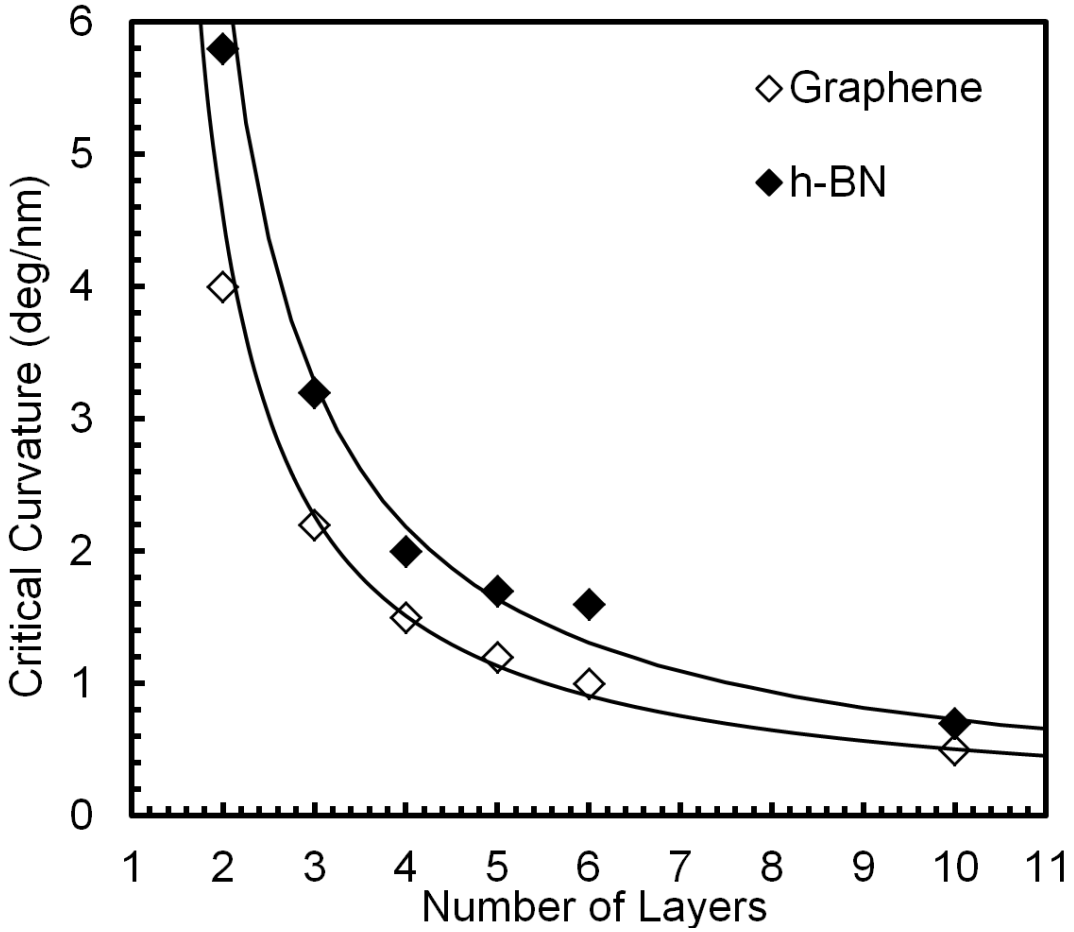

Figure 6.6: Critical curvatures for kinking. Continuous lines show fitting with Eq. 6.2 using $B = 6.6$ and 4.53 deg/nm for graphene and h-BN, respectively.

To verify this, a full range of simulations on graphene was performed using 5 nm-long simulation cells. Indeed, reducing the length by a factor of 2 caused only a 10% increase in critical curvature, showing that the length dependence is secondary. Figure 6.6 displays the critical curvature found from each of the simulations as well as the fitting of Eq. 6.2, using $B = 6.6$ and 4.5 deg/nm, for BN and graphene, respectively, meaning that graphene kinks $\approx 150\%$ earlier. The differences in the elastic properties of the h-BN and graphene monolayers are too small to account for this. Thus, this dissimilarity in B is largely due to the stronger interlayer binding in h-BN – it is more energetically expensive to disturb the perfect interlayer spacing by creating a wrinkle in h-BN than it is in graphene. The dotted lines in Fig. 6.1(b) show the critical curvature as predicted by Eq. 6.2, allowing a test of its validity. The curvature range in which the GNR kinks agrees with this prediction.

It is instructive to compare these results with the behavior of NTs under bending. Unlike multilayered NRs, MWNTs with closed cores feature complex competing forces when they bend. While the compression of the inner side of the bend still drives localized bending of the walls, the core of the NT provides support and prevents deep kinks from forming. Because of this, MWNTs tend to form distributed ripples at intermediate curvatures [60, 144]. Additionally, in MWNTs, there is circumferential stress arising from these competing forces, while in multilayered NRs, there is no in-plane stress perpendicular to the bending direction [144]. Conceptually, the bending of single-wall NTs (SWNTs) and MWNTs with open cores is closer to the bending of NRs. The lack of support from a closed core causes a localized kink to form under bending, similar to NRs [60, 145]. However, the circumferential connection between the inner and outer bending surface still plays a role. Because of this, both MWNTs and SWNTs show a $\kappa_{cr} \propto 1/R^2$ dependence of the critical curvature κ_{cr} on the tube radius R, in contrast to the $\kappa_{cr} \propto 1/T$ dependence on the thickness T observed here in NRs [60, 145].

6.5 Conclusion

In summary, direct bending experiments show that BNNRs and GNRs tend to bend reversibly by forming a localized kink, caused by the wrinkling of individual layers. The kinking behavior observed is universal despite the much more complex interlayer binding

in h-BN compared to graphene [110, 136]. Simulations reveal the atomistic details of bending, which is smooth and platelike at low curvatures, followed by kinking, the morphology and mechanics of which are in agreement with the experiments. Kinking occurs at lower curvatures for graphene than h-BN due to the stronger interlayer binding in the latter material. By examining the atomistic details of kinking, a simple model to predict the critical curvature at which kinking begins in experiment was proposed. The kinking behavior of the NRs was found to be significantly different from that of MW-and SWNTs. The proposed model can be used to predict the behavior of graphene and h-BN nanoribbons and nanosheets under bending in future experiments, as well as aid in the design of nanomechanical devices. The common bending behavior revealed here likely extends to even more complex layered materials of current interest, such as MoS_2 [146].

Chapter 7

Heat Current in Objective Structures: Preliminary Work

7.1 Introduction

The Green-Kubo method allows for calculation of the thermal conductivity of a system from equilibrium molecular dynamics. The theoretical expression for the Cartesian component pq of the anisotropic thermal conductivity tensor κ_{pq} is [147]

$$\kappa_{pq} = \frac{1}{Vk_BT^2}\int_0^\infty \langle J_p(\tau)J_q(0)\rangle d\tau. \tag{7.1}$$

Here, τ is some time during the simulation, V is the system volume, k_B is the Boltzmann constant, T is the system temperature (which is a constant if the system is in equilibrium), J_p and J_q are Cartesian components of the instantaneous time-dependent heat current vector $\mathbf{J}$, and the angle brackets indicate the ensemble average, which is equivalent to the time average under the ergodic hypothesis at the basis of molecular dynamics. The version of the equation that discretizes the integration for molecular dynamics simulations is

$$\kappa_{pq} = \frac{\Delta t}{Vk_BT^2}\sum_{m=1}^{M}(N-m)^{-1}\sum_{n=1}^{N-m} J_p(m+n)J_q(n). \tag{7.2}$$

Here, Δt is the timestep length and M is the total number of timesteps corresponding to the upper limit of the integral in Eq. 7.1. The index m corresponds to the integration

proceeding along time, $\tau \Leftrightarrow m\Delta t$. N is the total number of timesteps in the simulation. $N > M$, because a time average must be taken. The second summation represents a statistical average over time, with $N - m$ samples being taken of the correlation $J_p(\tau)J_q(0)$, each shifted in time. In each sample, $J_q(n)$ corresponds to $J_q(0)$ from Eq. 7.1, and $J_p(m + n)$ corresponds to $J_p(\tau)$. Also, of course, M is finite unlike the integral in Eq. 7.1. The integrand decays to zero with increasing time, so a long enough MD simulation should give the correct time. Alternatively, various strategies have been proposed for estimating the $t \to \infty$ behavior of the correlation based on shorter simulation times [148, 149].

7.2 Heat Current Expressions

This chapter is focused on the calculation of the microscopic heat current $\mathbf{J}$. The fundamental definition is [147]

$$\mathbf{J} = \frac{d}{dt} \sum_i \mathbf{X}_i(t)\epsilon_i(t). \tag{7.3}$$

Here, the sum runs over all atoms in a system and $\epsilon_i = m_i v_i^2/2 + E_i$ is the total energy of atom i, the sum of its kinetic energy $m_i v_i^2/2$ and potential energy E_i associated with that atom. Consider a system that is governed by a pair potential, so that $E = \frac{1}{2}\sum_i \sum_{j\neq i} E_{pair}(X_{ij})$, where the *only* dependence that E_{pair} has is on the distance between atoms i and j, X_{ij}. Then, the potential energy of atom i is straightforward to define, $E_i = \frac{1}{2}\sum_{j\neq i} E_{pair}(X_{ij})$. It can then be shown that[147]

$$\mathbf{J} = \sum_i \epsilon_i \mathbf{v}_i + \frac{1}{2}\sum_{j\neq i} \mathbf{X}_{ij}(\mathbf{f}_{ij} \cdot \mathbf{v}_i). \tag{7.4}$$

Here, $\mathbf{v}_i$ is the velocity of atom i, $\mathbf{X}_{ij}$ is the vector distance between atom i and atom j and $\mathbf{f}_{ij}$ is the force on atom i due to its pair interaction with atom j. Call this the *force formulation*. Another possible expression for $\mathbf{J}$ is[150].

$$\mathbf{J} = \sum_i (\epsilon_i \mathbf{v}_i - \mathbf{S}_i \mathbf{v}_i). \tag{7.5}$$

Here, $\mathbf{S}_i$ is the per-atom 3×3 static stress tensor for atom i. Component pq of the per-atom static stress tensor is one-half of the Cartesian component p of the force on

atom i due to neighbor n multiplied by the Cartesian component q of the interatomic vector $\mathbf{X}_{in}$, summed over all neighbors n. Call this the *stress formulation*. This is the formulation used in the highly popular LAMMPS computation package[151].

7.3 Implementation of Heat Current in Trocadero

In this chapter, heat current calculation is implemented for the Lennard-Jones potential (Appendix E.2) in the Trocadero computational package.[56] In Trocadero, the evaluation of the energy and the forces is decoupled from the time evolution. Thus, the stress formulation is chosen – it is more convenient to compute the atomic stress tensors and pass them to the time-evolution subroutine, than to store the pairwise forces and compute the double sum in Eq. 7.4.

For the Lennard-Jones potential, the internal potential energy of atom i is

$$E_i = \frac{1}{2}\sum_n \left(\frac{a}{X_{in}^{12}} - \frac{b}{X_{in}^{6}} \right). \tag{7.6}$$

The sum runs over all neighbors n of atom i that are within the cutoff range of the potential, both within the unit cell and its objective images. X_{in} is the distance between atom i and neighbor n. The Cartesian component pq of the per-atom stress tensor is

$$[\mathbf{S}_i]_{pq} = [\mathbf{S}_i]_{qp} = \frac{1}{2}\sum_n \left(-\frac{12a}{r_{in}^{14}} + \frac{6b}{r_{in}^{8}} \right) [\mathbf{X}_{in}]_p [\mathbf{X}_{in}]_q. \tag{7.7}$$

There is a computational caveat associated with implementing Eq. 7.7 with objective boundary conditions, similar to the rotation of the forces described in Sec. 2.3. The neighbor n is some atom j in the unit cell, or an image of atom j. To increase computational efficiency, the summand in Eq. 7.7 is evaluated only if $j \geq i$. In order to get the correct values of $\mathbf{S}$, then, the summand is accumulated to $\mathbf{S}_j$ as well as $\mathbf{S}_i$. However, if n is an image of j, the summand must be transformed before being accumulated to $\mathbf{S}_j$ – $\mathbf{S}$ is a rank 2 tensor and transforms as such. If $\mathbf{S}^*$ is the summand in Eq. 7.7, and neighbor n of atom i is an image of atom j that is rotated by angle θ, then the quantity accumulated to $\mathbf{S}_j$ is $\mathbf{R}_\theta^T \mathbf{S}^* \mathbf{R}_\theta$, where $\mathbf{R}_\theta$ is a standard rotation matrix.

Once the energy calculation is complete and E_i and $\mathbf{S}_i$ are obtained, the calculation of $\mathbf{J}$ is completed during the process of progessing to the next timestep of the

molecular dynamics simulation. The standard velocity Verlet molecular dynamics integration algorithm calculates the velocity $\mathbf{v}_i$, and the kinetic per-atom energy $m_i v_i^2$. This accounts for all the quantities required in Eq. 7.5. **J** can then be output for post-processing in order to obtain the thermal conductivity using the Green-Kubo formula. This implementation has been carried out in Trocadero for both PBC and OMD.

7.4 Testing of Implementation

In order to verify the implementation, several simulations were carried out on an "Argon nanowire" – a test system. Its physical properties are not of interest. Indeed, the simulations are being carried out at a temperature of 300 K, much higher than the boiling point of argon. Even that is irrelevant, as the simulations are only evolved for 10 timesteps of 2 fs. What is important is that the simulations are fully deterministic – starting with equivalent initial conditions, the time evolution of the heat flux should be identical regardless of the boundary conditions. The first test is a structure with helical-angular boundary conditions. As usual,

$$\mathbf{X}_{i,\zeta_h,\zeta_g} = \zeta_h \mathbf{T} + \mathbf{R}_\gamma{}^{\zeta_h} \mathbf{R}_\psi{}^{\zeta_g} \mathbf{X}_{i,0,0} \tag{7.8}$$

$$\mathbf{T} \equiv \begin{bmatrix} 0 \\ 0 \\ T \end{bmatrix}$$

$$\mathbf{R}_\gamma \equiv \begin{bmatrix} \cos\gamma & -\sin\gamma & 0 \\ \sin\gamma & \cos\gamma & 0 \\ 0 & 0 & 1 \end{bmatrix}$$

$$\mathbf{R}_\psi \equiv \begin{bmatrix} \cos\psi & -\sin\psi & 0 \\ \sin\psi & \cos\psi & 0 \\ 0 & 0 & 1 \end{bmatrix}.$$

Here, $\gamma = 1^\circ$ and $\psi = 24^\circ$, and the objective simulation cell contains 6 atoms (Fig. 7.1 (a), highlighted in maroon). Thus, to create the PBC simulation cell for this structure, the OMD cell must be rotated 15 times, and then the helical operation must be appied 24 times in order to regain the translational symmetry (a full 360° turn is

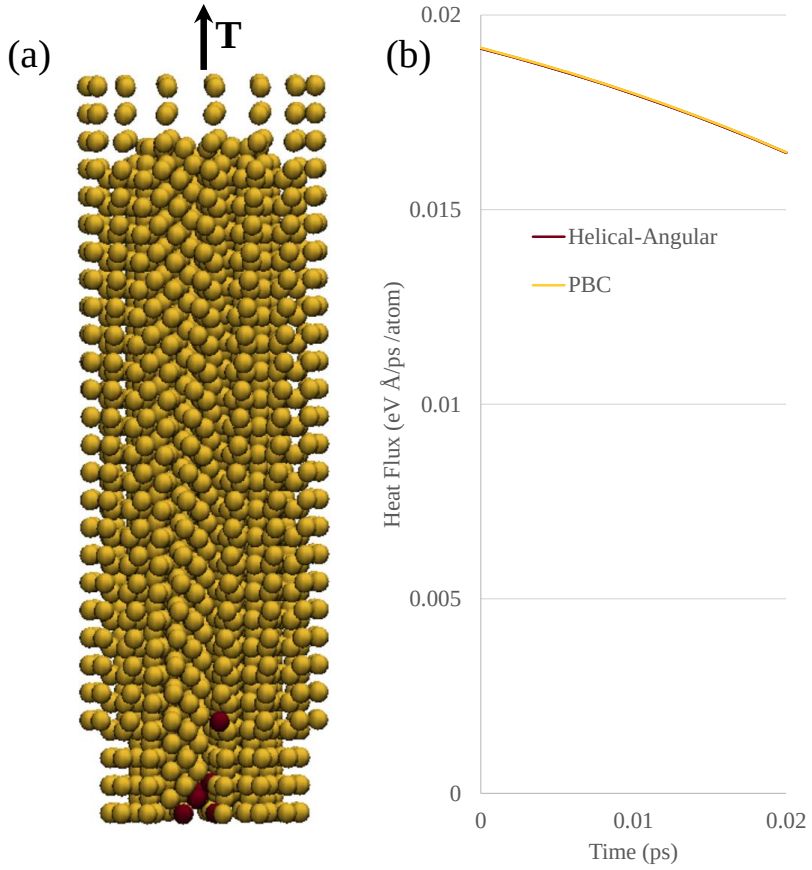

Figure 7.1: (a) PBC cell of "argon nanowire" used for test computations of heat current. Highlighted in maroon are the six atoms comprising the helical-angular simulation cell. (b) Time evolution of heat current along the wire axis, normalized by the number of atoms, for both sets of boundary conditions.

not needed, as the helical angle need only match the rotational symmetry angle), so the PBC cell contains $6 \times 15 \times 24 = 2160$ atoms (entire structue pictured in Fig. 7.1 (a)). With these two simulation cells, a short MD run was prformed with identical initial velocities (appropriately rotated for atoms in the PBC cell). The heat current along the "wire" axis is shown in Fig. 7.1 (b), normalized by the number of atoms. The graph confirms that the two simulations produce identical results, and the implementation is working in an internally consistent way.

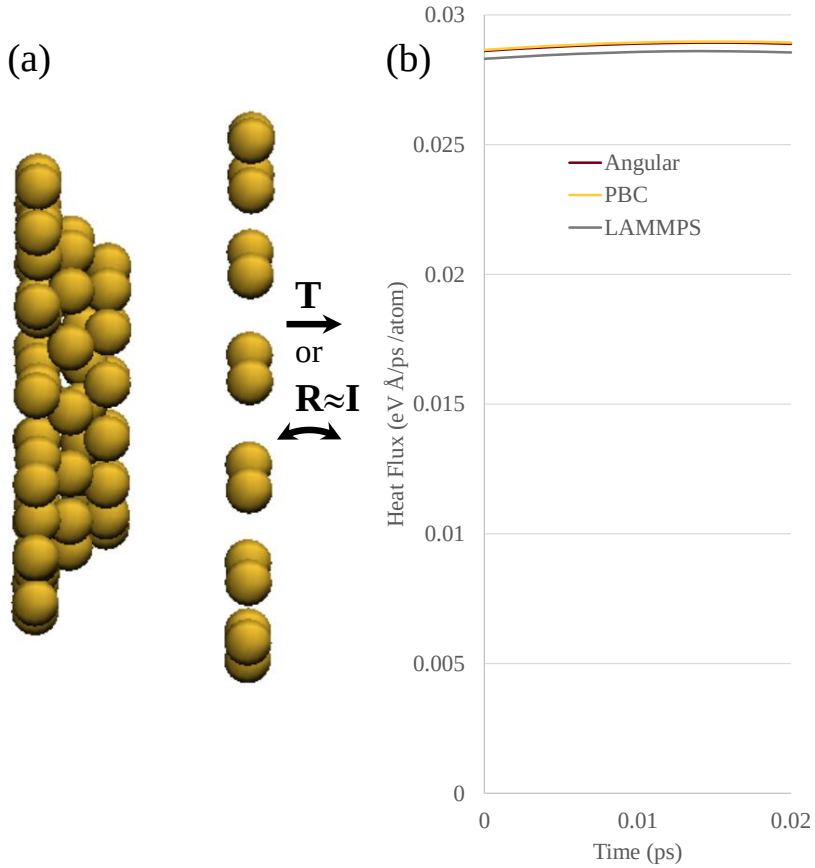

Figure 7.2: (a) Cell of "argon nanowire" used for PBC and angular-only objective test computations of heat current. (b) Time evolution of heat current along the wire axis, normalized by the number of atoms, for both sets of boundary conditions, as well as an analogous PBC computation with LAMMPS

These calculations, however, do not indicate anything about the heat current in the angular direction. There is no fully direct way to compare this to PBC. However, when bending is applied using OMD (for example, as it was in Chapter 6, except here no secondary translational operation is used), it should behave in a continuous manner. So, bending is appied to a 90-atom cell of an argon nanowire (same structure as before, except without the axial twist of 1°) (Fig. 7.2 (a)):

$$\mathbf{X}_{i,\zeta} = \mathbf{R}^{\zeta}\mathbf{X}_{i,0} \tag{7.9}$$
$$\mathbf{R} \equiv \begin{bmatrix} \cos\psi & -\sin\psi & 0 \\ \sin\psi & \cos\psi & 0 \\ 0 & 0 & 1 \end{bmatrix}.$$

If $\psi \to 0$ (and the coordinates $\mathbf{X}_{i,0}$ are offset from the origin appropriately in order to avoid axial strain), the time evolution should be approximately the same as that when PBC is used with the analogous same simulation cell. Here, $\psi = 0.1°$. As shown in Fig. 7.2 (b), the two types of boundary conditions agree with each other well. Additionally, Fig. 7.2 (b) shows an analogous PBC simulation carried out with LAMMPS. The results are very close to the Trocadero results. It may seem worrying that the Trocadero PBC and OMD results are closer to each other than the Trocadero PBC results and the LAMMPS PBC results, but the total difference between the latter is only about 1%. A small variation is to be expected, as there are minute differences in the simulation methods. For example, the Lennard-Jones potential is cut off at the same distance in both codes. However, in Trocadero, the pairwise energy is shifted in order to avoid a discontinuity at the cutoff. The LAMMPS simulations were carried out without this shift. Other differences may exist as well.

7.5 Conclusion and Future Work

In conclusion, heat current calculations have been implemented into the Trocadero simulation package using both PBC and OMD for the Lennard-Jones interatomic potential. The implementation was shown to be consistent both internally and with the well-proven LAMMPS simulation package. However, the truly interesting nanomaterials –

carbon, silicon, and others – with thermal applications require multi-body potentials to be treated, such as the Tersoff potential [31](Appendix E.1).

Moving from a two-body to a multi-body potential is a tremendous increase in complexity. Equations 7.5 and 7.4 still hold in some form, but only abstractly. Many question are raised and this is an area of intense study and debate [147, 148, 149]. In a many-body potential, what is the meaning of E_i, the potential energy associated with atom i? What is the "force on atom i due to atom j"? A given atom will enter many terms in the overall energy sum, affecting E_i for many different atoms i. On one hand, it is sensible to divide each many-body interaction into equal parts among the atoms involved[147]. On the other hand, this is difficult or perhaps impossible for some cases – in the Tersoff potential, the three-body terms are raised to a power after being added together, so the potential cannot be split into linearly superimposable three-body terms (Eq. E.4). Some works [147] state that the specific partitioning is irrelevant, including specifically for the Tersoff potential [148]. Because of the Tersoff potential's "superficially two-body" form (Eq. E.1), when it comes to implementation, it is clearly simpler to split the energies between atoms i and j, and assign no energy to atom k [148]. However, no rigorous justification for the choice of energy splitting is provided, only comparisons between results or philosophical arguments. Additionally, as it was explained, it is favorable to use the stress formulation. Unfortunately, the works that use the convenient pairwise energy splitting all use the force formulation. The stress formulation, as described in Ref. [150], uses an equal splitting between multi-body terms, and concerns a molecular mechanics potential for water where such a splitting is reasonably possible. This is the implementation that is used in LAMMPS. It is unclear if a stress formulation that uses the convenient pair-wise energy splitting and gives accurate results can be implemented for the Tersoff potential. Thus, a significant amount of research, development, and testing must be done before heat current calculations can be carried out for the Tersoff potential under OMD.

Chapter 8

Conclusion

In summary, objective molecular dynamics was used to enable or facilitate computational investigations of practical interest – electromechanical properties of screw-dislocated silicon nanowires, bending of a graphene monolayer and kinking of graphene and boron nitride nanoribbons. The results of these investigations have broad implications. For screw-dislocated silicon nanowires, the validity of Eshelby's continuum theory of dislocations at the nanoscale, when supplemented by an empirical core energy term, was confirmed, and the core energy term was calculated. Screw dislocations were revealed as a method of tuning the band-gap of silicon nanowires. Bending of graphene was analyzed in terms of a simple molecular orbital picture, demonstrating that π-orbital misalignment is the dominant source of bending strain energy. A far-reaching qualitative analysis of the behavior of empirical atomistic and continuum models of graphene was carried out, and their degree of validity for studying bending of graphene was presented. Atomistic simulations revealed the underlying mechanism behind the kinking seen in bending experiments of graphene and hexagonal boron-nitride nanoribbons, and a simple method of predicting critical curvature for the onset of kinking was presented.

The capabilities of objective molecular dynamics were extended to allow new types of simulations to be carried out. The venerable Ewald summation formula for electrostatic and dispersion interactions was generalized to helical symmetry, allowing self-consistent charge density functional-based tight-binding (SCC-DFTB) simulations to be carried out using objective boundary conditions for the first time. SCC-DFTB is a highly

accurate, yet computationally efficient method of simulating heteronuclear materials. Proof-of-concept simulations were carried out on a screw-dislocated zinc oxide nanowire, a boron nitride nanotube, and a DNA single helix. Preliminary work on implementing heat current calculations into objective molecular dynamics is presented, in the form of a successful impementation for the Lennard-Jones potential. Implementation for the Tersoff potential is proposed, and the challenges and considerations involved are discussed. Heat current calculations enable calculation of thermal conductivity. Successful coupling of heat current calculations with objective molecular dynamics would mean that, for the first time, the effect of deformations such as torsion and bending, and of defects such as screw dislocations on thermal conductivity will be able to be quantified.

The applications and developments of objective molecular dynamics presented herein suggest a multitude of new avenues of study, besides the obvious further development of heat current calculations. SCC-DFTB can enable highly accurate simulations analogous to those carried out in Chapters 3 and 4 – for example, methodical studies of screw-dislocated zinc oxide nanowires using SCC to augment previous non-SCC studies, or studies of ideal bending of layered materials other than graphene, such as hexagonal boron nitride, or molybdenum disulfide. Molybdenum disulfide and similar materials present an especially interesting opportunity – they are layered, but each layer has finite thickness, so plate approximations may be more viable, and the molecular orbital picture of bending would be vastly different from graphene. The simulations in Chapter 6 were carried out using the classical Tersoff potential. While time-consuming because of the large number of atoms, DFTB calculations should be feasible for kinking of graphene and boron-nitride nanoribbons. In general, DFTB would provide a more accurate description of interlayer registry effects, and SCC-DFTB would allow for a more accurate description of the partially ionic bonding in boron-nitride. Perhaps the most exciting prospect is the possibility of simulating biomolecules, such as DNA or amyloid fibrils. Biomolecules are traditionally simulated with molecular force-fields and the methodology is separate from that used to study solid-state materials. However, many biomolecules are a prominent example of objective structures. In fact, the very idea of objective structures arose from biomolecules[40]. Now that SCC-DFTB has been implemented with objective boundary conditions, in combination with dispersion, it will be possible to accurately simulate biomolecules with an explicitly quantum mechanical

method.

References

[1] W. Humphrey, A. Dalke, and K. Schulten, VMD - Visual Molecular Dynamics, *J. Molec. Graphics* **14**, 33 (1996).

[2] I. Nikiforov, D.-M. Tang, X. Wei, T. Dumitrică, and D. Golberg, Nanoscale Bending of Multilayered Boron Nitride and Graphene Ribbons: Experiment and Objective Molecular Dynamics Calculations, *Phys. Rev. Lett.* **109**, 025504 (2012).

[3] I. Nikiforov, E. Dontsova, R. D. James, and T. Dumitrică, Tight-Binding Theory of Graphene Bending, *Phys. Rev. B* **89**, 155437 (2014).

[4] R. A. Evarestov, M. I. Petrashen, and E. M. Ledovskaya, The Translational Symmetry in the Molecular Models of Solids, *Phys. Stat. Sol. (b)* **68**, 453 (1975).

[5] W. M. C. Foulkes, and R. Haydock, Tight-Binding Models and Density-Functional Theory, *Phys. Rev. B* **39**, 12520 (1989).

[6] A. Carlson, An Extended Tight-Binding Approach for Modeling Supramolecular Interactions of Carbon Nanotubes, Master's thesis, University of Minnesota, Minneapolis, MN 2010.

[7] R. Shankar, *Principes of Quantum Mechanics* (Springer Science+Business Media, LLC., New York, 1994), 2nd Ed.

[8] D.-B. Zhang, Electromechanical Characterization of Quasi-One Dimensional Nanostructures of Silicon, Carbon, and Molybdenum Disuldfide via Symmetry-Adapted Tight-Binding Molecular Dynamics, Doctoral dissertation, University of Minnesota, Minneapolis, MN 2010.

[9] K. S. Novoselov, A. K. Geim, S. V. Morozov, D. Jiang, Y. Zhang, S. V. Dubonos, I. V. Grigorieva, and A. A. Firsov, Electric Field Effect in Atomically Thin Carbon Films, *Science* **306**, 666 (2004).

[10] N. Lindahl, D. Midtvedt, J. Svensson, O. A. Nerushev, N. Lindvall, A. Isacsson, and E. E. B. Campbell, Determination of the Bending Rigidity of Graphene via Electrostatic Actuation of Buckled Membranes, *Nano Lett.* **12**, 3526 (2012).

[11] L. Tapasztó, T. Dumitrică, S. J. Kim, P. Nemes-Incze, C. Hwang, and L. P. Biró, Breakdown of Continuum Mechanics for Nanometre-Wavelength Rippling of Graphene, *Nature Phys.* **8**, 739 (2012).

[12] S. M. Kim, E. B. Song, S. Lee, J. Zhu, D. H. Seo, M. Mecklenburg, S. Seo, and K. L. Wang, Transparent and Flexible Graphene Charge-Trap Memory, *ACS Nano,* **6** 7879 (2012).

[13] X. Shi, B. M. Peng, N. M. Pugno, and H. Gao, Stretch-Induced Softening of Bending Rigidity in Graphene, *Appl. Phys. Lett.* **100**, 191913 (2012).

[14] Q. Lu, M. Arroyo, and R. Huang, Elastic Bending Modulus of Monolayer Graphene, *J. Phys. D: Appl. Phys.* **42**, 102002 (2009).

[15] Y. Huang, J. Wu, and K. C. Hwang, Thickness of Graphene and Single-Wall Carbon Nanotubes, *Phys. Rev. B* **74**, 245413 (2006).

[16] D.-B. Zhang, E. Akatyeva, and T. Dumitrică, Bending Ultrathin Graphene at the Margins of Continuum Mechanics, *Phys. Rev. Lett.* **106**, 255503 (2011).

[17] M. A. Hartmann, M. Todt, F. G. Rammerstorfer, F. D. Fischer, and O. Paris, Elastic Properties of Graphene Obtained by Computational Mechanical Tests, *EPL* **103** 68004 (2013).

[18] B. Hajgató, S. Güryel, Y. Dauphin, J. M. Blairon, H. E. Miltner, G. van Lier, F. de Proft, and P. Geerlings, Theoretical Investigation of the Intrinsic Mechanical Properties of Single- and Double-Layer Graphene, *J. Phys. Chem. C* **116**, 22608 (2012).

[19] Y. Wei, B. Wang, J. Wu, R. Yang, and M. L. Dunn, Bending Rigidity and Gaussian Bending Stiffness of Single-Layered Graphene, *Nano Lett.* **13**, 26 (2013).

[20] A. A. P. Sanjuan, Z. Wang, H. P. Imani, M. Vanevic, and S. Barraza-Lopez, Graphene's Morphology and Electronic Properties from Discrete Differential Geometry, *Phys. Rev. B.* **89** 121403(R) (2014).

[21] D.H. Robertson, D.W. Brenner, J.W. Mintmire, Energetics of Nanoscale Graphitic Tubules, *Phys. Rev. B* **45**, 12592 (1992).

[22] S. Iijima, Helical Microtubules of Graphitic Carbon, *Nature* **354**, 56 (1991).

[23] S. Iijima and T. Ichihashi, Single-shell Carbon Nanotubes of 1-nm Diameter, *Nature* **363**, 603 (1993).

[24] B. I. Yakobson, C. J. Brabec, and J. Bernholc, Nanomechanics of Carbon Tubes: Instabilities Beyond Linear Response, *Phys. Rev. Lett.* **76**, 2511 (1996).

[25] O. A. Shenderova, V. V. Zhirnov, and D. W. Brenner, Carbon Nanostructures, *Crit. Rev. Solid State Mater. Sci.* **27**, 227 (2002).

[26] C. Ru, Effective Bending Stiffness of Carbon Nanotubes, *Phys. Rev. B* **62**, 9973 (2000).

[27] V. Popov, V. V. Doren, and M. Balkanski, Elastic Properties of Single-Walled Carbon Nanotubes, *Phys. Rev. B* **61**, 3078 (2000).

[28] C. Y. Wang and L. C. Zhang, A Critical Assessment of the Elastic Properties and Effective Wall Thickness of Single-Walled Carbon Nanotubes, *Nanotechnol.* **19** 075705 (2008).

[29] M. Arroyo and T. Belytschko, Finite Crystal Elasticity of Carbon Nanotubes Based on the Exponential Cauchy-Born Rule, *Phys. Rev. B* **69**, 115415 (2004).

[30] J. Atalaya, A. Isacsson, and J. M. Kinaret, Continuum Elastic Modeling of Graphene Resonators, *Nano Lett.* **8**, 4196 (2008).

[31] J. Tersoff, New Empirical Approach for the Structure and Energy of Covalent Systems, *Phys. Rev. B* **37**, 6991 (1988).

[32] J. Tersoff, Empirical Interatomic Potential for Carbon, with Applications to Amorphous Carbon, *Phys. Rev. Lett.* **61**, 2879 (1988).

[33] D. W. Brenner, Empirical Potential for Hydrocarbons for Use in Simulating the Chemical Vapor Deposition of Diamond Films, *Phys. Rev. B* **42**, 9458 (1990).

[34] D. W. Brenner, O. A. Shenderova, J. A. Harrison, S. J. Stuart, B. Ni, and S. B. Sinnott, A Second-Generation Reactive Empirical Bond Order (REBO) Potential Energy Expression for Hydrocarbons, *J. Phys.:Condens. Matter* **14**, 783 (2002).

[35] S. Niyogi, M. A. Hammond, H. Hu, B. Zhao, P. Bhowmik, R. Sen, M. E. Itkis, and R. C. Haddon, Chemistry of Single-Walled Carbon Nanotubes, *Acc. Chem. Res.* **35**, 1105 (2002).

[36] T. Dumitrică, C. M. Landis, and B. I. Yakobson, Curvature-Induced Polarization in Carbon Nanoshells, *Chem. Phys. Lett.* **360**, 182 (2002).

[37] W. A. Harrison, *Elementary Electronic Structure* (World Scientific, Singapore, 2004), Rev. Ed.

[38] R. C. Haddon, Hybridization and the Orientation and Alignment of π-Orbitals in Nonplanar Conjugated Organic Molecules: π-Orbital Axis Vector Analysis (POAV2), *J. Am. Chem. Soc.* **108**, 2837 (1986).

[39] R. C. Haddon, L. C. Brus, and K. Raghavachari, Electronic Structure and Bonding in Icosahedral C_{60}, *Chem. Phys. Lett.* **125**, 459 (1986).

[40] R. D. James, Objective Structures, *J. Mech. Phys. Solids* **54**, 2354 (2006).

[41] T. Dumitrică and R. D. James, Objective Molecular Dynamics, *J. Mech. Phys. Solids* **55**, 2206 (2007).

[42] K. Dayal and R.D. James, Nonequilibrium Molecular Dynamics for Bulk Materials and Nanostructures, *J. Mech. Phys. Solids* **58**, 145 (2010).

[43] C. T. White, D. H. Robertson, and J. W. Mintmire, Helical and Rotational Symmetries of Nanoscale Graphitic Tubules, *Phys. Rev. B* **47**, 5485 (1993).

[44] C. A. Coulson, B. O'Leary, and R. B. Mallion, *Hückel Theory for Organic Chemists* (Academic Press, New York, 1978).

[45] D. Porezag, Th. Frauenheim, Th. Köhler, G. Seifert, and R. Kaschner, Construction of Tight-Binding-Like Potentials on the Basis of Density-Functional Theory: Application to Carbon, *Phys. Rev. B* **51**, 12947 (1995).

[46] D.-B. Zhang, M. Hua, and T. Dumitrică, Stability of Polycrystalline and Wurtzite Si Nanowires via Symmetry-Adapted Tight-Binding Objective Molecular Dynamics, *J. Chem. Phys.* **128**, 084104 (2008).

[47] D.-B. Zhang, R.D. James, and T. Dumitrica, Dislocation Onset and Nearely Axial Glide in Carbon Nanotubes under Torsion, *J. Chem. Phys.* **130**, 071101 (2009).

[48] D.-B. Zhang, R.D. James, and T. Dumitrica, Electromechanical Characterization of Carbon Nanotubes in Torsion via Symmetry-Adapted Tight-Binding Objective Molecular Dynamics, *Phys. Rev. B* **80**, 115418 (2009).

[49] A description of the parameter set and a listing of relevant publications may be found at www.dftb.org/parameters/download/pbc.

[50] D.-B. Zhang, T. Dumitrică, and G. Seifert, Helical Nanotube Structures of MoS_2 With Intrinsic Twisting: An Objective Molecular Dynamics Study, *Phys. Rev. Lett.* **104**, 065502 (2010).

[51] D. Teich, T. Lorenz, J.-O. Joswig, G. Seifert, D.-B. Zhang, and T. Dumitrică, Structural and Electronic Properties of Helical TiS_2 Nanotubes Studied with Objective Molecular Dynamics, *J. Phys. Chem. C* **115**, 6392 (2011).

[52] D.-B. Zhang, E. Akatyeva, and T. Dumitrică, Helical BN and ZnO Nanotubes with Intrinsic Twisting: An Objective Molecular Dynamics Study, *Phys. Rev. B* **84**, 115431 (2011).

[53] I. Nikiforov, B. Hourahine, B. Aradi, Th. Frauenheim, and T. Dumitrică, Ewald Summation on a Helix: A Route to Self-Consistent Charge Density-Functional Based Tight-Binding Objective Molecular Dynamics, *J. Chem. Phys.* **139**, 094110 (2013).

[54] K.N. Kudin, G.E. Scuseria, and B.I. Yakobson, C_2F, BN, and C Nanoshell Elasticity From Ab Initio Computations, *Phys. Rev. B* **64**, 235406 (2001).

[55] S. J. Stuard, A. B. Tutein, and J. A. Harrison, A Reactive Potential for Hydrocarbons with Intermolecular Interactions, *J. Chem. Phys.* **112**, 6472 (2000).

[56] R. Rurali and E Hernandez, Trocadero: a Multiple-Algorithm Multiple-Model Atomistic Simulation Program, *Comp. Mat. Sci.* **28**, 85 (2003).

[57] D.-B. Zhang and T. Dumitrică, Elasticity of Ideal Single-Walled Carbon Nanotubes via Symmetry-Adapted Tight-Binding Objective Modeling, *Appl. Phys. Lett.* **93**, 031919 (2008).

[58] Z. Xu and M. Buehler, Geometry Controls Conformation of Graphene Sheets: Membranes, Ribbons, and Scrolls, *ACS Nano* **4**, 3869 (2010).

[59] V.B. Shenoy, C.D. Reddy, A. Ramasubramaniam and Y.W. Zhang, Edge-Stress-Induced Warping of Graphene Sheets and Nanoribbons, *Phys. Rev. Lett* **101**, 245501 (2008).

[60] I. Nikiforov, D.-B. Zhang, R. D. James, and T. Dumitrică, Wavelike Rippling in Multiwalled Carbon Nanotubes under Pure Bending, *Appl. Phys. Lett.* **96**, 123107 (2010).

[61] H. Jackman, P. Krakhmalev, and K. Svensson, Measurements of the Critical Strain for Rippling in Carbon Nanotubes, *Appl. Phys. Lett.* **98**, 183104 (2011).

[62] E. Akatyeva and T. Dumitrică, Chiral Graphene Nanoribbons: Objective Molecular Dynamics Simulations and Phase-Transition Modeling, *J. Chem. Phys.* **137**, 234702 (2012).

[63] D.-B. Zhang and T. Dumitrică, Role of the Effective Tensile Strain in the Electromechanical Response of Helical Graphene Nanoribbons with Open and Closed Edges, *Phys. Rev. B* **85**, 035445 (2012).

[64] W. Jorgensen, Theoretical Studies of Medium Effects on Conformational Equilibria, *J. Phys. Chem.* **87**, 5304 (1983).

[65] For a perspective see Jin, S.; Bierman, M.J.; Morin, S. A. A New Twist on Nanowire Formation: Screw-Dislocation- Driven Growth of Nanowires and Nanotubes. *J. Phys. Chem. Lett.* **1**, 1472 (2010).

[66] Hanrath, T.; Korgel, B. Supercritical Fluid-Liquid-Solid (SFLS) Synthesis of Si and Ge Nanowires Seeded by Colloidal Metal Nanocrystals. *Adv. Mat.* **15**, 437 (2003).

[67] Hanrath, T.; Korgel, B. Nucleation and Growth of Germanium Nanowires Seeded by Organic Monolayer-Coated Gold Nanocrystals. *J. Am. Chem. Soc.* **124**, 1424 (2002).

[68] Bierman, M. J.; Lau, Y. K. A.; Kvit, A. V.; Schmitt, A. L.; Jin, S. Dislocation-Driven Nanowire Growth and Eshelby Twist. *Science* **320**, 1060 (2008).

[69] Zhu, J.; Peng, H.; Marshall, A.F.; Barnett, D.M.; Nix, W.D.; Cui, Y. Formation of Chiral Branched Nanowires by the Eshelby Twist. *Nature Nanotech.* **3**, 477 (2008).

[70] Morin, S.A.; Bierman, M.J.; Tong, J.; Jin, S. Mechanism and Kinetics of Spontaneous Nanotube Growth Driven by Screw Dislocations. *Science* **328**, 476 (2010).

[71] Morin, S.A.; Jin, S. Screw Dislocation-Driven Epitaxial Solution Growth of ZnO Nanowires Seeded by Dislocations in GaN Substrates. *Nano Lett.* **10**, 3459 (2010).

[72] Frank, F.C. The Influence of Dislocations on Crystal Growth. *Disc. Faraday Soc.* **5**, 48 (1949).

[73] Weertman, J.; Weertman J.R. *Elementary Dislocation Theory* (Oxford University Press, New York, 1964), 1st Ed.

[74] Eshelby, J.D. Screw Dislocations in Thin Rods. *J. Appl. Phys.* **24**, 176 (1952).

[75] Bigger, J.R.K.; McInnes, D. A.; Sutton, A. P.; Payne, M. C.; Stich, I.; King-Smith, R. D.; Bird, D. M.; Clarke L. J. Atomic and Electronic Structures of the 90^0 Partial Dislocation in Silicon. *Phys. Rev. Lett.* **69**, 2224 (1992).

[76] Arias, T.A.; Joannopoulos, J.D. *Ab Initio* Theory of Dislocation Interactions: From Close-Range Spontaneous Annihilation to the Long-Range Continuum Limit. *Phys. Rev. Lett.* **73**, 680 (1994).

[77] Huang, Y.M.; Spence J.C.H.; Sankey, O.F. Dislocation Kink Motion in Silicon. *Phys. Rev. Lett.* **74**, 3392 (1995).

[78] Lehto, N.; Öberg, S. Effects of Dislocation Interactions: Application to the Period-Doubled Core of the 90^0 Partial in Silicon. *Phys. Rev. Lett.* **80**, 5568 (1998).

[79] Rao, S.; Hernandez, D.; Simmonds, J. P.; Parthasarathy, T. A.; Woodward, C. Green's Function Boundary Conditions in Two-Dimensional and Three-Dimensional Atomistic Simulations of Dislocations. *Philos. Mag. A*, **77**, 231 (1998).

[80] Zhang, R.Q.; Lifshitz, Y.; Ma, D.D.D.; Zhao, Y.L.; Fraunheim, Th.; Lee, S.T.; Tong, S.Y. Structures and Energetics of Hydrogen-Terminated Silicon Nanowire Surfaces. *J. Chem. Phys.* **123**, 144703 (2005).

[81] Xu, Hu; Yang, X. B.; Guo, C.S.; Zhang, R.Q. An Energetic Stability Predictor of Hydrogen-Terminated Si Nanostructures. *Appl. Phys. Lett.* **95**, 253106 (2009).

[82] Furmanchuk, A.; Isayev, O.; Dinadayalane, T.C.; Leszczynski, J. Car-Parrinello Molecular Dynamics Simulations of Tensile Tests on Si $\langle 001 \rangle$ Nanowires. *J. Phys. Chem. C* **115**, 12283 (2011).

[83] Zhang, D.-B.; Dumitrică, T. Effective Strain in Helical Rippled Carbon Nanotubes: A Unifying Concept for Understanding Electromechanical Response. *ACS Nano* **4**, 6966 (2010).

[84] Tan, T.Y.; Lee, S.T.; Gösele, U. A Model for Growth Directional Features in Silicon Nanowires. *Appl. Phys. A* **74**, 423 (2002).

[85] Cui, Y.; Lauhon, L. J.; Gudiksen, M. S.; Wang, J.; Lieber, C. M. Diameter-Controlled Synthesis of Single-Crystal Silicon Nanowires. *Appl. Phys. Lett.* **78**, 2214 (2001).

[86] Frauenheim, Th.; Weich, F.; Kohler, Th.; Uhlmann, S.; Porezag, D.; Seifert, G. Density-Functional-Based Construction of Transferable Nonorthogonal Tight-Binding Potentials for Si and SiH. *Phys. Rev. B* **52**, 11492 (2005).

[87] Guo, C.S.; Luo, L.B.; Yuan, G.D.; Yang, X.B.; Zhang, R.Q.; Zhang, W.J.; Lee, S.T. Surface Passivation and Transfer Doping of Silicon Nanowires. *Angew. Chem. Int. Ed.* **121**, 10080 (2009).

[88] Zhang, D.-B.; Dumitrică, T. Modulating the Optical and Electronic Properties of Highly Symmetric Si Quantum Dots. *Nanotechnol.* **20**, 445401 (2009).

[89] See, for example, W. Falk and R.D. James, Elasticity Theory for Self-Assembled Protein Lattices with Application to the Martensitic Phase Transition in Bacteriophage T4 Tail Sheath, *Phys. Rev. E* **73**, 011917 (2006).

[90] J. Ishioka, Y. H. Liu, K. Shimatake, T. Kurosawa, K. Ichimura, Y. Toda, M. Oda, and S. Tanda, Chiral Charge-Density Wave, *Phys. Rev. Lett.* **105**, 176401 (2010).

[91] R. Gutierrez, E. Diaz, R. Naaman, and G. Cuniberti, Spin-Selective Transport Through Helical Molecular Systems, *Phys. Rev. B* **85**, 081404(R) (2012).

[92] G. Edwards, D. Hochberg, and T.W. Kephart, Structure in the Electric Potential Emanating from DNA, *Phys. Rev. E* **50**, 698 (1994).

[93] P.J. Lin-Chung and A.K. Rajagopal, Helical Coordinate System and Electrostatic Fields of Double-Helix Charge Distributions, *Phys. Rev. E* **52**, 901 (1995).

[94] D. Hochberg, G. Edwards, and T.W. Kephart, Representing Structural Information of Helical Charge Distributions in Cylindrical Coordinates, *Phys. Rev. E* **55**, 3765 (1997).

[95] J. Landy and J. Rudnick, Symmetries of Interacting Helices of Charge, *Phys. Rev. E* **81**, 061918 (2010).

[96] A.A. Kornyshev and S. Leikin, Theory of Interaction Between Helical Molecules, *J. Chem. Phys.* **107**, 3656 (1997).

[97] F.J. Solis, G. Vernizzi, and M.O. de la Cruz, Electrostatic-Driven Pattern Formation in Fibers, Nanotubes and Pores, *Soft Matt.* **7**, 1456 (2011).

[98] P.L. Overfelt, Helical Harmonics for Static Fields, *Phys. Rev. E* **64**, 036603 (2001).

[99] P.P. Ewald, Die Berechnung optischer und elektrostatischer Gitterpotentiale, *Ann. Phys.* **369**, 253 (1921).

[100] N. Karasawa and W.A. Goddard III, Acceleration of Convergence for Lattice Sums, *J. Phys. Chem.* **93**, 7320 (1989).

[101] F.G. Fumi and M.P. Tosi, Extension of the Madelung Method for the Evaluation of Lattice Sums, *Phys. Rev.* **117**, 1466 (1960).

[102] D.E. Parry, The Electrostatic Potential in the Surface Region of an Ionic Crystal, *Surf. Sci.* **49**, 433 (1975).; *ibidem*, **54**, 195 (1976).

[103] M. Born and K. Huang, *Dynamical Theory of Crystal Lattices* (Oxford University Press, Oxford, 1954).

[104] C. Kittel, *Introduction to Solid State Physics* (John Wiley & Sons, Inc., Hoboken, 1996).

[105] M. Porto, Ewald Summation of Electrostatic Interactions of Systems with Finite Extent in Two of Three Dimensions, *J. Phys. A* **33**, 6211 (2000).

[106] D.J. Langridge, J.F. Hart, and S. Crampin, Ewald Summation Technique for One-Dimensional Charge Distributions, *Comp. Phys. Comm.* **134**, 78 (2001).

[107] A. Brodka and P. Sliwinski, Three-Dimensional Ewald Method with Correction Term for a System Periodic in One Direction, *J. Chem. Phys.* **120** 5518 (2004).

[108] O.N. Osychenko, G.E. Astrakharchik, and J. Boronat, Ewald Method for Polytropic Potentials in Arbitrary Dimensionality, *Mol. Phys.* **110**, 227 (2012).

[109] M. Elstner, D. Porezag, G. Jungnickel, J. Elsner, M. Haugk, T. Frauenheim, S. Suhai, and G. Seifert, Self-Consistent-Charge Density-Functional Tight-Binding Method for Simulations of Complex Materials Properties, *Phys. Rev. B* **58**, 7260 (1998).

[110] A. Carlson and T. Dumitrică, Extended Tight-Binding Potential for Modelling Intertube Interactions in Carbon Nanotubes, *Nanotechnol.* **18**, 065706 (2007).

[111] I. Nikiforov, D.-B. Zhang, and T. Dumitrică, Screw Dislocations in ⟨100⟩ Silicon Nanowires: An Objective Molecular Dynamics Study, *J. Phys. Chem. Lett.* **2**, 2544 (2011).

[112] D.-B. Zhang and T. Dumitrică, Effective-Tensional-Strain-Driven Bandgap Modulations in Helical Graphene Nanoribbons, *Small* **7**, 1023 (2011).

[113] M. Yang and N.A. Kotov, Nanoscale Helices from Inorganic Materials, *J. Mater. Chem.* **21**, 6775 (2011).

[114] Th. Frauenheim, G. Seifert, M. Elstner, Z. Hajnal, G. Jungnickel, D. Porezag, S. Suhai, R. Scholz, A Self-Consistent Charge Density-Functional Based Tight-Binding Method for Predictive Materials Simulations in Physics, Chemistry and Biology, *Phys. Stat. Sol. (b)* **217**, 41 (2000).

[115] M. Elstner, Th. Frauenheim, and S. Suhai, An Approximate DFT Method for QM/MM Simulations of Biological Structures and Processes, *J. Mol. Struct. (THEOCHEM)* **632**, 29 (2003). M. Elstner, The SCC-DFTB Method and its Application to Biological Systems, *Theor. Chem. Acc.* **116**, 316 (2006).

[116] M. Abramowitz and I.A. Stegun (Eds.), *Handbook of Mathematical Functions* (Dover, New York, 1972), 6.1.1 p. 255.

[117] E. Madelung, *Die Math. Hilfsmittel des Physikers* (Springer, Berlin, 1950).

[118] In general, $\sum_{\zeta=-\infty}^{+\infty} f(\zeta) = \sum_{k=-\infty}^{+\infty} \int_{-\infty}^{\infty} f(x) e^{-2\pi i k x} dx$. Here $f(\zeta) = e^{-t(\zeta T + T_0 - T')^2 + il\zeta\theta}$. This formula is a specific case of the general Poisson summation formula, $\sum_{\zeta=-\infty}^{+\infty} f(x' + \zeta L) = \frac{1}{L} \sum_{k=-\infty}^{+\infty} e^{2\pi i k x'/L} \int_{-\infty}^{\infty} f(x) e^{-2\pi i k x/L} dx$, with $x' = 0$ and $L = 1$.

[119] F.E. Harris, Incomplete Bessel, Generalized Incomplete Gamma, or Leaky Aquifer Functions, *J. Comp. Appl. Math.* **215**, 260 (2008).

[120] B. Aradi, B. Hourahine, and Th. Frauenheim, DFTB+, a Sparse Matrix-Based Implementation of the DFTB Method, *J. Phys. Chem. A* **111**, 5678 (2007).

[121] M. Elstner, P. Hobza, T. Frauenheim, S. Suhai, and E. Kaxiras, Hydrogen Bonding and Stacking Interactions of Nucleic Acid Base Pairs: a Density-Functional-Theory Based Treatment, *J. Chem. Phys.* **114**, 5149 (2001).

[122] L. Zhechkov, T. Heine, S. Patchkovskii, G. Seifert, and H.A. Duarte, An Efficient a Posteriori Treatment for Dispersion Interaction in Density-Functional-Based Tight Binding, *J. Chem. Theory Comput.* **1**, 841 (2005).

[123] B. Grundkötter-Stock, V. Bezugly, J. Kunstmann, G. Cuniberti, Th. Frauenheim, and Th. A. Niehaus, SCC-DFTB Parametrization for Boron and Boranes, *J. Chem. Theory Comput.* **8**, 1153 (2012).

[124] H.J. Monkhorst and J.D. Pack, Special Points for Brillouin-Zone Integrations, *Phys. Rev. B* **13** 5188 (1976).

[125] E. Akatyeva, L. Kou, I. Nikiforov, T. Frauenheim, and T. Dumitrică, Electrically Active Screw Dislocations in Helical ZnO and Si Nanowires and Nanotubes, *ACS Nano* **6**, 10042 (2012).

[126] E. Akatyeva and T. Dumitrică, Eshelby Twist and Magic Helical Zinc Oxide Nanowires and Nanotubes, *Phys. Rev. Lett.*, **109** 035501 (2012).

[127] A. Pérez, F.J. Luque, and M. Orozco, Frontiers in Molecular Dynamics Simulations of DNA, *Acc. Chem. Res.* **45**, 196 (2012).

[128] A. Noy and R. Golestanian, Length Scale Dependence of DNA Mechanical Properties, *Phys. Rev. Lett.* **109**, 228101 (2012).

[129] T. Macke, and D.A. Case, in *Molecular Modeling of Nucleic Acids*, edited by N.B. Leontes and J. SantaLucia, Jr. (American Chemical Society, Washington, DC, 1998), pp. 379-393.

[130] S. Arnott, P.J. Campbell Smith, and R. Chandraseharan, in *Handbook of Biochemistry and Molecular Biology, 3rd Ed. Nucleic Acids – Vol. II*, edited by G.P. Fasman. (CRC Press, Cleveland, 1976), pp. 411-422.

[131] The code we used for coordinate generation can be found at http://structure.usc.edu/make-na.

[132] M. Gaus, Q. Cui, and M. Elstner, DFTB3: Extension of the Self-Consistent-Charge Density-Functional Tight-Binding Method (SCC-DFTB), *J. Chem. Theory Comput.* **7**, 931 (2011).

[133] P. H. Tan, W. P. Han, W. J. Zhao, Z. H. Wu, K. Chang, H. Wang, Y. F. Wang, N. Bonini, N. Marzari, N. Pugno, G. Savini, A. Lombardo, and A. C. Ferrari, The Shear Mode of Multilayer Graphene, *Nature Mater.* **11**, 294 (2012).

[134] E. A. Henriksen, D. Nandi, and J. P. Eisenstein, Quantum Hall Effect and Semimetallic Behavior of Dual-Gated ABA-Stacked Trilayer Graphene, *Phys. Rev. X* **2**, 011004 (2012).

[135] H. Zeng, C. Zhi, Z. Zhang, X. Wei, X. Wang, W. Guo, Y. Bando, and D. Golberg, "White Graphenes": Boron Nitride Nanoribbons via Boron Nitride Nanotube Unwrapping, *Nano Lett.* **10**, 5049 (2010).

[136] N. Marom, J. Bernstein, J. Garel, A. Tkatchenko, E. Joselevich, L. Kronik, and O. Hod, Stacking and Registry Effects in Layered Materials: The Case of Hexagonal Boron Nitride, *Phys. Rev. Lett.* **105**, 046801 (2010).

[137] K. K. Kim, A. Hsu, X. Jia, S. Min Kim, Y. Shi, M. Hofmann, D. Nezich, J. F. Rodriguez-Nieva, M. Dresselhaus, T. Palacios, and J. Kong, Synthesis of Monolayer Hexagonal Boron Nitride on Cu Foil Using Chemical Vapor Deposition, *Nano Lett.* **12**, 161 (2012).

[138] X. Bai, D. Golberg, Y. Bando, C. Zhi, C. Tang, M. Mitome, and K. Kurashima, Deformation-Driven Electrical Transport of Individual Boron Nitride Nanotubes, *Nano Lett.* **7**, 632 (2007).

[139] H. Zhao, K. Min, and N. R. Aluru, Size and Chirality Dependent Elastic Properties of Graphene Nanoribbons under Uniaxial Tension, *Nano Lett.* **9**, 3012 (2009).

[140] J. Song, J. Wu, Y. Huang, and K. C. Hwang, Continuum Modeling of Boron Nitride Nanotubes, *Nanotechnology* **19**, 445705 (2008).

[141] J. Tersoff, Modeling Solid-State Chemistry: Interatomic Potentials for Multicomponent Systems, *Phys. Rev. B* **39**, 5566(R) (1989).

[142] V. Verma, V. K. Jindal, and K. Dharamvir, Elastic Moduli of a Boron Nitride Nanotube, *Nanotechnology* **18**, 435711 (2007).

[143] L. A. Girifalco, M. Hodak, and R. S. Lee, Carbon Nanotubes, Buckyballs, Ropes, and a Universal Graphitic Potential, *Phys. Rev. B* **62**, 13104 (2000).

[144] L. Mahadevan, J. Bico, and G. McKinley, Popliteal Rippling of Layered Elastic Tubes and Scrolls, *Europhys. Lett.* **65**, 323 (2004).

[145] S. Iijima, C. Brabec, A. Maiti, and J. Bernholc, Structural Flexibility of Carbon Nanotubes, *J. Chem. Phys.* **104**, 2089 (1996).

[146] J. Brivio, D. T. L. Alexander, and A. Kis, Ripples and Layers in Ultrathin MoS_2 Membranes, *Nano Lett.* **11**, 5148 (2011).

[147] P. K. Schelling, S. R. Phillpot, and P. Keblinski, Comparison of Atomic-Level Simulation Methods for Computing Thermal Conductivity, *Phys Rev. B* **65**, 144306 (2001).

[148] J. Li, L. Porter, and S. Yip, Atomistic Modeling of Finite-Temperature Properties of Crystalline β-SiC II. Thermal Conductivity and Effects of Point Defects, *J. Nucl. Mater.* **255**, 139 (1998).

[149] A. Guajardo-Cuéllar, D. B. Go, and M. Sen, Evaluation of Heat Current Formulations for Equilibrium Molecular Dynamics Calculations of Thermal Conductivity, *J. Chem. Phys.* **132**, 104111 (2010).

[150] T. W. Sirk, S. Moore, and E. F. Brown, Characteristics of Thermal Conductivity in Classical Water Models, *J. Chem. Phys.* **138**, 064505 (2013).

[151] S. Plimton, Fast Parallel Algorithms for Short-Range Molecular Dynamics, *J. Comp. Phys.* **117**, 1 (1995).

[152] J. Tersoff, New Empirical Model for the Structural Properties of Silicon, *Phys. Rev. Lett.* **56**, 632 (1986).

[153] G. C. Abell, Empirical Chemical Pseudopotential Theory of Molecular and Metallic Bonding, *Phys. Rev. B* **31**, 6184 (1985).

Appendix A

Geometric description of CNT structure

Bent graphene is modeled as a large-diameter CNT. With the objective structures concept [40], the CNT can be constructed by applying symmetry operations to one carbon atom. These symmetry operations are given by the discrete group of isometries

$$\{h^{\zeta_h} g^{\zeta_g} f^{\zeta_f} : \zeta_h \in \mathbb{Z},\, \zeta_g = 1, \ldots, N_g,\, \zeta_f = 1, 2\}. \tag{A.1}$$

Here h, g and f are the helical, angular and 180° rotation about some axis operations respectively, operating on a single point in $\mathbb{R}^3$. h and g are the operations defined elsewhere in the dissertation, are used in Sec. 4.3. Operation f is not used is the simulations – it is used *a priori* to construct the simulation cell. It is a demonstration of a further possible simplification of the objective description, reducing the 2-atom unit cell to one atom. Formally:

1. $h = (\mathbf{R}_\gamma | \, \mathbf{T})$, $\mathbf{T} \equiv T\mathbf{e}$, $\mathbf{R}_\gamma \mathbf{e} = \mathbf{e}$, $|\mathbf{e}| = 1$, is the helical operation, a rotation of angle γ combined with a translation $T \neq 0.$, with a shared axis $\mathbf{e}$.

2. $g = (\mathbf{R}_\psi | \, 0)$, $\mathbf{R}_\psi \mathbf{e} = \mathbf{e}$, is the pure angular rotation of angle $\psi = 2\pi/N_g$, $N_g \in \mathbb{Z}$, $N_g \neq 0$ around axis $\mathbf{e}$.

3. $f = (\mathbf{R} | \, 0)$, $\mathbf{R} = -\mathbf{I} + 2\mathbf{e}_1 \otimes \mathbf{e}_1$, $|\mathbf{e}_1| = 1, \mathbf{e} \cdot \mathbf{e}_1 = 0$, is a 180° rotation about axis $\mathbf{e}_1$, defined below.

The following is summarized from Ref.[41]. The standard choice of lattice vectors $\mathbf{t}_1, \mathbf{t}_2$ is used to describe one of the two sublattices of graphene, so that $\mathbf{C} = n\mathbf{t}_1 + m\mathbf{t}_2$ is the chiral vector (Fig. 4.1). For integers p, q, define

$$\begin{aligned} \mathbf{X}(p,q) &= R\cos(2\pi\xi(p,q))\,\mathbf{a}_1 + R\sin(2\pi\xi(p,q))\,\mathbf{a}_2 + (\eta(p,q) - \frac{1}{2}\eta(1/3,1/3))\,\mathbf{a}_3, \\ \text{where}\quad \xi(p,q) &= \frac{(2n+m)p + (2m+n)q}{2(n^2+m^2+nm)}, \\ \eta(p,q) &= \frac{3a(pm-qn)}{2\sqrt{n^2+m^2+nm}}, \\ R &= \frac{a}{2\pi}\sqrt{3(n^2+m^2+nm)}, \end{aligned} \tag{A.2}$$

where $\mathbf{a}_1, \mathbf{a}_2, \mathbf{a}_3$ is an orthonormal basis and a is the carbon-carbon bond length. The atomic positions of the rolled up sheet are then given by $\mathbf{X}(p,q)$ and $\mathbf{X}(p+1/3, q+1/3)$, $p, q \in \mathbb{Z}$. Note that

$$\begin{aligned} \mathbf{X}(0,0) &= R\,\mathbf{a}_1 - \frac{1}{2}\eta(1/3,1/3)\mathbf{a}_3, \qquad (A.3) \\ \mathbf{X}(1/3,1/3) &= R\,\cos(2\pi\xi(1/3,1/3))\,\mathbf{a}_1 + R\,\sin(2\pi\xi(1/3,1/3))\,\mathbf{a}_2 + \frac{1}{2}\eta(1/3,1/3)\mathbf{a}_3. \end{aligned}$$

The formula (A.2) differs by an additive constant from that in [41]. It is also clear from (A.3) that $\mathbf{e}_1$ should be the unit vector

$$\mathbf{e}_1 = \cos(\pi\xi(1/3,1/3))\,\mathbf{a}_1 + \sin(\pi\xi(1/3,1/3))\,\mathbf{a}_2. \tag{A.4}$$

Note that a 180° rotation about $\mathbf{e}_1$ maps $\mathbf{X}(0,0)$ into $\mathbf{X}(1/3,1/3)$. So the group (A.1) acts on $\mathbf{X}(0,0)$ only.

The remaining task is to find $h = (\mathbf{R}_\gamma|T\mathbf{e})$ and $g = (\mathbf{R}_\psi|0)$ of (A.1). Since g and h have the common axis $\mathbf{e} = \mathbf{a}_3$,

$$h^{\zeta_h} g^{\zeta_g} = (\mathbf{R}_{\zeta_h\gamma+\zeta_g\psi}|\zeta_h T\mathbf{a}_3). \tag{A.5}$$

Hence to make (A.5) agree with the formula for $\mathbf{X}(p,q)$ in (A.2) it is necessary to find, for every pair of integers (p,q), a pair (ζ_h, ζ_g), $\zeta_h \in \mathbb{Z}$, $\zeta_g = 1, \ldots, N_g$, such that

$$\begin{aligned} \zeta_h\gamma + \zeta_g\psi &= 2\pi\xi(p,q) = 2\pi\frac{(2n+m)p + (2m+n)q}{2(n^2+m^2+nm)}, \\ \zeta_h T &= \eta(p,q) = \frac{3a(pm-qn)}{2\sqrt{n^2+m^2+nm}}, \end{aligned} \tag{A.6}$$

and conversely. The general theory says that this is always possible. To do this, look first at the second of (A.6). The key question is, what is the smallest positive value of $pm - qn$? This is answered by the Extended Euclidean algorithm. This says that, given n and m, the smallest positive integer value of $pm - qn$ is the greatest common divisor of n, m, briefly GCD(n, m). Let p^*, q^* be integers delivered by the Extended Euclidean algorithm, $p^*m - q^*n = l$, where $l = \text{GCD}(n, m)$. Therefore, all values of $\eta(p, q)$ are obtained by choosing

$$T = \frac{3a\ l}{2\sqrt{n^2 + m^2 + nm}}. \tag{A.7}$$

In fact, using this value of T also gives a formula relating (ζ_h, ζ_g) to (p, q) from (A.6):

$$\begin{aligned} p &= \zeta_h p^* + \zeta_g P, \\ q &= \zeta_h q^* + \zeta_g Q, \end{aligned} \tag{A.8}$$

where the integers P, Q satisfy $Pm - Qn = 0$. The latter ensures that the result is the general solution of (A.6). The general solution of $Pm - Qn = 0$ is now

$$P = \frac{n}{l}, \quad Q = \frac{m}{l}. \tag{A.9}$$

Equation (A.8) implies that for every pair of integers (p, q) there is a pair $(\zeta_h, \zeta_g),\ \zeta_h \in \mathbb{Z},\ \zeta_g = 1, \ldots, N_g$. Now, substitute (A.8), (A.9) into the first equation in (A.6) and simplify. This results in

$$\gamma = \pi\Big(\frac{(2n + m)p^* + (2m + n)q^*}{n^2 + m^2 + nm}\Big), \quad \psi = 2\pi/l. \tag{A.10}$$

Appendix B

Angles and Bond Lengths in Ideal CNT structure

With the atom notation shown in Fig. B.1, the bond length a_i (distance between the two atoms) for bond $i = 1, 2, 3$ which makes an angle β_i with the circumferential vector $\mathbf{C}$ in a CNT of radius R created by using the procedure in Appendix 1 can be written as

$$a_i = \sqrt{4R^2 \sin^2\left(\frac{a\cos\beta_i}{2R}\right) + a^2 \sin^2\beta_i} = a - \frac{2a\cos^4\beta_i}{3}\theta^2 + O\left(\theta^4\right), \tag{B.1}$$

where a is the bond length in flat graphene.

The bond angles in the bent graphene

$$\theta_{ij} = \cos^{-1}\left(\hat{\mathbf{b}}_i \cdot \hat{\mathbf{b}}_j\right) \tag{B.2}$$

are given by

$$\begin{aligned}
\theta_{12} &= \frac{2\pi}{3} - \frac{\theta^2}{\sqrt{3}}\left(3 + 5\sin(2\beta + \frac{\pi}{6}) + \frac{7}{4}\sin(4\beta - \frac{\pi}{6})\right) + O(\theta^4), \\
\theta_{23} &= \frac{2\pi}{3} - \frac{\theta^2}{\sqrt{3}}\left(3 - 5\cos(2\beta) + \frac{7}{4}\cos(4\beta)\right) + O(\theta^4), \\
\theta_{31} &= \frac{2\pi}{3} - \frac{\theta^2}{\sqrt{3}}\left(3 - 5\sin(2\beta - \frac{\pi}{6}) - \frac{7}{4}\sin(4\beta + \frac{\pi}{6})\right) + O(\theta^4).
\end{aligned} \tag{B.3}$$

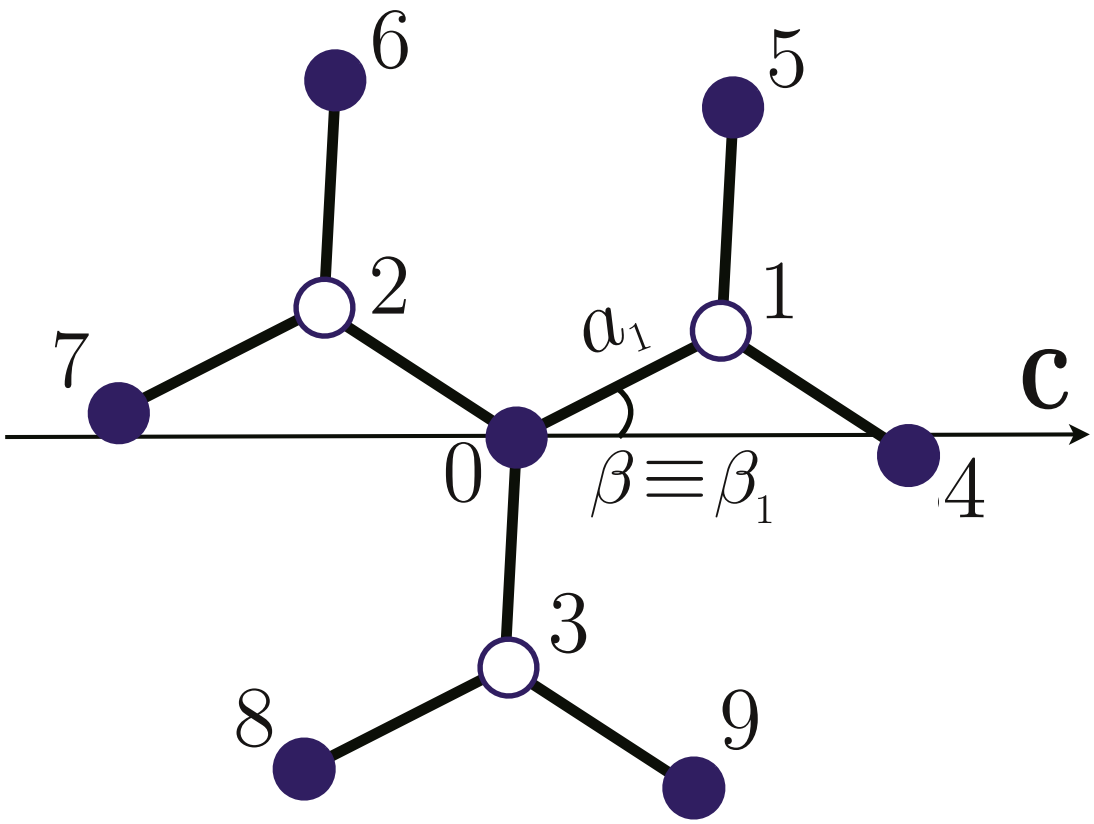

Figure B.1: Numbering scheme for first- and second-nearest neighbors of central atom 0. **C** indicates the roll-up direction. Bond length a_1 and angle β_1 (Eq. B.1) are indicated. As before, $\beta \equiv \beta_1$ for angle calculations.

Here, $i, j = 1, 2, 3$ correspond to the nearest neighbors of the central atom 0, omitted in the angle notation. See Fig. B.1 for the neighbor numbering scheme. $\hat{\mathbf{b}}_i$ and $\hat{\mathbf{b}}_j$ are the unit vectors corresponding to the bonds connecting atoms i and j to atom 0. So, $\hat{\mathbf{b}}_i = (\mathbf{X}_i - \mathbf{X}_0)/|\mathbf{X}_i - \mathbf{X}_0| = (\mathbf{X}_i - \mathbf{X}_0)/a_i$, where $\mathbf{X}_i$ and $\mathbf{X}_0$ are atomic positions, and analogously for j.

Dihedral angles

$$\Theta_{ijk} = \text{atan2}(-\hat{\mathbf{b}}_i \cdot [\hat{\mathbf{b}}_j \times \hat{\mathbf{b}}_k], [-\hat{\mathbf{b}}_i \times \hat{\mathbf{b}}_j] \cdot [\hat{\mathbf{b}}_j \times \hat{\mathbf{b}}_k]), \tag{B.4}$$

can be written as

$$\begin{aligned}
\Theta_{214} &= \pi + \theta[4\sin(2\beta) + 2\sqrt{(3)}] + O(\theta^3), \\
\Theta_{215} &= \Theta_{314} = \varphi_1, \\
\Theta_{315} &= \pi + \theta[4\sin(2\beta) - 2\sqrt{(3)}] + O(\theta^3), \\
\Theta_{126} &= \Theta_{327} = \varphi_2, \\
\Theta_{127} &= \pi - 8\theta\cos(\beta - \pi/6)\cos(\beta) + O(\theta^3), \\
\Theta_{326} &= \pi + 8\theta\sin(\beta - \pi/6)\sin(\beta) + O(\theta^3), \\
\Theta_{138} &= \pi + 8\theta\cos(\beta + \pi/6)\cos(\beta) + O(\theta^3), \\
\Theta_{139} &= \Theta_{238} = \varphi_3, \\
\Theta_{239} &= \pi - 8\theta\sin(\beta + \pi/6)\sin(\beta) + O(\theta^3).
\end{aligned} \tag{B.5}$$

Here, $\hat{\mathbf{b}}_i$ and $\hat{\mathbf{b}}_j$ are the same as previously. Atom k is a second-nearest neighbor of the central atom 0, ranging from 4 to 9 (see Fig. B.1). $\hat{\mathbf{b}}_k$ corresponds to the bond connecting atom k to atom j, $\hat{\mathbf{b}}_k = (\mathbf{X}_k - \mathbf{X}_j)/|\mathbf{X}_k - \mathbf{X}_j|$. atan2$(y, x)$ is the four-quadrant arctangent function which returns a full 2π range of values, $\Theta_{ijk} \in (-\pi, \pi]$. The indices must be ordered such that the vectors are head-to-tail. This is also the reason for the negative sign in Eq. B.4. This is necessary in order to distinguish between $\Theta_{ijk} \approx 0$ (such as Θ_{215} and all other torsional misalignment angles) and $\Theta_{ijk} \approx \pi$ (such as Θ_{214}). This distinction is important if the dihedral-angle term is not symmetric about $\Theta_{ijk} = \pm\pi/2$, such as in the AIREBO potential as described in Section 4.4. If the dihedral-angle term is symmetric about $\Theta_{ijk} = \pm\pi/2$, such as in Brenner's second-generation potential, this distinction is unimportant.

Appendix C

Radial Corrections to Ideal CNT Structure

Here, the radial expansion caused by the two mechanisms described in Section 4.3 – the shortening of the bonds due to rolling and the elastic bend-stretch competition – is examined. Because the simulations in Fig. 4.4 a) are restricted to plane strain (no axial relaxation), the same restriction is made here.

First, the radius that the nanotube expands to in order to compensate for the shortening of the bonds caused by the roll up construction is calculated. In Eq. B.1, the bond lengths a_i that occur in a CNT of radius R created by the ideal roll-up construction were calculated. Now, uniformly deform the nanotube by varying the radius R_0, and observe how the bond lengths a_i^0 vary:

$$a_i^0 = \sqrt{4R_0^2 \sin^2\left(\frac{a\cos\beta_i}{2R}\right) + a^2 \sin^2\beta_i}, \tag{C.1}$$

The strain ϵ_i^0 in bond i when the tube is deformed to radius R_0, then, is $\epsilon_i^0 = a_i^0/a - 1$, where a is the bond length in flat graphene. The non-linearity of the bond deformation caused by the roll-up construction is evident from Eq. C.1. Because of this, it is in general not possible to choose an R_0 so that the strains in all three bonds are zero. Each bond is approximated as a linear spring, resulting in the following relationship for

the bond strain energy in the CNT deformed to radius R_0:

$$E_0 \propto \sum_{i=1}^{3} (\epsilon_i^0)^2. \tag{C.2}$$

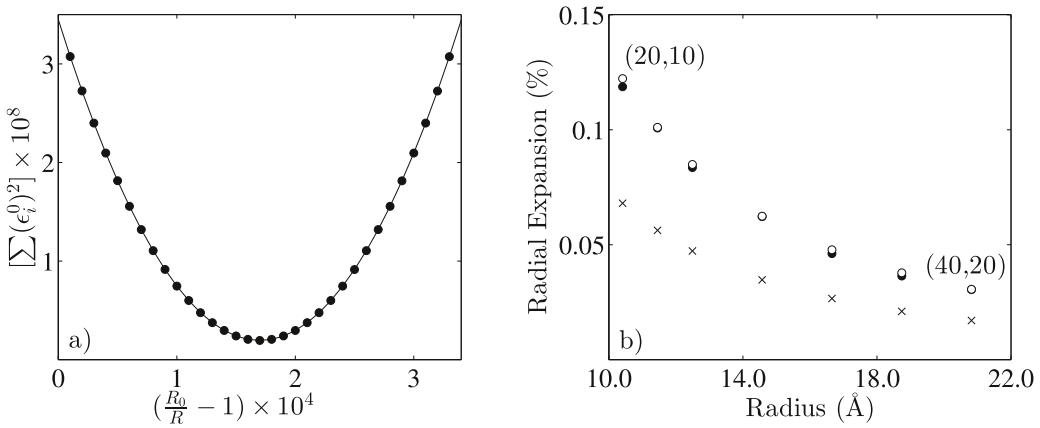

Figure C.1: a) Optimization of bond strain energy w.r.t. radius R_0 for a (40,20) CNT. b) Mechanisms of radial expansion. Crosses represent bond length optimization only (Eq. C.2). Empty circles represent optimization of bend-stretch energy balance (Eq. C.3 after carrying out bond length optimization). Filled circles represent relaxed configurations from simulations in Section 4.3.

This energy is numerically optimized to find the optimal R_0 (Fig. C.1 a)). Now, this optimal R_0 is taken as the configuration that is free of circumferential in-plane strain and the second mechanism of radial expansion – competition between in-plane and bending strain energy – is examined. Consider an elastic layer with in-plane stiffness C, Poisson's ratio ν and bending stiffness D. If the radius R_0 is the radius that results in zero in-plane strain in the circumferential direction, then the circumferential plane strain at some radius R_1 is $\epsilon_c = R_1/R_0 - 1$. Then, the total strain energy at radius R_1, assuming plane strain, is

$$W = \frac{1}{2}(1+\nu^2)C\left(\frac{R_1}{R_0} - 1\right)^2 + \frac{1}{2}D\left(\frac{1}{R_1}\right)^2. \tag{C.3}$$

The balance between the two terms of this equation is the primary reason for the radial expansion seen in Fig. 4.4 a). A bent elastic layer will take on a small amount

of in-plane strain in the circumferential direction, because this increases the radius and therefore reduces the bending strain. Differentiating w.r.t. R_1 and setting the derivative to zero results in following quartic equation for R_1 after rearrangement:

$$\frac{(1+\nu^2)C}{R_0^2}R_1^4 - \frac{(1+\nu^2)C}{R_0}R_1^3 - D = 0. \tag{C.4}$$

The discriminant of this equation is always negative, so there are two real and two complex conjugate roots. It can be shown that only one of the real roots is positive, providing an unambiguous result for the optimal radius. Fig. C.1 b) shows these radius corrections. Crosses correspond to the radius R_0 from the bond-length correction alone (Eq. C.2). Empty circles represent the radius R_1 when the bend-stretch energy balance correction (Eq. C.3) is applied after the bond-length correction. The elastic constants C and $D = E_b''$ calculated in Section 4.3 (Table 4.2), and $\nu = 0.151$, calculated from flat graphene using the same parameter set, are used. Filled circles reperesent the radial expansion seen in the OMD-DFTB simulations (identical to Fig. 4.4 a)). The two corrections entirely account for the radial expansion seen in the simulations.

Appendix D

Helical Ewald Summation Code

Provided below is Fortran code for computing the Ewald summation on a helix. The additional Fortran subroutines for the required special functions are freely available as part of the SLATEC Common Mathematical Library on the Netlib Repository. The upper incomplete gamma function is implemented in the short-range potential using the dgamit.f subroutine which computes Tricomi's incomplete gamma function (Gautschi, Walter. *The incomplete gamma functions since Tricomi.* In *Tricomi's Ideas and Contemporary Applied Mathematics*, Atti dei Convegni Lincei, n. 147, Accademia Nazionale dei Lincei. 1998.) The long-range potential is calculated using zbesi.f, which calculates a series of modified Bessel functions of the first kind, of arbitrary orders in integer increment - very convenient for calculating this term for all considered values of l at once. All the dependencies of these functions are included in SLATEC as well. The machine constant subroutines d1mach.f and i1mach.f need to have the correct lines uncommented to match the machine being used, or the subroutines need to be replaced with modern, selfadapting versions.

D.1 Primary Module

```
!> Contains functions for calculating helical Ewald summation.
!!
!! \details We make some simplifications in variables without loss of generality:
!! - T_prime in the code is equivalent to (T^0 - T') in the paper
```

```
!! - gamma_prime in the code is equivalent to (gamma^0 - gamma') in the paper.
module helicalEwald
  use interfaces
  use accuracy
  use parameters
  implicit none
  private

  public :: helicalEwaldPotential

contains

  !> Main driving function
  !!
  !! \param r  Radius of helix of charges, starting positon (r, 0, 0).
  !! \param T  Translational operation.
  !! \param gamma  Angle of rotation operation.
  !! \param r_prime  1st cylindrical coordinate (r) of point at which the
  !!     potential is evaluated.
  !! \param T_prime  2nd cylindrical coordinate (z) of point at which the
  !!     potential is evaluated.
  !! \param gamma_prime  3rd cylindrical coordinate (gamma) of point at which the
  !!     potential is evaluated.
  !! \param eta  Numerical Ewald split parameter.
  !! \param zeta_max  Maximum summation index in V^S.
  !! \param l_max  Maximum l summation index in V^L.
  !! \param k_max  Maximum k summation index in V^L (usually zero).
  !! \param intervals  Number of numerical integration intervals in V^L.
  !!
  function helicalEwaldPotential (r, T, gamma, r_prime, T_prime,&
      & gamma_prime, eta, zeta_max, l_max, k_max, intervals) result(res)
    real(dp), intent(in) :: r, T, gamma, r_prime, T_prime, gamma_prime, eta
```

```
  integer, intent(in) :: zeta_max, l_max, k_max, intervals
  real(dp) :: res

  res = V_S(r, T, gamma, r_prime, T_prime, gamma_prime, eta, zeta_max)&
      & + V_L(r, T, gamma, r_prime, T_prime, gamma_prime, eta, l_max, k_max,&
      & intervals)

end function helicalEwaldPotential


!> Calculates short-ranged V^S component of helical Ewald summation.
!!
!! \param r  Radius of helix of charges, starting positon (r, 0, 0).
!! \param T  Translational operation.
!! \param gamma  Angle of rotation operation.
!! \param r_prime  1st cylindrical coordinate (r) of point at which the
!!     potential is evaluated.
!! \param T_prime  2nd cylindrical coordinate (z) of point at which the
!!     potential is evaluated.
!! \param gamma_prime  3rd cylindrical coordinate (gamma) of point at which the
!!     potential is evaluated.
!! \param eta  Numerical Ewald split parameter.
!! \param zeta_max  Maximum summation index in V^S.
!!
function V_S(r, T, gamma, r_prime, T_prime, gamma_prime, eta,&
    & zeta_max)
  real(dp), intent(in) :: r, T, gamma, r_prime, T_prime, gamma_prime, eta
  integer, intent(in) :: zeta_max
  real(dp) :: V_S

  integer :: zeta
  real(dp) :: R_zeta, R_zeta_2
```

```
real(dp) :: R_0, R_0_2
real(dp) :: sqrt_eta

V_S = 0.0_dp
sqrt_eta = sqrt(eta)

! negative zeta
do zeta = -zeta_max, -1
  R_zeta_2 = (zeta * T - T_prime)**2 + (r_prime**2 + r**2) &
      - two * r_prime * r * cos(zeta * gamma - gamma_prime)
  R_zeta = sqrt(R_zeta_2)
  V_S = V_S + one / R_zeta - dgamit(half, eta * R_zeta_2) * sqrt_eta
end do

! zeta = 0, but only if we are not at a lattice point
if (abs(r_prime - r) > eps .or. abs(gamma_prime) > eps &
    &.or. abs(T_prime) > eps) then
  R_0_2 = T_prime**2 + (r_prime**2 + r**2) &
      &- two * r_prime * r * cos(gamma_prime)
  R_0 = sqrt(R_0_2)
  V_S = V_S + one / R_0 - dgamit(half, eta * R_0_2) * sqrt_eta
end if

! positive zeta
do zeta = 1, zeta_max
  R_zeta_2 = (zeta * T - T_prime)**2 + (r_prime**2 + r**2) &
      &- two * r_prime * r * cos(zeta * gamma - gamma_prime)
  R_zeta = sqrt(R_zeta_2)
  V_S = V_S + one / R_zeta - dgamit(half, eta * R_zeta_2) * sqrt_eta
end do

V_S = V_S - dgamic(0.0_dp, eta * r_prime**2) / T
```

```
  write(*,*), 'V^S = ', V_S

end function V_S


!> Calculates long-ranged V^L component of helical Ewald summation.
!!
!! \param r  Radius of helix of charges, starting positon (r, 0, 0).
!! \param T  Translational operation.
!! \param gamma  Angle of rotation operation.
!! \param r_prime  1st cylindrical coordinate (r) of point at which the
!!     potential is evaluated.
!! \param T_prime  2nd cylindrical coordinate (z) of point at which the
!!     potential is evaluated.
!! \param gamma_prime  3rd cylindrical coordinate (gamma) of point at which the
!!     potential is evaluated.
!! \param eta  Numerical Ewald split parameter.
!! \param l_max  Maximum l summation index in V^L.
!! \param k_max  Maximum k summation index in V^L (usually zero).
!! \param intervals  Number of numerical integration intervals in V^L.
!!
function V_L(r, T, gamma, r_prime, T_prime, gamma_prime, eta, l_max,&
    & k_max, intervals)
  real(dp), intent(in) :: r, T, gamma, r_prime, T_prime, gamma_prime, eta
  integer, intent(in) :: l_max, k_max, intervals
  real(dp) :: V_L

  real(dp) :: x ! (t in paper)
  real(dp) :: bessel_array(l_max+1)
  real(dp) :: bessel_dummy_complex_array(l_max+1)
  real(dp) :: integrand
```

```
integer :: i, l, k
real(dp) :: r_sq, r_prime_sq, four_T_sq_rec
real(dp) :: two_rprime_r
real(dp) :: r_sq_sum
real(dp) :: step
integer :: nz
integer :: ierr
real(dp) :: zr
real(dp), parameter :: zi = 0.0_dp
real(dp), parameter :: fnu = 0.0_dp

r_sq = r**2
r_prime_sq = r_prime**2
four_T_sq_rec = one / (four * T**2)
two_rprime_r = two * r_prime * r
r_sq_sum = r_prime_sq + r_sq

step = eta / intervals
V_L = 0.0_dp

! pre-fill arrays for numberical integration
do i = 1, intervals
  ! start at 1, not zero, because at x=0 (t in paper) we put in the limit
  !  manually

  ! divide by x (t in paper) at the end of each numerical integration step
  ! divide by T at the very end of numerical integration

  ! zbesi returns an array of values in steps of 1 for the order, so we pre
  ! -fill
  ! it as well as the array for variable of integration, x (t in paper), here
  ! and initialize integrand
```

```
x = step * i
integrand = 0.0_dp
call zbesi(two_rprime_r*x, zi, fnu, 1, l_max+1, bessel_array,&
    & bessel_dummy_complex_array, nz, ierr)

if ((nz /= 0) .or. (ierr /= 0)) then
  write (*,*) 'Error or underflow in bessel subroutine'
  stop
end if

! add 1:l_max arrays first, to double later
do l = 1, l_max
  do k = -k_max, k_max
    integrand = integrand&
        & + cos(l*gamma_prime-(l*gamma+two*pi*k)*T_prime/T)&
        & * bessel_array(l+1)&
        & * exp(-r_sq_sum*x-four_T_sq_rec*(two*pi*k+gamma*l)**2/x)
  end do
end do
integrand = integrand * two

! now l=0 for k=finite
do k = -k_max, k_max
  if (k == 0) then
    cycle
  end if
  integrand = integrand + cos(-two*pi*k*T_prime/T) * bessel_array(1)&
      & * exp(-r_sq_sum*x-four_T_sq_rec*(two*pi*k)**2/x)
end do

! now l=0 k=0
```

```
      integrand = integrand +  bessel_array(1) * exp(-r_sq_sum*x)&
          & - exp(-r_prime_sq*x)
      integrand = integrand / x

      ! add up for numerical integration
      if (i == intervals) then
        V_L = V_L + half * integrand
      else
        V_L = V_L + integrand
      end if
    end do

    !this is 1/2 * the limit of the V_L integrand as it approaches 0
    V_L = (V_L - half * r_sq) / T
    V_L = V_L * step

    if (abs(r_prime - r) < eps .and. abs(gamma_prime) < eps&
        & .and. abs(T_prime) < eps) then
      V_L = V_L - two * sqrt(eta / pi)
    end if

    write(*,*), 'V^L = ', V_L

  end function V_L


end module helicalEwald
```

D.2 Supplementary Modules

```
!> Contains interfaces for F77 SLATEC functions.
module interfaces
```

```
implicit none

interface
  !***BEGIN PROLOGUE  ZBESI
  !***PURPOSE  Compute a sequence of the Bessel functions I(a,z) for
  !            complex argument z and real nonnegative orders a=b,b+1,
  !            b+2,... where b>0.  A scaling option is available to
  !            help avoid overflow.
  !***LIBRARY   SLATEC
  !***CATEGORY  C10B4
  !***TYPE      COMPLEX (CBESI-C, ZBESI-C)
  !***KEYWORDS  BESSEL FUNCTIONS OF COMPLEX ARGUMENT, I BESSEL FUNCTIONS,
  !             MODIFIED BESSEL FUNCTIONS
  !***AUTHOR  Amos, D. E., (SNL)
  !***DESCRIPTION
  !
  !                    ***A DOUBLE PRECISION ROUTINE***
  !         On KODE=1, ZBESI computes an N-member sequence of complex
  !         Bessel functions CY(L)=I(FNU+L-1,Z) for real nonnegative
  !         orders FNU+L-1, L=1,...,N and complex Z in the cut plane
  !         -pi<arg(Z)<=pi where Z=ZR+i*ZI.  On KODE=2, CBESI returns
  !         the scaled functions
  !
  !            CY(L) = exp(-abs(X))*I(FNU+L-1,Z), L=1,...,N and X=Re(Z)
  !
  !         which removes the exponential growth in both the left and
  !         right half-planes as Z goes to infinity.
  !
  !         Input
  !           ZR     - DOUBLE PRECISION real part of argument Z
  !           ZI     - DOUBLE PRECISION imag part of argument Z
  !           FNU    - DOUBLE PRECISION initial order, FNU>=0
```

```
!           KODE   - A parameter to indicate the scaling option
!                    KODE=1  returns
!                            CY(L)=I(FNU+L-1,Z), L=1,...,N
!                        =2  returns
!                            CY(L)=exp(-abs(X))*I(FNU+L-1,Z), L=1,...,N
!                            where X=Re(Z)
!           N      - Number of terms in the sequence, N>=1
!
!         Output
!           CYR    - DOUBLE PRECISION real part of result vector
!           CYI    - DOUBLE PRECISION imag part of result vector
!           NZ     - Number of underflows set to zero
!                    NZ=0    Normal return
!                    NZ>0    CY(L)=0, L=N-NZ+1,...,N
!           IERR   - Error flag
!                    IERR=0  Normal return     - COMPUTATION COMPLETED
!                    IERR=1  Input error       - NO COMPUTATION
!                    IERR=2  Overflow          - NO COMPUTATION
!                            (Re(Z) too large on KODE=1)
!                    IERR=3  Precision warning - COMPUTATION COMPLETED
!                            (Result has half precision or less
!                            because abs(Z) or FNU+N-1 is large)
!                    IERR=4  Precision error   - NO COMPUTATION
!                            (Result has no precision because
!                            abs(Z) or FNU+N-1 is too large)
!                    IERR=5  Algorithmic error - NO COMPUTATION
!                            (Termination condition not met)
subroutine zbesi(zr, zi, fnu, kode, n, cyr, cyi, nz, ierr)
  double precision, intent(in) :: zr
  double precision, intent(in) :: zi
  double precision, intent(in) :: fnu
  integer, intent(in) :: kode
```

```
  integer, intent(in) :: n
  double precision, dimension (n), intent(out) :: cyr
  double precision, dimension (n), intent(out) :: cyi
  integer, intent(out) :: nz
  integer, intent(out) :: ierr
end subroutine zbesi


!***BEGIN PROLOGUE  DGAMIT
!***PURPOSE  Calculate Tricomi's form of the incomplete Gamma function.
!***LIBRARY   SLATEC (FNLIB)
!***CATEGORY  C7E
!***TYPE      DOUBLE PRECISION (GAMIT-S, DGAMIT-D)
!***KEYWORDS  COMPLEMENTARY INCOMPLETE GAMMA FUNCTION, FNLIB,
!             SPECIAL FUNCTIONS, TRICOMI
!***AUTHOR  Fullerton, W., (LANL)
!***DESCRIPTION
!
!   Evaluate Tricomi's incomplete Gamma function defined by
!
!   DGAMIT = X**(-A)/GAMMA(A) * integral from 0 to X of EXP(-T) *
!              T**(A-1.)
!
!   for A .GT. 0.0 and by analytic continuation for A .LE. 0.0.
!   GAMMA(X) is the complete gamma function of X.
!
!   DGAMIT is evaluated for arbitrary real values of A and for non-
!   negative values of X (even though DGAMIT is defined for X .LT.
!   0.0), except that for X = 0 and A .LE. 0.0, DGAMIT is infinite,
!   which is a fatal error.
!
!   The function and both arguments are DOUBLE PRECISION.
```

```
  function dgamit (a, x)
    double precision dgamit
    double precision, intent(in) :: x
    double precision, intent(in) :: a
  end function dgamit

  !***BEGIN PROLOGUE  DGAMIC
  !***PURPOSE  Calculate the complementary incomplete Gamma function.
  !***LIBRARY   SLATEC (FNLIB)
  !***CATEGORY  C7E
  !***TYPE      DOUBLE PRECISION (GAMIC-S, DGAMIC-D)
  !***KEYWORDS  COMPLEMENTARY INCOMPLETE GAMMA FUNCTION, FNLIB,
  !             SPECIAL FUNCTIONS
  !***AUTHOR  Fullerton, W., (LANL)
  !***DESCRIPTION
  !
  !   Evaluate the complementary incomplete Gamma function
  !
  !   DGAMIC = integral from X to infinity of EXP(-T) * T**(A-1.)  .
  !
  !   DGAMIC is evaluated for arbitrary real values of A and for non-
  !   negative values of X (even though DGAMIC is defined for X .LT.
  !   0.0), except that for X = 0 and A .LE. 0.0, DGAMIC is undefined.
  !
  !   DGAMIC, A, and X are DOUBLE PRECISION.
  function dgamic (a, x)
    double precision dgamic
    double precision, intent(in) :: x
    double precision, intent(in) :: a
  end function dgamic
end interface
```

```
end module interfaces

!> Contains constants for helical Ewald summation.
module parameters
  use accuracy
  implicit none

  real(dp), parameter :: one = 1.0_dp        !< Numerical 1.
  real(dp), parameter :: two = 2.0_dp        !< Numerical 2.
  real(dp), parameter :: four = 4.0_dp       !< Numerical 4.
  real(dp), parameter :: half = 0.5_dp       !< Numerical 1/2.
  real(dp), parameter :: pi = 3.14159265358979323846_dp      !< Numerical pi.
  real(dp), parameter :: eps = epsilon(1.0_dp)      !< small number close to 0.

end module parameters

!> Accuracy parameters.
module accuracy
  implicit none

  !> Kind parameter for real numbers (double precision).
  integer, parameter :: dp = selected_real_kind(14, 300)

end module accuracy
```

Appendix E

Description of Empirical Potentials

Section E.1 is adapted from my M.S. thesis, I. Nikiforov, A Study of Bending Deformations in Carbon Nanotubes Using the Objective Molecular Dynamics Method, Master's thesis, University of Minnesota, Minneapolis, MN, 2010.

E.1 Tersoff Potential

The overall form of the potential is [141]

$$E = \frac{1}{2}\sum_{i \neq j} E_{ij}, \quad E_{ij} = f_c(X_{ij})[f_R(X_{ij}) + b_{ij} f_A(X_{ij})]. \tag{E.1}$$

The potential function E is modeled as a sum of pair terms E_{ij}, where ij runs over every pair of atoms in the system that are within the cutoff radius S of the potential. E_{ij} has a superficially simple form, with three two-body terms – $f_R(X_{ij})$ (the repulsive potential), $f_A(X_{ij})$ (the attractive potential) and $f_C(X_{ij})$ (the cutoff function). The many-body term b_{ij} scales the attractive term and accounts for all the complexity of semiconductor bonding. The repulsive and attractive terms have the following form:

$$f_R(X_{ij}) = A\exp(-\lambda X_{ij}), \quad f_A(X_{ij}) = -B\exp(-\mu X_{ij}). \tag{E.2}$$

Here, A, B, λ and μ are fitted parameters. The exponential forms are a "universal" way to describe general bonding behavior[31, 152], due to several reasons aside from their

computational efficiency. Introduced by Abell[153], it is logical to describe bonding in such a way because atomic wavefunctions decay exponentially with radius. Also, *ab initio* studies of simple molecules showed a nearly exponential dependence of f_R and f_A on X_{ij} [153]. The cutoff function has the form

$$f_C(X_{ij}) = \begin{cases} 1: & X_{ij} < R \\ \frac{1}{2} + \frac{1}{2}\cos[\pi(X_{ij} - R)/(S - R)]: & R < X_{ij} < S \\ 0: & X_{ij} > S. \end{cases} \tag{E.3}$$

This form is chosen simply because it is a smooth way to go from full interaction ($f_C = 1$) to no interaction ($f_C = 0$). Here, S is the total cutoff radius beyond which atom pairs do not interact. R is the beginning of the cutoff transition. These are chosen so that in equilibrium configurations, only nearest-neighbors interact, and they interact fully ($f_C = 1$). Finally, the all-important many-body term takes the form

$$b_{ij} = (1 + \beta^n \zeta_{ij}^n)^{-1/2n}, \tag{E.4}$$

where

$$\zeta_{ij} = \sum_{k \neq i,j} f_C(r_{ik}) g(\theta_{ijk}), \quad g(\theta_{ijk}) = 1 + \frac{c^2}{d^2} - \frac{c^2}{d^2 + (h - \cos\theta_{ijk})^2}. \tag{E.5}$$

This form is justified by qualitative arguments about the nature of bonding in semiconductors. First, it is important to understand the specific challenge posed by modeling semiconductors. Semiconductors are unique in that their equilibrium states posess intermediate coordination. Metals assume close-packed structures, while the elements at the upper right of the periodic table tend to – disregarding weak long-range forces – form diatomic molecules. This is, of course, excluding the inert gases which form no molecular bonds at all. Semiconductors, on the other hand, are in between these two extremes in the sense that while they form coherent bulk structures (as opposed to isolated diatomic molecules) these structures are not close-packed. Moreover, many semiconductors have several stable configurations with different coordinations. Silicon, with small changes in pressure, can assume a large number of different coordinations[31]. More pertinent to this work is the example of carbon, which, at room temperature and pressure, has the two commonly known bulk forms of graphite and diamond, not to mention the plethora of stable nanostructures. The difficulty in modeling this behavior is clear. Particularly,

any potential that includes only two-body terms that are "physically reasonable" will have a minimum energy configuration that is close-packed[31].

Abell[153] argued that the bond order b (the strength of each bond) weakens as the coordination number z (the number of bonds to a particular atom) increases. The more bonds connect to a single atom, the weaker (lower binding energy) each bond is. Thus, there is a trade-off between having few strong bonds or having many weak bonds. The exact dependence of bond order on coordination determines the equilibrium coordination. If the dependence is strong, each extra bond will reduce bond order greatly and will reduce total binding energy. The extreme case of this is elements which form diatomic molecules – only one bond. If the dependence is weak, each extra bond will not affect the bond order significantly and will therefore increase total binding energy. The extreme case here is metals, which have the maximum number of bonds possible – close packing. Semiconductors are special because their b-z relationship strikes a "delicate balance" which means the equilibrium configuration has an intermediate number of bonds[31].

The measure of bond order in the Tersoff potential is the term b_{ij}. It can be shown that, for a potential of the form in eq. E.1 with components from eq. E.2, the energy is independent of coordination number if $b \propto z^{1/2}$. In eq. E.4, β and n are fitted parameters, while ζ_{ij} is a measure of "effective coordination". For simplicity, one can assume $\zeta_{ij} = z - 1$ for now. The form of eq. E.4 was chosen because, with the correct choice of β and n, at low z, b_{ij} has a less negative slope than $z^{1/2}$, while at higher z, b_{ij} has a less negative slope than $z^{1/2}$[31]. In other words, compared to the $b \propto z^{1/2}$ case which creates a constant total binding energy as a function of z, taking away a bond at low coordination does not increase bond strength as much, while adding a bond at high coordination decreases the bond strength more. This creates a minimum total binding energy at intermediate coordination.

The term ζ_{ij} is meant to represent the number of bonds connecting to atom i besides the ij bond, thus the earlier assumption that it is equal to $z - 1$. Because this is the only term modifying the strength of a bond based on the local environment, however, it clearly cannot be that simple. Without some kind of angular dependence, the shear modulus of diamond is zero and all structures with the same coordination and nearest-neighbor distance have the same energy (elements that can assume a diamond

structure would also be able to assume a planar square structure at the same energy, for example)[31]. So, the present form of ζ_{ij} (eq. E.5) counts all the atoms $k \neq i, j$ around i that are inside the cutoff (scaled appropriately if they are between R and S), scaled by the angular function $g(\theta_{ijk})$. In g, the parameter h represents the cosine of the optimal bond angle of the particular species it is fitted to. When $cos(\theta_{ijk}) = h$, g does not modify the bond strength. Any deviations from the optimal bond angle lower the bond strength. Parameters c and d are fitted. In practice, h is also fitted and does not generally correspond to the bond angle of any single configuration. There is even no reason it has to lie between -1 and 1[31].

E.2 Lennard-Jones Potential

The form of the Lennard-Jones potential is exceptionally simple, as it models non-reactive interactions between atoms. It is a pairwise potential, meaning that each term in the summation only depends on the coordinates of two atoms. The energy is

$$E = \frac{1}{2} \sum_{i \neq j} 4\epsilon \left[\left(\frac{\sigma}{X_{ij}} \right)^{12} - \left(\frac{\sigma}{X_{ij}} \right)^{6} \right]. \tag{E.6}$$

σ is the parameter that controls equilibrium distance, while ϵ controls the strength of the interaction. An alternate form often used for convenience in atomistic simulation codes is

$$E = \frac{1}{2} \sum_{i \neq j} \left[\frac{a}{X_{ij}^{12}} - \frac{b}{X_{ij}^{6}} \right]. \tag{E.7}$$

Appendix F

Commonly Used Terms and Abbreviations

Due to the large variety of topics adressed herein, no attempt is made to summarize all of the symbols and abbreviations found in the work. Additionally, it is unavoidable that between different chapters, some symbols are reused with different meanings. However, regarding the central topic of this dissertation – objective molecular dynamics – an effort has been made to use a unified convention. Thus, the symbols used for describing helical-angular objective boundary conditions are listed below.

- $\mathbf{X}$ – atomic position.
- $\mathbf{T}$ – translation vector. When used in context of helical objective operation, lies along z-axis.
- $\mathbf{R}$ – rotation matrix, always around z-axis in this work.
- ζ – simulation cell image index.
- h – helical objective operation consisting of rotation of angle γ around z-axis and translation T along z-axis.
- g – angular objective operation consisting of rotation of angle ψ around z-axis.
- MD – Molecular dynamics.

- PBC – Periodic boundary conditions.
- OMD – Objective molecular dynamics.
- DFTB – Density-functional-based tight-binding.